NOVEL SURFACE MODIFICATION TECHNIQUES TO ENHANCE BIOCOMPATIBILITY OF METALLIC MATERIALS FOR MEDICAL IMPLANTS

by

Mahdis Shayan

B. S. in Biomedical Engineering, Amirkabir University of Technology (Tehran Polytechnic), 2004

M. S. in Biomedical Engineering, Amirkabir University of Technology (Tehran Polytechnic), 2008

Submitted to the Graduate Faculty of

The Swanson School of Engineering in partial fulfillment

of the requirements for the degree of

Doctor of Philosophy

University of Pittsburgh

2016

UNIVERSITY OF PITTSBURGH

SWANSON SCHOOL OF ENGINEERING

This dissertation was presented

by

Mahdis Shayan

It was defended on

June 03, 2016

and approved by

Bopaya Bidanda, PhD, Ernest E. Roth Professor and Chairman, Department of Industrial Engineering

Prashant Kumta, PhD, Edward R. Weidlein Chair Professor, Department of Bioengineering

Ravi Shankar, PhD, Associate Professor, Department of Industrial Engineering

Dissertation Director: Youngjae Chun, PhD, Assistant Professor, Department of Industrial Engineering

NOVEL SURFACE MODIFICATION TECHNIQUES TO ENHANCE BIOCOMPATIBILITY OF METALLIC MATERIALS FOR MEDICAL IMPLANTS

Mahdis Shayan, PhD

University of Pittsburgh, 2016

Four different novel surface modification techniques have been investigated to enhance the cell growth behavior in metallic implantable materials. The potential of each technique has been studied for improving current treatments in a target disease. The first surface modification technique is the creation of nanoscale grain surfaces on stainless steel 316L material via linear plane-strain machining. The *in vitro* cell adhesion study demonstrates the enhanced osteoblast adhesion and growth on the native oxide layer formed on the material with the smallest grain size (*i.e.*, created by 0° rake angle). This result represents a high potential of nanoscale grain surface in stainless steel for improving the bone bonding for orthopedic biomaterials. The second surface modification technique is a rapid endothelialization of thin film nitinol through electrostatic cell seeding process. This technique utilizes dielectrophoresis supplying for temporarily created positive surface charges on thin film nitinol. *In vitro* cell adhesion assays have demonstrated the

enhanced seeding of endothelial cells on thin film nitinol under the optimal electrical conditions (*i.e.,* 5V applied voltage for 30 minutes) which shows the potential use of the technique for thin film nitinol based low-profile endovascular graft. In the third technique, a thin layer of silk is deposited on the thin film nitinol substrate using electrospinning technique to facilitate the surface endothelialization and to enhance the hemocompatibility. The proof-of-concept *in vitro* test results have demonstrated that the integrated thin film nitinol and electrospun silk represents a high-potential candidate material for small-diameter vascular grafts owning to favorable properties of thin film nitinol and silk. The last technique introduces the micropatterned thin film nitinol as a novel low-profile cover for stents in treating carotid artery stenosis disease. A sputter deposition technique along with a lift-off process was used to create various microscale features in thin film nitinol. The micropatterned thin film nitinol effectively captured the embolic particles dislodged from the carotid artery stenosis *in vitro* model. Besides, the micropatterned thin film nitinol has significantly enhanced endothelial cell adhesion and growth. Therefore, four surface modification techniques showed advancement in cellular behavior with the various metallic biomaterials used in treating critical diseases.

TABLE OF CONTENTS

LIST OF TABLES

LIST OF FIGURES

PREFACE

This dissertation is dedicated to my parents, *Fatemeh* and *Mohammadreza* and my brother, *Alireza* for their unconditional love and support.

1.0 BACKGROUND

Millions of people around the world are receiving implanted medical devices and biomaterials to replace the function of the diseased tissue. Despite the important role of implants in saving people's life and improving the quality of their life, many of these implanted devices and biomaterials fail in a short term and have many complications. Major failure in biomaterials is from their inadequate biocompatibility. Biocompatibility is defined as follows:

"*The ability of a biomaterial to perform its desired function with respect to medical therapy, without eliciting any desirable local or systemic effects in the recipient or beneficiary of that therapy, but generating the most appropriate beneficial cellular or tissue response in that specific situation, and optimizing the clinically relevant performance of that therapy*"(Williams, David F., *Biomaterials*, 2008).

Based on this definition, biocompatibility testing consists of a wide variety of tests for evaluating the suitability of the biomaterials that contact with the human body both in a short and long term. Therefore, the evaluation of the biomaterials' surface, mechanical and biological properties are primary categories of biocompatibility testing. Implantable medical devices and biomaterials must undergo numerous biocompatibility tests depending on the host location and type of the device to ensure their safety and effectiveness prior to be used in human body. *In vitro* cell culture tests are highly favorable and have been widely used to assess the important

biological response of the implanted biomaterials and to study the cellular interaction with them before entering clinical trials. Typical cell culture studies include cell adhesion, migration, proliferation and differentiation studies and any of these should be specifically chosen depending on the type of implantable devices and biomaterials.

This dissertation includes four major sections. Disease backgrounds are first introduced and the limitations of current devices and biomaterials (*e.g.,* biocompatibility) are discussed. Novel surface treatment strategies are suggested for each device or material to overcome the biological complications occurred in the current treatments. This dissertation brings up today's significant challenges found in the biomaterials field related to cell-biomaterials interface. In addition, this study presents novel solutions and useful information to meet these challenges and shed some light on these complications.

Two types of materials that are used for presenting these strategies include 316L stainless steel and thin film nitinol. 316L stainless steel has been widely used as a biomaterial in bone fixation devices (plates, screws and pins) and artificial joints. Thin film nitinol shows a high potential for new small vascular devices (*e.g.,* heart valves and covering stent grafts) due to its unique and beneficial properties (*e.g.,* superelasticity and low-profile feature).

After indicating the challenging issues of current treatments in each disease and presenting the techniques to obviate these obstacles, in the next step, appropriate *in vitro* tests have been used to examine the effectiveness of the new techniques in resolving the implied challenges. In each case, the suggested technique is compared to the current treatment to demonstrate the level of effectiveness of the suggested technique.

In the first part, four groups of 316L stainless steel surfaces with average grain sizes in the range of 42nm (*i.e.,* corresponding to 0°-tool-rake-angle-obtained chip) up to 22μm (*i.e.,* corresponding to bulk sample) have been used.

The first generation of bone implants was filling the empty space of the lost tissue in the bone showing inert biological response. As an example, metallic biomaterials such as stainless steel substrates with passivated oxide layers on their surface demonstrate corrosion resistance and inert surfaces in the biological environment. However, one of the main failure reasons of orthopedic implanted materials is the weak connection between the surface of the implanted material and bone. Therefore, if the bonding between the bone and the surface of the implant improves, the performance and lifetime of it increases. Hence, in biomaterials field, one of the important research areas is to improve the biocompatibility by modifying the biomaterials surface. Biomaterials with modified surfaces can improve the host response in the direction to accept the biomaterial instead of ignoring it as inert biomaterials.

Since interactions between cells and biomaterial surfaces are mediated by molecules and cell membrane at nanoscale dimensions, creating nano-structure surfaces for biomaterials can influence the cellular behavior in the interface of biomaterials and biological cells, for example, increasing the attachment of bone cells. Accordingly, the potential of ultrafine grain size 316L stainless steel substrates is examined for improving the bone bonding for orthopedic implants.

The mechanism behind the enhancement of cell attachment on the ultrafine grain size substrates has not been explicitly known and there is the lack of understanding regarding to the effects of refining the grain size on cellular response. Since the cells directly contact with oxide layer formed on the surface, we characterize the properties of the oxide formed on the nanograin substrates. In addition to naturally formed oxide layer, by using thermal and chemical treatment

methods, oxide layer is grown on the nanograin substrates. Growing oxide layer on the surfaces with different average grain sizes facilitates the study of the effect of grain size refinement on the surface oxide properties; furthermore, growing oxide layer along with refining the grain size creates surfaces with various surface properties (*e.g.*, surface roughness).

In order to discover the surface that possibly enhances the bone attachment, MC3T3 (precursor osteoblast cells) cells are cultured on the surfaces and the adhesion and proliferation of them are assessed on the all the oxide surfaces. The results demonstrate that the adhesion of osteoblasts attachment are higher on the surface of naturally oxide layer compared to thermally and chemically formed oxide layers and the adhesion of cells enhances on the surface with the smallest average grain size (*i.e.*, obtained by 0° tool rake angle). Therefore, the naturally formed oxide layer on the surface of 316L stainless steel with nanoscale average grain size (*i.e.*, ~ 42nm) demonstrate a high potential in enhancing the bone attachment and reducing the loosening occurrence in orthopedic biomaterials. To understand the reason behind enhancing osteoblast adhesion on the naturally formed oxide layer on 0° chips compared to all other surfaces, important surface properties which determine the cellular response (*i.e.*, surface topography, chemistry and surface wettability) are analyzed. In future studies, the microstructure of oxide layers formed on the nanograin substrates will be fully analyzed using transmission electron microscopy (TEM) imaging to achieve a better understanding about the effect of grain size refinement on the cell adhesion.

In addition to orthopedic biomaterials, the other high-demanding group of biomaterials is endovascular devices. Small-diameter vascular diseases are mostly life-threatening and if not treated in an effective manner, they can cause serious damages or even result in death. In this dissertation, two new thin film nitinol-based endovascular biomaterials have been suggested

which show improvement in terms of their surface interaction with surrounding biological environment. These biomaterials include: 1) electrostatic endothelial cell seeded thin film nitinol, 2) integrated thin film nitinol/electrospun silk. Three major features which affect the performance of endovascular devices include: 1) bulkiness, 2) surface endothelialization, 3) blood-compatibility. Bulk devices occupy more volume of the blood vessel duct and raise the probability of thrombosis occurrence because of the high probability of blood flow disturbance; this factor highly matters in small-diameter blood vessel. Thin film nitinol demonstrates a significantly low profile (*i.e.,* 6μm) compared to commercially available grafts such as e-PTFE or Dacron materials (*i.e.,* 100-200μm); furthermore, due to the superelasticity of thin film nitinol, it can provide sufficient radial force to prevent migration under blood flow of small-diameter blood vessels without need to use vascular stent backbones which result in a significant reduction in the bulkiness of the device.

Adhesion and growth of endothelial cells play a key role in the success of small-diameter vascular devices since endothelial cells can potentially enhance the thrombosis resistance similar to the native blood vessel tissue. A new electrostatic endothelial cell seeding inside the small-size catheter (*e.g.,* 6Fr) has been introduced in order to performing the endothelial cell seeding right before the endovascular surgery. The results demonstrate applying 5V voltage with induced electrostatic charge of 0.68×10^{-6}μC and induced electric field of $5.11 V/mm^{-1}$ for 30min duration on the superhydrophilic thin film nitinol substrate significantly enhances the attachment of endothelial cells.

Besides, electrospun silk demonstrates a remarkable enhancement on endothelial cell adhesion and reduction in blood coagulation compared to control materials during *in vitro* tests. Therefore, the proof-of-concept *in vitro* testing results suggest that electrostatic endolthelial

seeded thin film nitinol and integrated thin film nitinol/ electrospsun silk and be promising candidate materials for small-diameter vascular devices and can create a significant improvement in the treatment of small-diameter vascular diseases.

In addition to unique characteristics of thin film nitinol such as superelasticity and being low-profile, various micropatterns can be created on its surface. The micropatterned thin film nitinol is suggested to be used as a covering membrane for stents since the stents can open the narrowed blood vessel but they cannot prevent the dislodgment and embolization of microparticles from the plaques while a covering membrane can trap the embolic particles. Diamond-shape micropatterned covered stent can prevent the emboli dislodgement up to 85% through 30min *in vitro* tests. Besides, endothelial cell adhesion, growth and elongation significantly enhance on the micropatterned thin film nitinol surface. According to the *in vitro* results indicating the high emboli protection and enhanced endothelial cell coverage, micro-patterned thin film nitinol represents a high-potential low-profile candidate membrane for covering the vascular stent in treating carotid artery stenosis.

Consequently, this dissertation presents primary *in vitro* results of enhancing the cell attachment on the surfaces of the metallic substrates (*i.e.*, 316L stainless steel and thin film nitinol) which have been modified by using the surface modification techniques including refining the average grain size of 316L stainless steel substrate, inducing the electrostatic charge on thin film nitinol surface, coating the thin film nitinol surface with nanofibrous silk and creating micropatterned surfaces on thin film nitinol. This dissertation introduces new biomaterials in order to improve the current treatments of several critical diseases and also sheds some light on several subjects in the category of biomaterials-cells interface.

2.0 INTRODUCTION

Millions of people in the US use implanted medical devices, annually. Medical implants are placed permanently or temporarily into the damaged body parts to replace or support the missing body function. In addition to replacing the damaged body parts, implants can be used for various applications such as delivering medication, monitoring body functions or supporting the repair of damaged tissues. Therefore, a wide variety of implanted medical devices have been developed for many different parts of the body such as hip implants, vascular grafts, bone grafts, dental implants, orthopedics screws and plates, pacemakers, cardiovascular stents, heart valve replacements and drug delivery systems (Figure 1). Metals are the most widely used materials for load-bearing implants such as fracture fixation plates, artificial joints, maxillofacial implants and dental implants. In addition, they are used for vascular stents and cardiovascular devices. The most commonly metals in biomedical applications are stainless steels, cobalt-base alloys, commercially pure titanium, titanium alloys and nickel-titanium (*i.e.*, nitinol) alloy.

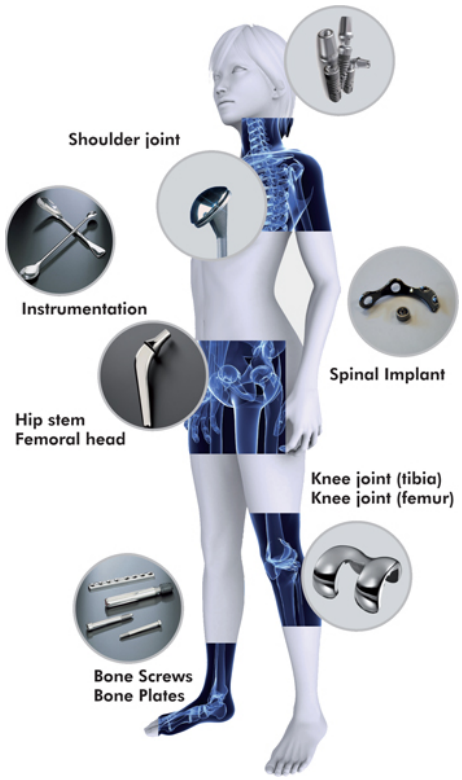

Figure 1: Examples of implants and medical devices[1]

In recent decades, the use of medical implants is remarkably growing, for example, in 2004, the number of implanted drug-eluting stents alone exceeded two million[2]. With the increasing population of patients, aging population and lengthening the life expectancy, developing a new generation of advanced biomaterials with longer lifetime and improved properties is required. In the implantable device, the interaction of biomaterials surface with biological cells and surrounding tissues is one of the most critical factors affecting the success and lifetime of them. Lack of sufficient integration between the implanted biomaterial and the host tissue results in the failure of implants[3, 4]. Therefore, a more detailed understanding of

interactions occurring in implants interface with their surrounding biological environment is known as one of the today fundamental requirements in biomaterial research field whereas the vast majority of the biological principles controlling the interaction of cells with implants remain largely ambiguous. Here, the interaction of cells with the implanted material surface and effective surface parameters regarding to this process as well as surface modification techniques to improve the bio-functionality of the metallic implantable materials are reviewed.

2.1 CELL-SURFACE INTERACTION IN BIOMEDICAL IMPLANTS

The cell–material interaction is a complex interplay of a variety of biological processes which is strongly influenced by implant surface properties such as surface hydrophilicity, surface roughness, texture and morphology as well as surface chemistry and surface electrostatic charge[5, 6]. Immediately after placing the implant inside the body, a water layer forms on the surface and the chemistry and electrostatic charge of the surface determine the level of water molecules dissociation and their bonding strength as well as the incorporation of the surrounding ions on covering the surface. Subsequently, the proteins existing in the biological fluid attach on the implant surface via physical or chemical bonds. The chemical and physical characteristics of the surface determine which proteins adhere on the surface and also determine their orientation and spatial arrangement. Protein adhesion on the surface is a thermodynamic process based on electrostatic, hydrophobic or covalent interactions which is also affected by the size and concentration of proteins[7, 8]. The interactions of surface-bound proteins with cells are mediated via integrins. Integrin receptors are heterodimers composed of α and β subunits that

occur in distinct combinations which then bind to specific ligands. Different cells express various integrins which the type and level of this expression is affected by physicochemical properties of the surface. For instance, microrough surfaces increase the expression of the β1 integrin subunit, which is essential in osteoblastic differentiation[9]. Apart from integrins in the surface, focal adhesions consist of specific proteins such as talin, α-actinin and vinculin filaments that interact with the cytoskeleton on the cytoplasmic side of the cells. Through focal adhesions, cells react to extrinsic chemical and mechanical signals from the cell–cell contact or cell-extracellular matrix (ECM) components. Changes in microscale and nanoscale of their surrounding environment (*e.g.*, implant surface) cause signal transduction and lead to change in cell behavior since cells communicate with their surrounding environment via electrical, chemical and mechanical signals.

Here, the role of important surface factors especially in metallic biomaterials in determining the biological cell behaviors have been reviewed:

2.1.1 Surface chemistry

Biocompatibility of metal biomaterials is due to forming a chemically stable oxide layer on their surface which separates the highly reactive bulk material from the biological environment. For instance, stainless steel materials are resistant to a wide range of corrosive agents due to their high chromium content (>12 wt%), which allows the formation of a strongly adherent, self-healing and corrosion resistant coating oxide of Cr_2O_3. The oxide layer interacts with proteins and cells upon implantation since surface chemistry effectively influences proteins adsorption and their conformation, and initial cell attachment. For example, Rapuano and McDonald

showed that negatively charged functional groups of surface oxide in Ti_6Al_4V alloy can modulate fibronectin integrin receptor activity by altering the adsorbed proteins conformation[10].

2.1.2 Surface roughness, morphology and texture

Three-dimensional morphology of an implant is thought to be a major factor in determining cell response and implant performance. Surface microroughness affects osteoblast differentiation as well as the synthesis of proteins such as collagen type I, vitronectin and fibronectin[11].

In addition, cells interact and respond to the surface nanotopography[12]. Conformational changes in focal adhesions and cytoskeletal conformation transfer information about the ECM topography to the nucleus as mechanical signals. In response to mechanical signals, cytoskeleton filaments reorient and subsequently a distortion occurs in the cell nucleus which may induce changes in gene transcription[13].

Surface topography is known as an effective factor on determining signaling pathways through modulation of integrin clustering[14].

2.1.3 Surface energy and wettability

Surface free energy is a more important surface characteristic than surface roughness for cellular adhesion strength and proliferation. Various models have been suggested to explain the relationship between the wettability and surface roughness[15]. According to Wenzel's model, wettability decreases by roughening smooth hydrophobic surfaces and increases by roughening

smooth hydrophilic surfaces. Osteoblast cell growth and proliferation generally increases with increasing surface roughness and hydrophilcity[16]. It is shown that cell attachment and spreading are significantly greater on hydrophilic surfaces than on hydrophobic surfaces.

2.1.4 Surface electrostatic charge

Surface electrostatic charge affects the electrical parameters of cells and produces signals to regulate cell behavior. For example, increasing surface charge density is shown that improves the cell adhesion and proliferation in several polymeric substrates[17]. Furthermore, cell differentiation and adhesion change on surfaces with positive ions and the negative ions as well[18]. For instance, osteoblast and fibroblast adhesion improve in hydroxyethylmethacrylate (HEMA) hydrogels with positive charges compared to negative or neutral charges[19]. Surface charge may regulate protein adsorption and through it control the cell adhesion. It has been postulated that negative charge may facilitate adsorption of proteins and promote cell adhesion and responses.

2.1.5 An example study on evaluating cell-surface interaction in biomedical implants (improved osteoblast response to UV-irradiated PMMA/TiO_2 nanocomposites with controllable wettability)

Chun *et al.,* evaluated osteoblast response of PMMA/TiO_2 nanocomposite thin films that exhibited the controllable wettability with UV treatment. In this study, three samples of PMMA/TiO_2 were fabricated with three different compositional volume ratios (*i.e.*, 25/75, 50/50,

and 75/25) followed by UV treatment for 0hr, 4hrs, and 8hrs. Surface profiler and atomic force microscopy demonstrated the increased surface roughness after UV irradiation due to the partial elimination of PMMA on the surface (confirmed by Fourier transform infrared spectroscopy (FTIR). All samples showed the increased hydrophilicity after UV irradiation. The films fabricated with the greater amount of TiO_2 and treated with the longer UV irradiation time increased the hydrophilicity more. The partial elimination of PMMA on the surface after UV irradiation created a durable hydrophilic surface by (1) exposing higher amount of TiO_2 on the surface, (2) increasing the hydroxyl groups on the TiO_2 surface, and (3) producing a mesoporous structure that helps to hold the water molecules on the surface longer. While all UV-treated hydrophilic samples demonstrated the improvement of osteoblast cell adhesion, the PMMA/TiO_2 25/75 sample after 8hrs UV irradiation *(i.e.,* the superhydrophilic surface) represented the best cellular response as compared to other samples (Figure 2)[9].

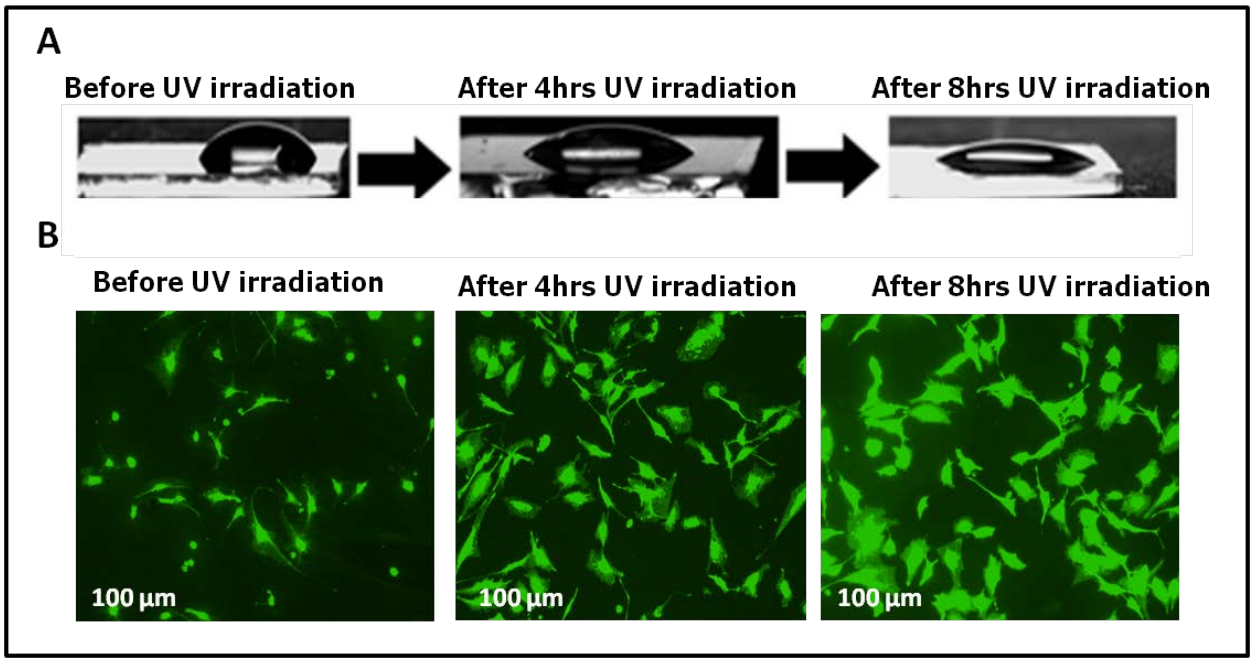

Figure 2: A) Water contact angle and B) Fluorescent images of attached MC3T3 cells before and after 4hrs and 8hrs UV irradiation on 25/75 PMMA/TiO_2 nanocomposites[9]

2.2 SURFACE MODIFICATION TECHNIQUES IN METALLIC BIOMEDICAL IMPLANTS

To functionalize the surface of metallic implants, different physical and chemical surface treatments have been studied. One surface treatment strategy is coating the surface of the implant with a bioactive ceramic (*e.g.*, hydroxyapatite (HA) and bioactive glass). Surface treatment methods for this coating include electrophoretic deposition, plasma spraying, radio frequency sputtering, laser ablation and hot isostatic pressure[20-25]. None of these methods produce covalent links with the substrate and in long-term implantation they can delaminate, besides,

there are difficulties in controlling the final composition and structure of the coating. While chemical surface modification (*e.g.,* thermochemical techniques, sol-gel coating or attachment of self-assembled monolayers) obtains or induces the deposition of a bioactive ceramics on metallic surfaces *in vivo* and creates a direct chemical link between the substrate and the coating [26-28]. Surface bio-activation can be achieved by functionalizing surfaces with different biomolecules and biopolymers such as immobilization of ECM proteins, peptide sequences and DNA by applying a variety of methods where both chemical bonding and physical adsorption take place. With the advancements of technology, role of nanostructure surface of materials on improving cell behavior have been evaluating.

2.2.1 Nano-functionalizing of metallic biomaterials

Nanostructure surfaces have the ability to mimic the biological environment hereby improving the cell behavior and functionalizing the surface to bind to specific biological targets (*e.g.,* ligands, proteins, antigens or cell types). For example, Webster *et al.,* demonstrated increased osteoblast cell adhesion on different nanophase metallic microparticles (*i.e.,* Ti, Ti6Al4V and CoCrMo) compared to conventional particles owning to creating surfaces with nanoscale roughness and increasing grain boundaries[29]. Multiple methods have been suggested to produce nanostructure metallic surfaces such as chemical etching, powder metallurgy techniques, anodic oxidation and nanocoatings[30, 31]. However, these methods require multi-step processes, they are chemically complicated, or result in uncontrolled surface property changes. Severe plastic deformation (SPD) techniques eliminate the concerns of conventional methods. SPD can result in extreme grain refinement obtaining nanograin material through large

deformations applied at high strain rates and relatively low temperatures. SPD methods can produce material with relatively higher strength and novel mechanical properties. These methods have high potential to produce a new generation of implant materials through concurrent enhancement of mechanical characteristics and biocompatibility[32].

2.2.2 Thin film nitinol (TFN) biomaterial and surface modification techniques for it

Nitinol, the acronym for Nickel Titanium Naval Ordinance, is an equiatomic nickel–titanium composition alloy that is known mostly for two unique properties of shape memory and superelasticity[33]. The shape memory response of nitinol is defined as the recovery of the material's mechanical deformation when it is heated to above the transformation temperature (*i.e.,* austenite phase) from a low temperature state (*i.e.,* martensite phase). Another unique feature of nitinol is the superelasticity that provides high resistance against plastic deformation. Bulk nitinol has a long-track record of successful uses in many endovascular applications; however, nitinol-based devices are relatively bulky when used with synthetic graft materials such as expanded polytetrafluoroethylene (e-PTFE) or Dacron© polyester. In general, these devices could be used for treating vascular diseases in large diameter blood vessels such as abdominal aortic aneurysms; however, it is difficult to deliver the synthetic polymer-covered nitinol devices in many trauma situations. For example, it is challenging to deliver the device into the calcified blood vessels (*i.e.,* narrowed vasculature), the highly tortuous small vascular systems, and pediatric patient's blood vessels. Therefore, there is a significant need for the development of new biomaterials that are low-profile and hemocompatible, as well as deliverable to the desired disease locations with appropriate material properties such as elasticity, toughness, and fatigue

resistance. One novel material worth considering for developing a low-profile transcatheter device is the relatively new material, “thin film nitinol”[34]. Vacuum sputter deposition process for thin film nitinol is considered the preferred fabrication method, because of the precise controllability of the deposition process and the consistency of the quality of the films[35]. The thickness of thin film nitinol as materials in medical devices would be 3-12μm depending on the type of applications. Thin film nitinol can be used in small caliber vascular system, including cerebral, carotid, coronary, renal arteries and veins, and so on. In addition, thin film nitinol exhibits superelastic property in human’s body temperature, which improves the device apposition with vascular wall compared to any synthetic fabric that typically has wrinkles or permanent deformation. Vascular wall apposition is especially critical for the devices used in small and low blood flow vascular systems; therefore, thin film nitinol is a great candidate as a covering membrane for minimizing or preventing blood flow disruption and local thrombosis accumulation between the graft and vascular wall.

While nitinol is a well-known biocompatible material, the thrombotic complications frequently occur when it is used for vascular implants in small arteries. A variety of factors including surface roughness, wettability, and surface charge, involve in thrombosis. It is known that native blood vessels are negatively charged and hydrophilic which has been postulated to decrease the attachment of blood products. Therefore, Chun *et al.*, suggested different techniques to treat thin film nitinol surface in order to obtain a more hydrophilic and negatively charged surface (*i.e.*, UV irradiation, heat treatment and H_2O_2 chemical modification)[36].

UV irradiation induces a photochemical reaction on the surface including a reduction reaction of titanium ions in the surface oxide layer and the generation of vacancies in its oxygen. The oxygen vacancies cause surrounding water molecules to dissociate and the hydroxyl groups

absorb on the surface boosting the hydrophilicity and negative charge. However, UV irradiation didn't significantly improve the wettability of nitinol thin film due to the extremely low thickness of the native oxide layer (less than 10nm) and the lack of the stability of absorbed hydroxyl groups on the surface. Another method to grow oxide layer was heat treatment, heating the sample above 600ºC resulted in the formation of a thick and uniform oxide layer (*i.e.*, ~100nm) on the surface creating a superhydrophilic surface but the thick surface TiO_2 causes embrittlement in the film deteriorating the proper mechanical behavior. While both UV irradiation and heat treatment did not show the best results for creating a high-quality superhydrophilic surface, chemical modification using 30% H_2O_2 for 15hrs at room temperature, demonstrated that a high-quality hydrophilic surface was produced maintaining the desirable mechanical properties of the thin film[36].

The ultra-smooth surface of thin film nitinol and the uniform oxide layer created by chemical treatment on its surface, obtains a superhydrophilic surface while the improvement of surface wettability in bulk nitinol after the similar surface treatment, is much less. Thus, this method is suggested the preferred surface treatment method to improve the biocompatibility of thin film nitinol[36].

In this dissertation, four different new techniques for improving the cell adhesion and growth in metallic biomaterials have been evaluated. For each technique, a disease has been targeted that the surface modification technique shows potential for improving the treatment for the disease. The first technique "obtaining nanograin surfaces by linear plane-strain machining" has been evaluated for stainless steel substrates for improving the osseointegration in orthopedic biomaterials applications. The other three methods are used for thin film nitinol substrates for vascular graft application.

3.0 TECHNIQUE 1: OBTAINING NANOGRAIN 316L STAINLESS STEEL BY LINEAR PLANE-STRAIN MACHINING

3.1 INTRODUCTION

Population aging and high incidence of osteoporosis, obesity and arthrosis all lead to increasing demands for orthopedic devices such that it is estimated that the number of total hip and knee joint replacements will be duplicated by the year 2015 and 2026, respectively[37]. Besides, it is estimated that from 2012 to 2019, the orthopedic devices market will grow from $29.2 billion to $41.2 billion[38]. In addition to increasing the demands, due to increasing the average life expectancy, development of novel orthopedic devices with higher durability and functionality are urgently required. Mechanical strength and stability is a fundamental requirement for orthopedic biomaterials since they are mostly used in load-bearing positions such as internal fixation devices and joint implants. Therefore, metals (*i.e.*, titanium alloys, cobalt alloys and stainless steel) are the main composition used in orthopedic biomaterials providing sufficient strength under high static and cyclic loads[39, 40]. Although metals present a wide range of favorable mechanical properties for load-bearing orthopedic applications compared to ceramic and polymer compositions; however, they are all inert and do not interact with the biological environment to bond with the bone and enhance biological interface[41]. Therefore, improving

the biological function of metallic surface can open the window to design and develop novel durable orthopedic biomaterials. Biological cells do not directly attach to the biomaterial surface, they attach to proteins and biomolecules initially adsorbed on the surface and composition and configuration of these adsorbed proteins and biomolecules conduct signals to cells determining their behavior (*e.g.,* adhesion, differentiation, proliferation and apoptosis). Since surface cell receptors and native ECM proteins are structured in nanoscale (*e.g.,* 25-50 nm hydroxyapatite crystals and 300nm collagen fibrils in bone), it is indicated that cell signaling in biomaterial-biological environment interface occurs in the nanoscale. Thus, engineering the surface in nanoscale has been inferred as an attractive technique to manipulate surface chemistry, roughness, topography and surface energy in nanometer scale in order to control the absorbance of proteins and biomolecules in this scale and improving the cell behavior[6, 42, 43]. For example, Webster *et al.,* demonstrated increased osteoblast adhesion on different nanophase metallic microparticles (*i.e.,* Ti, Ti6Al4V and CoCrMo) compared to conventional particles owning to creating surfaces with nanoscale roughness and increasing grain boundaries[29].

Severe plastic deformation (SPD), is an alternative approach which can produce metals with ultra-fine grain sizes through applying large deformation at high strain rates [44, 45]. Under SPD processes, lattice defects within polycrystalline metals are annihilated and recombined creating new grain boundaries and refining the average grain size [46, 47]. SPD techniques do not have complications of other nanofabrication methods and also increase the mechanical strength of the bulk material. Multiple studies have investigated the effect of refining the grain size on the cellular behavior. In these studies, different SPD techniques such as equal channel angular pressing (ECAP), high pressure torsion (HPT) and severe cold rolling have been applied (Figure 3) on a wide range of substrates (*e.g.,* commercial pure titanium, Ti6Al4V alloy, pure iron,

nitinol alloy, copper, zirconium, stainless steel sample) using various types of cells (*e.g.*, fibroblast cell, osteoblast cells and endothelial cells).

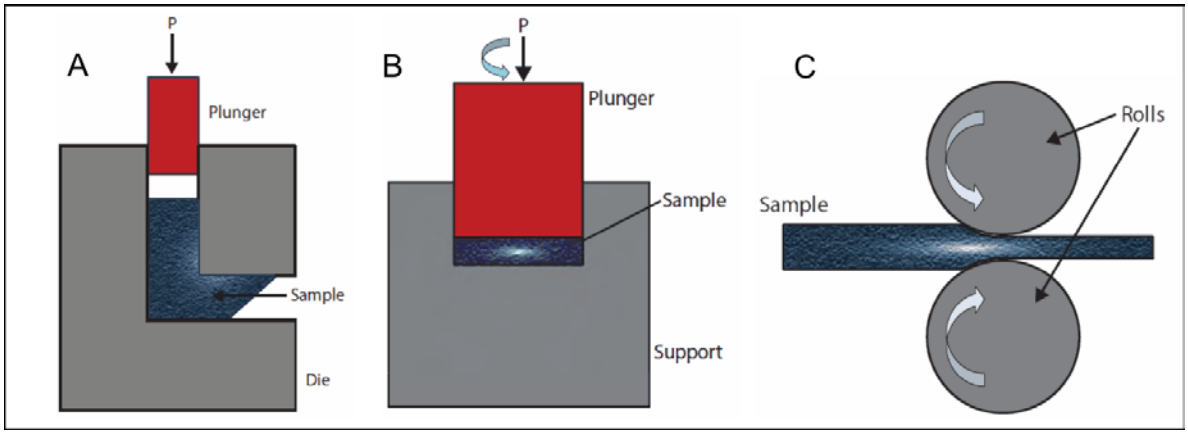

Figure 3: Schematic illustration of examples of SPD techniques: (A) Equal channel angular pressing (ECAP), (B) High pressure torsion (HPT) and (C) Severe cold rolling[48]

Table 1 reviews a number of studies about the effect of grain size refinement on the cellular behavior. Most of these studies report positive cellular responses (*e.g.*, improvement in adhesion, proliferation, viability of cells) in ultra-fine grain size samples but there are also reports such as Saldana *et al.* study that observed no difference between the viability, proliferation and spreading of cells on the coarse grain and ultra-fine grain size Zirconium samples[49]. The reason behind the effect of grain size refinement on the cellular response is hypothesized the increase in the surface energy or creation of numerous nanoscale points to facilitate the attachment of cells[32].

Table 1: Examples of studies about the effect of grain size refinement on the cellular behavior [49-56]

	Substrate	SPD Method	Average Grain size	Cell type	Results
1	Copper	ECAP	260nm	L929	Higher cell viability on NG samples (MTT assay)
2	Zirconium	Severe rolling	240nm	SaoS-2	-Enhancement of Wettability in NG samples -No difference was observed between viability, proliferation and spreading of cells between samples
3	Pure Ti	ECAP	350- 450nm	3T3	-Enhancement of wettability in nanograined (NG) samples - Higher Cell adhesion and proliferation on NG samples (MTT assay) -Higher adsorption of fibronectin protein on NG samples
4	Pure Ti	ECAP	200nm	MC3T3- E1	-Higher Cell proliferation on NG samples (MTT assay)
5	Pure Ti	ECAP	170- 200nm	hMSC	-Different surface topography between control and NG samples (by AFM) -Higher cell adhesion and spreading on NG samples
6	Pure Ti	Surface mechanical attrition treatment (SMAT)		SaOs-2	-Higher Cell viability on NG samples
7	Pure Ti	HPT	10-50nm	MC3T3	-XPS and XRD demonstrated a different oxide layer on the NG surface compared to control. - Wettability changes on NG samples -Higher cell adhesion on NG samples

Table 1 (continued)

8	Nitinol	HPT	200-300nm	L929 Mg63	-No difference for L929 but improvement in cell viability for MG63 cells on NG samples
9	AZ31 Mg alloy	Grove pressing (GP)	5µm	L6	-No difference in Viability (MTT assay) NG surfaces showing: - Higher surface wettability -Lower corrosion rate -Higher Bioactivity -Roughness increasing

Linear plane-strain machining is a SPD method whereby a sharp tool quickly removes the surface metal in a predetermined depth and angle. In this method, grain size can be controlled by three parameters of rake angle, tool velocity, and cutting depth [57, 58]. Controlling the average grain size in nanoscale provides nanofunctional surfaces that can have potential applications to develop advanced biomedical implants and improve their performance.

In this study, austenitic 316L stainless steel samples in three different nanoscale average grain sizes are obtained by linear plane-strain machining SPD technique. The aim is to investigate whether grain refinement by linear plane-strain machining technique in stainless steel 316L can affect MC3T3 responses. To understand the effect of grain size refinement on surface characteristics and surface oxide structure, a comprehensive surface characterization is performed.

3.2 METHODS

3.2.1 Preparation of test samples

Commercially available, annealed and cold-finished 316L stainless steel plate (McMASTER-CARR, Cleveland, OH, USA) was used in this study. The plate was processed by linear plane-strain machining at room temperature using cutting depth of 150µm and tool velocity of 25mm/s for three different rake angles of +40°, +20° and 0°. The dimensions of resulting chips were typically 8mm×3mm×0.25mm. Control samples were prepared by cutting the bulk plate in 8mm×3mm×1mm pieces using diamond saw. The nanograin chips and control sample were mechanically grinded by SiC paper and polished using polycrystalline diamond suspensions in 9 and 3µm sizes (DP suspension P, Struers, Denmark) followed by a mirror finish by colloidal silica suspension (OP-U suspension, Struers, Denmark) using the polishing machine (Struers, Tegramin-25, OH, USA) and then were cleaned in acetone and ethanol for 20min in an ultrasound system. Oxide layer was chemically grown on all three nanograin chips and the control sample using the chemical method reported by Evance *et al.* [59]. Briefly, samples were soaked in the solution containing 5M sulfuric acid (VWR, BDH Aristar® Plus, Canada) and 2.5M chromic acid (Sigma-Aldrich, MO, USA) at 70°C temperature for 30min and 1hr duration. Thermal treatment was also examined to grow the oxide layer on nanograin chips and the control sample. Thus, samples were thermally oxidized in air at 1000°C temperature for 15min and rapidly cooled to room temperature [60].

3.2.2 Hardness measurement

The Vickers hardness of control nanograin samples was measured using microhardness tester (Shimadzu, HMV-2 Series, Japan).

3.2.3 Surface characterization

3.2.3.1 Surface wettability

To measure the wettability of surfaces (*i.e.,* three types of nanograin chips and control sample before and after chemical and thermal treatments), sessile drop method was used by a drop shape analysis system (Kruss, DSA10, PA, USA). Deionized (D.I) water was dispersed on top of surfaces from a syringe, the drop image was recorded by a video camera and the contact angle of the drop was calculated.

3.2.3.2 Surface topography

Surface profile and roughness of untreated nanograin chips and coarse-grain sample which have the mirror-finish surface was studied by optical surface profiler (Veeco NT3300 Optical Profiler, GA, US). Average roughness (R_a), root mean squared roughness (R_q) and maximum height of the profile (R_t) was measured and R_a was used to compare the surface roughness between different groups. Furthermore, surface topography and microstructure of all samples (*i.e.,* three types of nanograin chips and control sample before and after chemical and thermal treatments) was characterized by scanning electron microscopy (SEM) (Jeol-JSM 6610 LV, Japan). A nanometer layer of palladium (pd) was sputtered on the surface before SEM imaging.

3.2.3.3 Surface chemistry

Surface chemistry of all samples before and after thermal and chemical treatment was analyzed using X-ray Photoelectron Spectroscopy (XPS, ESCALAB 250 XI Thermoscientific, USA). In addition to survey spectra, high-resolution XPS spectra at Fe2p and Cr2p were acquired for control and nanograin samples.

3.2.4 Cell viability and proliferation assay

All samples were sterilized by soaking in 70% ethanol for 30min and subsequently washed with sterile PBS (Gibco®, NY, USA). MC3T3 cells at passage number 6 were seeded on the specimens at a density of 3×10^5 cells/ml. Cells were grown in MEM Alpha (1×) medium (Gibco®, NY, USA) containing 10% FBS and 1% Antibiotic-Antimycotic solution. 2ml of media was added in each well of the tissue culture plate and the plates were kept in a humidified incubator under 5% CO_2 at 37°C.

After 48hrs cell culture, the samples were washed with PBS, loaded with 1ml 10µM Calcein AM (life technologies™, NY, USA) solution and were incubated in (37°C and 5% CO_2) for 30min before imaging. Fluorescent images were taken to observe the live and attached cells using fluorescent microscopy (Olympus BX43, Japan).

Cell proliferation was assessed by a colorimetric assay using 3-(4, 5-dimethylthiazol-2-yl)-2, 5-diphenyl tetrazolium bromide (MTT, CT02 MTT Cell Growth Assay Kit, EMD Millipore, Darmstadt, Germany). Cells were cultured for 1hr, 2hrs, 4hrs, 24hrs and 5 days at an initial seeding density of 3×10^5 cells/ml. After the determined incubation time, 0.01ml pre-warmed MTT solution was added to each culture well containing 0.1ml fresh cell medium and

the cell culture plate containing MTT solution continued incubation for 4hrs under the same conditions. MTT solution has a pale yellow color which live cells cleave it to yield a dark blue formazan product. This transformation is catalyzed just by active cell mitochondria. Thus, the measurement of produced formazan can be an index of number of live cells. After 4hrs incubation of cells with MTT, 0.1ml isopropanol with 0.04 N HCl was added to each well. The HCl converts the phenol red in tissue culture medium to a yellow color that does not interfere with MTT formazan measurement. The isopropanol dissolves the formazan to give a homogeneous blue solution suitable for absorbance measurement. The absorbance was measured at a wavelength of 570nm using microplate reader (BioTek® Synergy 2, VT, USA).

The morphology of MC3T3 cells adhered on substrates was probed by SEM after a thin layer of palladium (Pd) deposition by sputtering. For the SEM, cells were fixed with 2.5% glutaraldehyde (Sigma-Aldrich, MO, USA), dehydrated in a series of ethanol/DI water mixtures including 30%, 50%, 75%, 90% and 100% ratios, then, subjected to drying with hexamethyldisilazane (HMDS) (Alfa Aesar, MA, USA)/ethanol in 3:1, 1:1 and 1:3 volume ratios. The samples were dried in the hood overnight at room temperature.

3.2.5 Statistical analysis

For characterization tests (*i.e.,* contact angle measurement, roughness measurement and hardness measurement) and cell culture study, three samples of each condition were examined and results were presented as mean values ± standard deviation (SD). Statistical analysis was conducted in Minitab® 16.1.0 (©2010 Minitab Inc. PA, USA) using the one-way analysis of variance

(ANOVA) test and post hoc Tukey's HSD test. P-value <0.01 was considered statistically significant.

3.3 RESULTS

3.3.1 Hardness measurement

Figure 4 shows the measured Vickers microhardness values of all four samples (*i.e.*, control sample, 40°, 20° and 0° nanograin chips). Vickers microhardness of control sample showed 194±21.7HV and nanograin samples showed 310±59HV, 385±81.97HV and 460±56.92HV for 40°, 20° and 0° chips, respectively. These results demonstrated that decreasing the average grain size significantly increases the Vickers microhardness such that Vickers microhardness of 0° chip with average grain size of 42nm increased more than two times compared to bulk control sample that has 22μm average grain size.

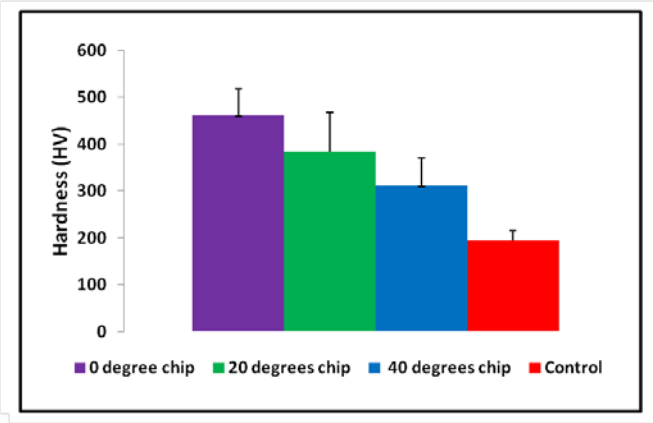

Figure 4: Vickers microhardness for control and 0°, 20° and 40° chips

3.3.2 Surface characterization

3.3.2.1 Surface profile and roughness analysis

Figure 5 shows the surface profile of all four samples (*i.e.*, control sample, 40°, 20° and 0° nanograin chips) that characterized by optical profilometer. Small variation is observed in surface texture of the samples. Surface profile of 0° chip shows a fairly smooth surface with no significant dents and peaks while in control and two other nanograin chips (*i.e.*, 20° and 40° chips), small uneven areas in nanometer scale are observed. Average surface roughness (R_a) of all samples shows less than 20nm, but there is a significant difference between the average surface roughness (R_a) of them (P-value<0.001).

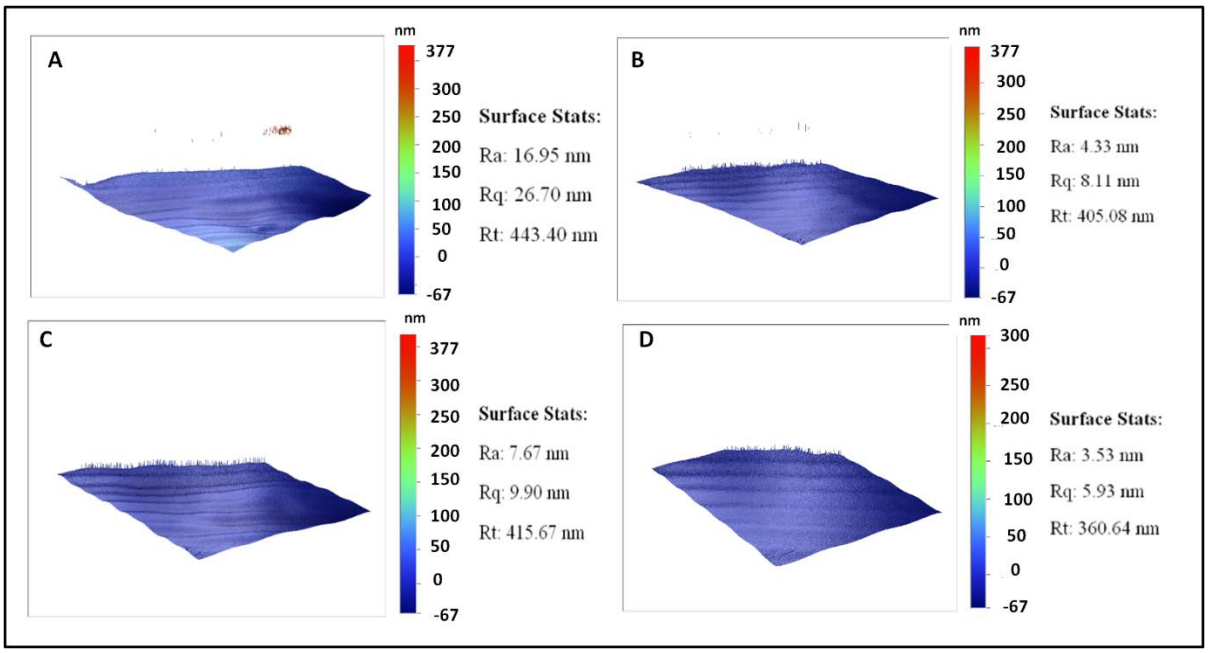

Figure 5: Representative surface profile of A) Control sample, B) 40°chip, C) 20°chip and D) 0°chip

Figure 6 shows the results on surface roughness of four samples. While control sample shows 19.2±1.1nm in average, three nanograin samples show 4±1.4nm for 0° chip, 5.4±0.91nm for 20° chip, and 7.1±0.88nm for 40° chip. As we described the nanograin sample preparation in earlier section (2.2.1), all samples were grinded and polished in a same manner. However, the surface roughness decreased in nanoscale over decreasing the average grain size. The slight difference in the surface roughness might be because of the difference in the hardness of samples causing slight change in the surface profile during surface polishing since the probability of forming dents is higher on surfaces with lower hardness.

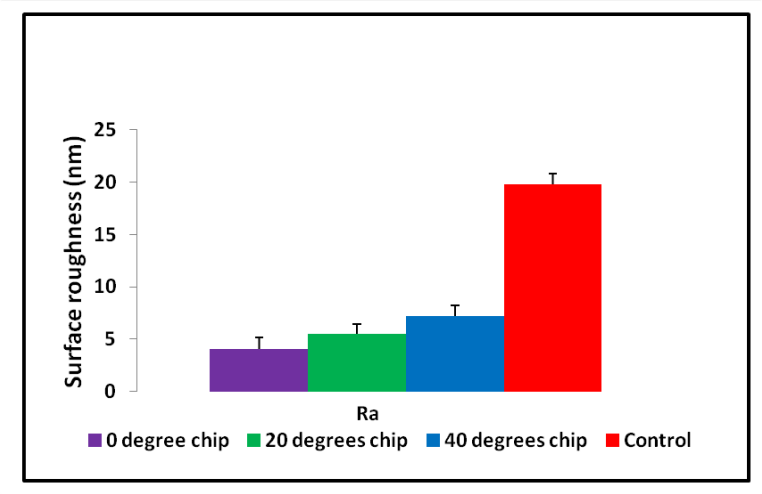

Figure 6: Average surface roughness (Ra) of control sample and nanograin chips

3.3.2.2 Surface topography characterized by SEM

Since the surface profile analysis by optical profilometer is only applicable for shiny surfaces, SEM image was used to inspect detail surface topographies of all samples studied here (*i.e.*, control sample, 40°, 20° and 0° nanograin chips, as well as chemically and thermally treated samples). Figure 7 shows the representative SEM images of untreated, chemically, and thermally treated control samples, 40°, 20° and 0° chips. Untreated surfaces show smooth and mirror-finish topography, no noticeable difference is observed in surface topography of four types of samples (Figure 7-A1, B1, C1 and D1). However, island-like structures, grooves and holes are appeared on the surface after 1hr chemical treatment. The average size of created islands is larger in the control sample (~>10µm) compared to nanograin chips. In nanograin chips, the average size of islands was reduced with the finer nanograin samples (*i.e.*, smaller rake angle). In addition, while both the number and size of holes were increased over decreasing the rake angle from 40° to 0°, the depth of surrounding grooves was increased. Thus, surfaces became rougher in smaller

nanograin samples after chemical treatment (Figure 7-D2). The surface texture after thermal treatment is somewhat different from the surfaces observed in the samples chemically treated. New micro features were appeared on the surface after thermal treatment; however, the size and shape of them were substantially smaller than those observed in the chemically treated samples. The uniformity of surface microfeatures was increased in the finer nanograins. The 0° nanograin chip showed the uniformly distributed microfeatures with an average size of ~2μm that cover the surface, which is different from the control sample (*i.e.*, random size of micro features with non-uniform distribution).

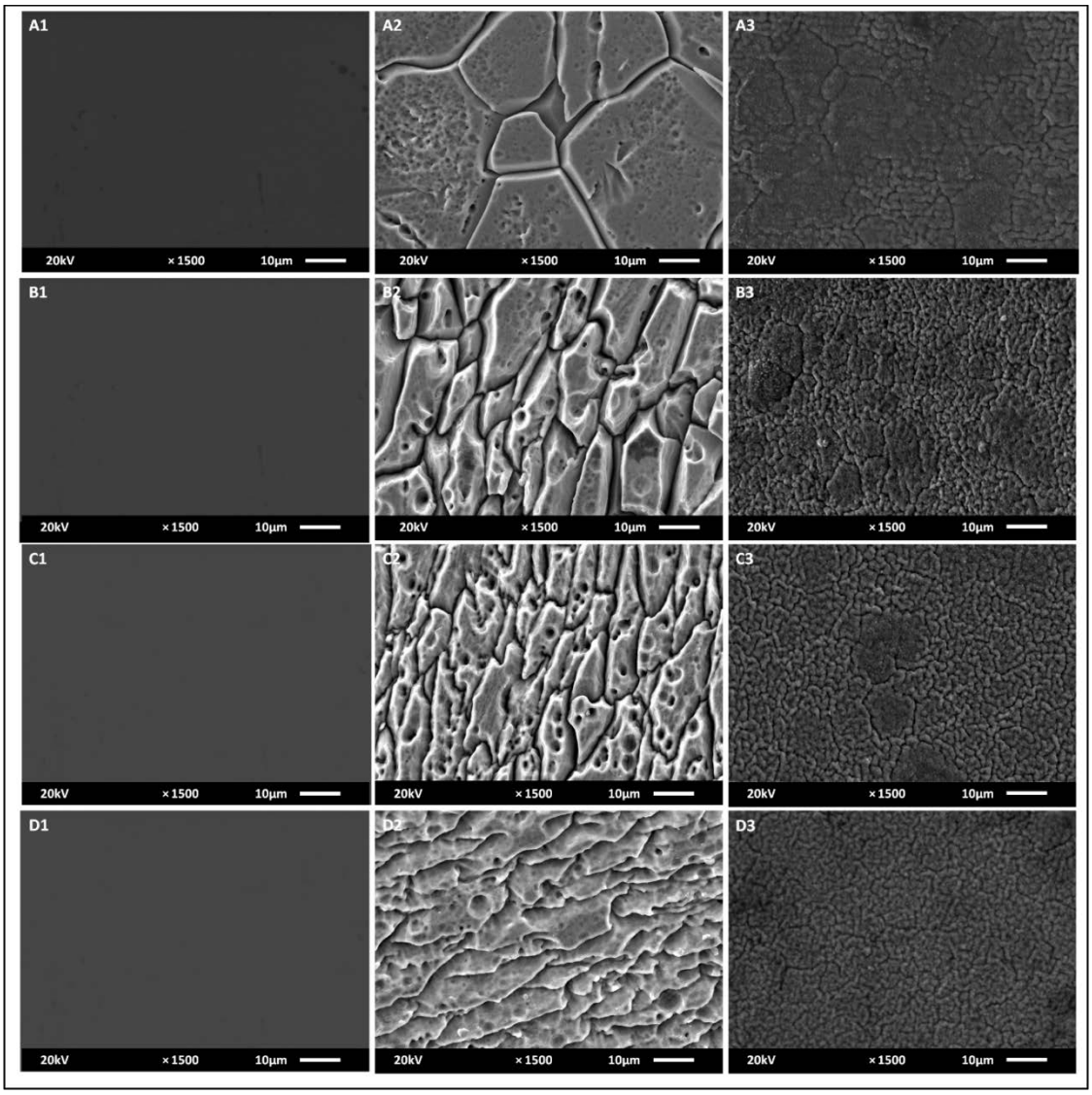

Figure 7: SEM images of A) Control sample: 1. Untreated, 2. Chemical treated, 3. Thermal treated, B) 0° chip: 1. Untreated, 2. Chemical treated, 3. Thermal treated, C) 20° chip: 1. Untreated, 2. Chemical treated, 3. Thermal treated and D) 40° chip: 1. Untreated, 2. Chemical treated, 3. Thermal treated

3.3.3 X-ray photoelectron spectroscopy (XPS) analysis

Chemical compositions of all four samples (*i.e.*, control sample, 40°, 20° and 0° nanograin chips) before any surface treatment were analyzed by X-ray photoelectron Spectroscopy (XPS). Figure 8A shows the survey spectra of these four samples. Identical peaks appeared in all four spectra including dominating peaks corresponding to elements of carbon, oxygen, chromium and iron and the lower peak corresponding to the nickel. High resolution spectra of Fe2p and Cr2p are presented in Figure 8B and Figure 8C, respectively. Fe2p spectra represented a double peak corresponding to free iron and iron oxide compositions. The XPS results for Cr2p region also indicated the presence of free chromium and chromium oxide compositions on the surface.

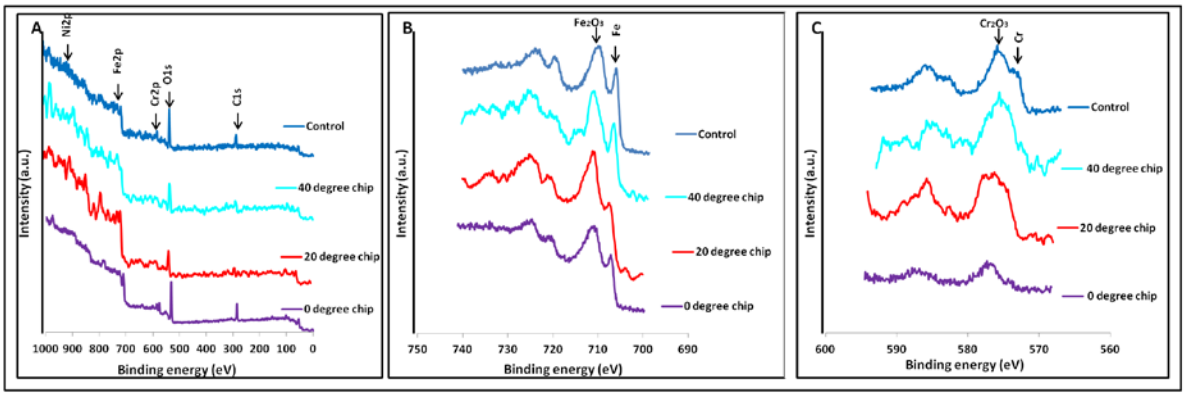

Figure 8: A) Survey XPS spectra and B) High resolution XPS spectra of Fe 2p and C) Cr 2p for control sample and 0°, 20° and 40° chips

To study the chemical compositions of chemically and thermally treated nanograin chips and control sample, similar XPS spectra (*i.e.*, survey, Fe2p and Cr2p) were acquired for them.

Similar to untreated samples, no noticeable differences were observed between the XPS spectra of control and nanorain chips after both thermal and chemical treatments. In both chemically and thermally treated samples, peaks corresponding to free iron and free chromium disappeared (Figure 9 and 10). In chemically treated surfaces, similar peaks to untreated surface were observed; however, the peaks corresponding to chromium oxide and iron oxide significantly intensified.

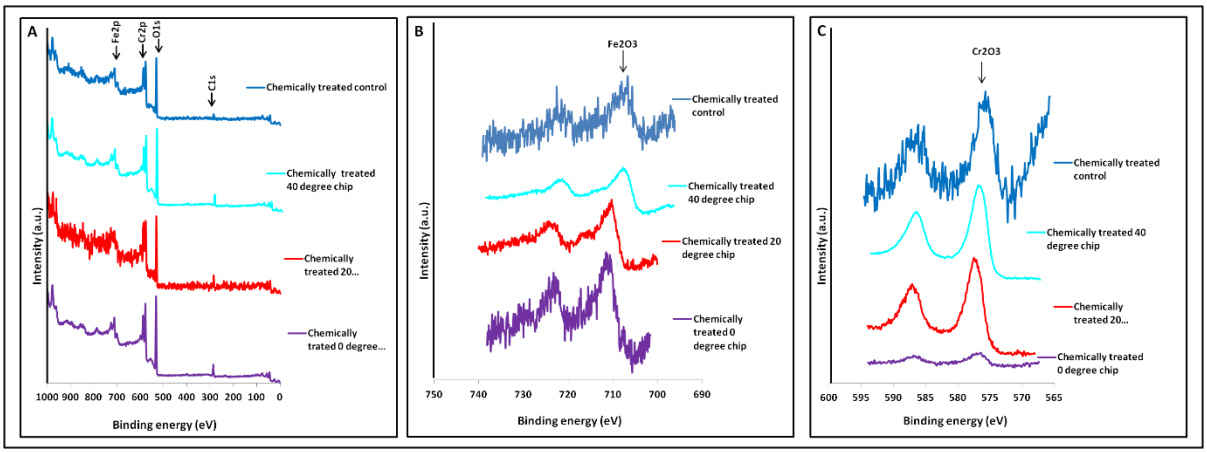

Figure 9: A) Survey XPS spectra, B) High resolution XPS spectra of Fe2p and C) Cr2p for control sample and 0°, 20° and 40° chips after chemical treatment

In thermally treated surfaces, in addition to present peaks observed in untreated surfaces, a new peak corresponding to manganese compositions appeared on the surface and the peak corresponding to chromic oxide strongly intensified.

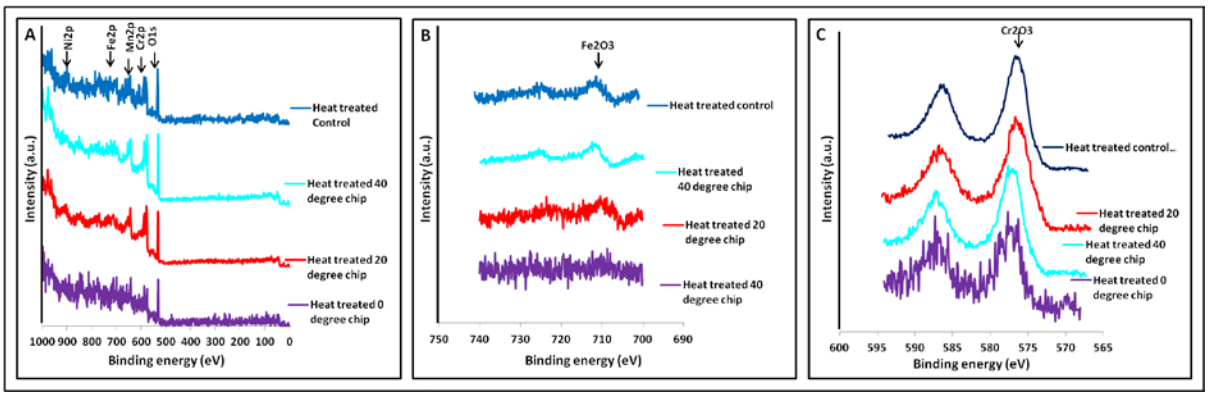

Figure 10: A) Survey XPS spectra, B) High resolution XPS spectra of Fe2p and C) Cr2p for control sample and 0°, 20° and 40° chips after thermal treatment

3.3.4 Contact angle measurement

Figure 11 compares the contact angles measured for control sample and nanograin chips before and after surface treatment. The control sample shows 70.83±2.56° water contact angle and no significant difference is observed between the control, 40°, 20° and 0° chips before surface treatment (P-value=0.299). The contact angles of all samples, however, significantly were decreased (P-value<0.001) after 1hr chemical treatment. There is a trend that samples with smaller grain sizes show greater reduction of contact angles. The 0° chip presents a superhydrophilic surface (9±3.18° contact angle) while the control sample, 40° and 20° chips show contact angle of 28.75±0.35°, 26.75±3.1° and 19.5±1.4°, respectively. Water contact angle was also decreased after thermal treatment compared to the untreated samples (*i.e.*, 50±1.2°, 44.5±0.21°, 39±3.6° and 37±1.8° for control sample, 40°, 20° and 0° chips, respectively). While

the reduction rates were not significant compared to the samples chemically treated, a similar trend was observed in thermally treated samples, which means that samples with smaller average grain size show more hydrophilic surfaces.

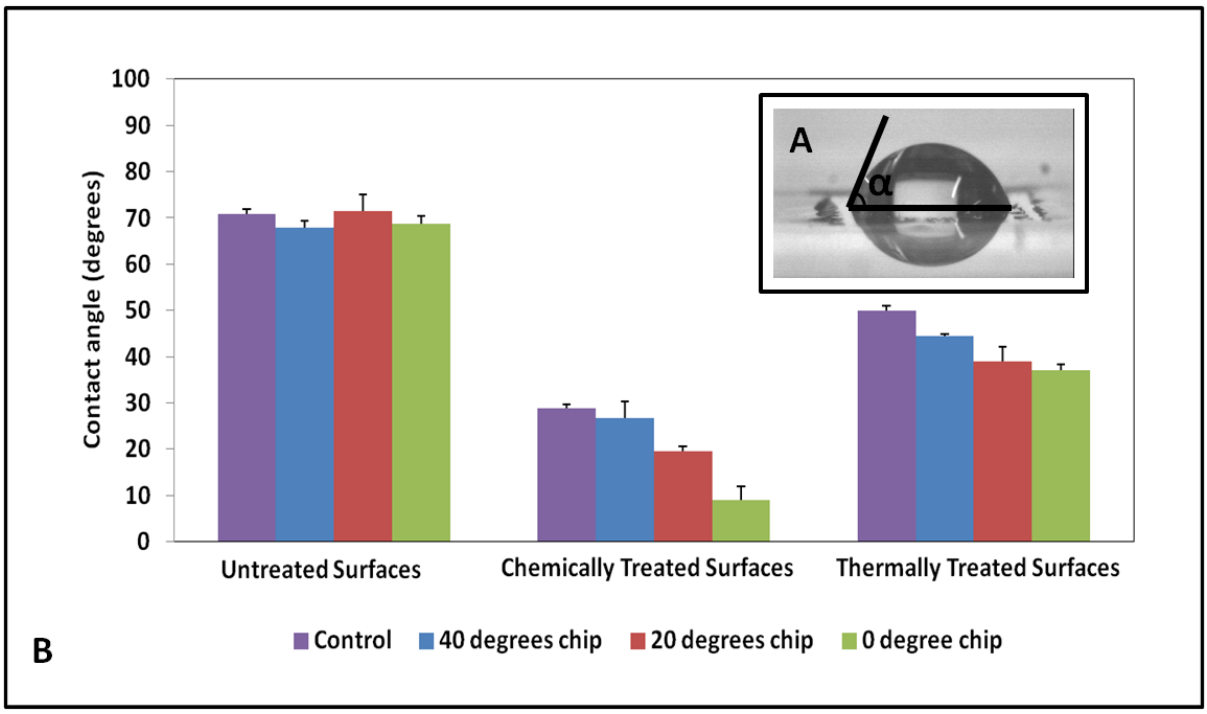

Figure 11: A) Representative image of water contact angle on 0° chip, B) Contact angle measurement of control sample and 0°, 20° and 40° chips before and after chemical and thermal treatment

3.3.5 Cell viability and proliferation assay

Figure 12 shows the mean value of MC3T3 cells viability on untreated, chemically treated and thermally treated samples that were evaluated using the MTT assay over five different periods

(1hr, 2hrs, 4hrs, 1day and 5 days). After 1hr, mean counts of optical density measurement were 0.1086±0.023, 0.0875±0.0082, 0.0774±0.0078 and 0.056±0.001 for untreated 0°, 20°, 40° and control sample, respectively (P-value=0.011) indicating the higher initial cell attachment and viability for smaller grain size samples. This trend was kept for rest of time periods Proliferation rate during these five time periods does not show a noticeable difference between control and nanograin chips. In chemically treated surfaces, no significant difference is observed between samples in all five time periods. However, in thermally treated samples, it shows enhancement in cell viability by decreasing the average grain size. Both chemically and thermally treated samples demonstrate lower proliferation rate compared to untreated samples.

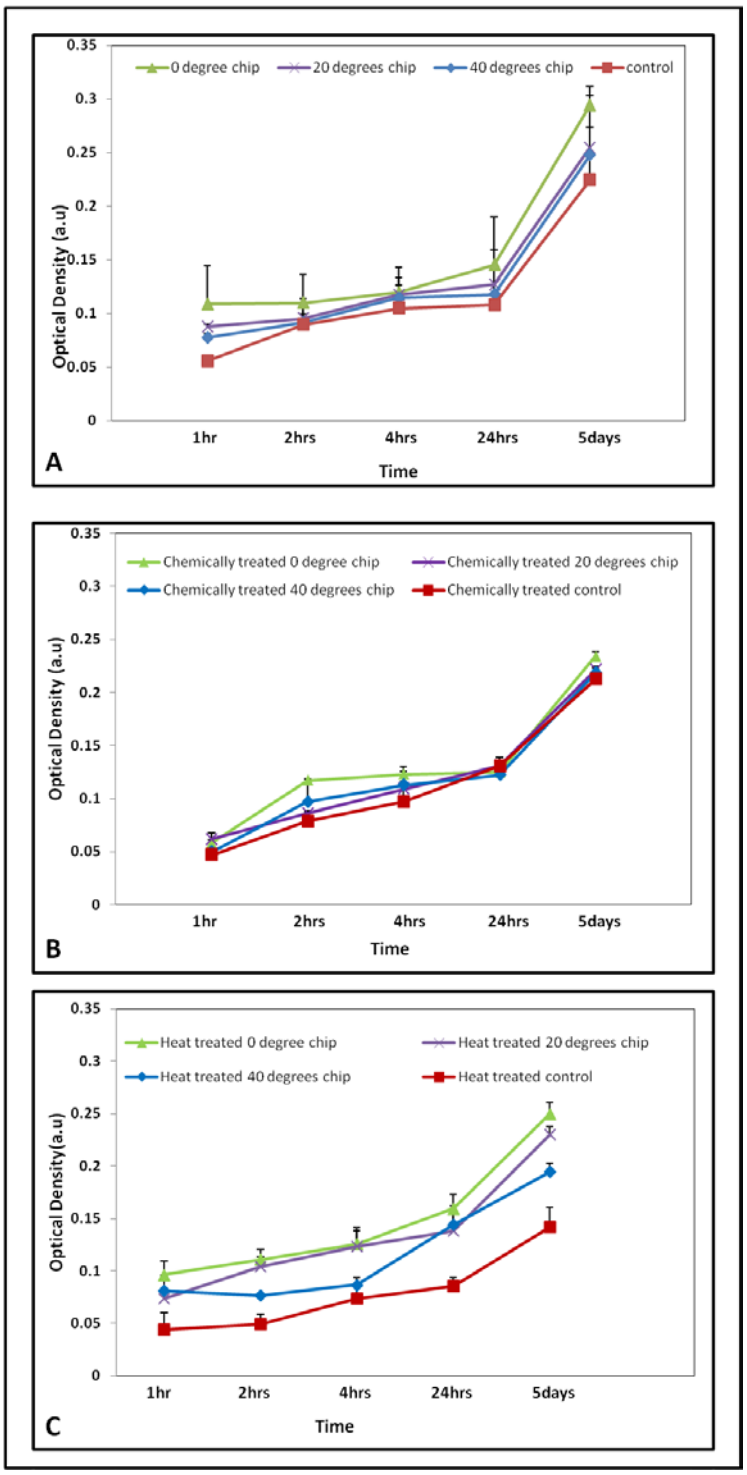

Figure 12. MTT assay for cell viability of control sample and 0°, 20°, 40° chips in A) Untreated, B) Chemically treated and C) Thermally treated conditions after 1hr, 2hrs, 4hrs, 24hrs and 5days

Figure 13 shows Calcein AM stained live cells cultured on the control sample and nanograin chips before and after surface treatments. Highest number of live cells was spread out on the untreated 0° surface. By decreasing the grain size in untreated samples, the cell growth and the fluorescent intensity became higher. In chemically treated surfaces, no significant difference is observed between number of live cells on nanograin chips and coarse-grain surface. However compared to untreated surfaces, the cell growth is lower in analogous chemically treated surfaces. In thermally treated surfaces, number of live cells is higher in 0° chip compared to control sample. The cell growth on thermally treated surfaces is noticeably smaller compared to analogous untreated surfaces.

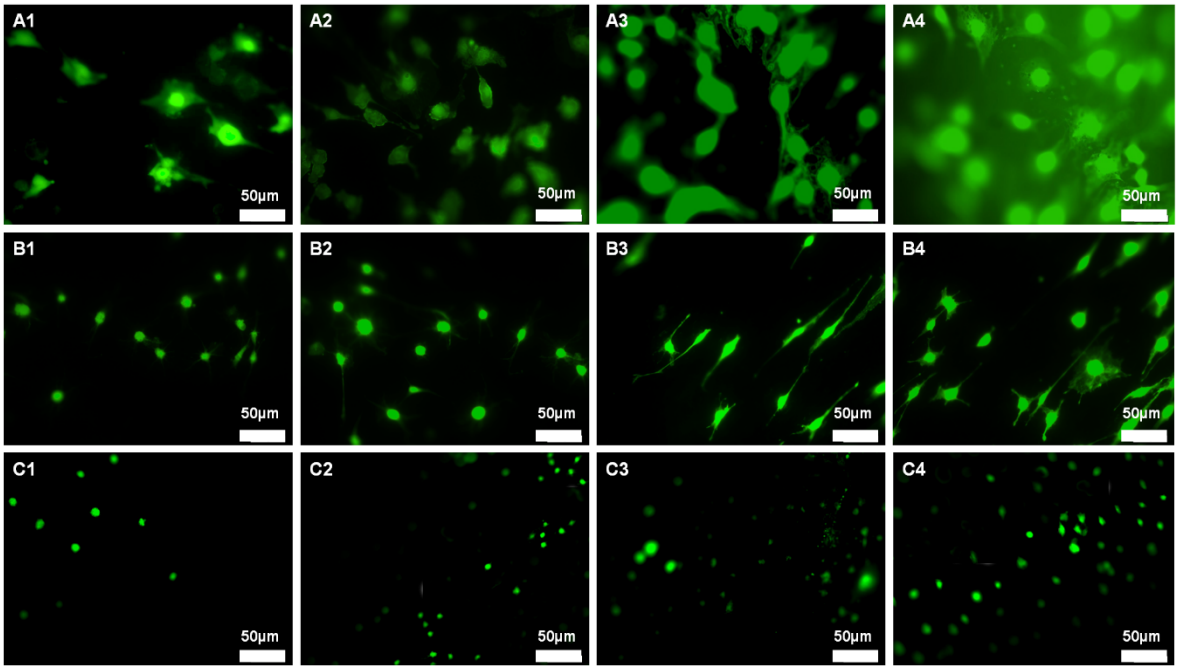

Figure 13: Fluorescent images of Calcein AM stained MC3T3 cells after 48hrs culturing on A1) Control surface, A2) 40° chip, A3) 20° chip, A4) 0° chip, B1) Chemically treated control Surface B2) Chemically treated 40° chip, B3) Chemically treated 20° chip and B4) Chemically treated 0° chip, C1) Thermally treated control surface, C2) Thermally treated 40° chip, C3) Thermally treated 20° chip and C4) Thermally treated 0° chip

Figure 14 shows SEM images of MC3T3 cells cultured on the control sample and nanograin chips before and after surface treatment. Cells on untreated samples fully spread and extend their cytoplasmic projections in multiple directions. Larger size of cells on nanograin chips compared to control sample imply their higher growth on nanograin chips. However, in both groups of surface treated samples, cells do not display fully flat shape similar to untreated surfaces. On chemically treated samples, cells extend their pseudopodia anchoring the rough surface in multiple directions. In chemically treated 0° chip which shows an extremely rough surface, the pseudopodia of cells attached on the surface are pretty elongated. On thermally

treated surfaces, cells have not been spread on the surface, they show a flat shape on control and 40° samples while on 20° and 0° chips, cells demonstrate round shape with short pseudopodia extruded from their surfaces.

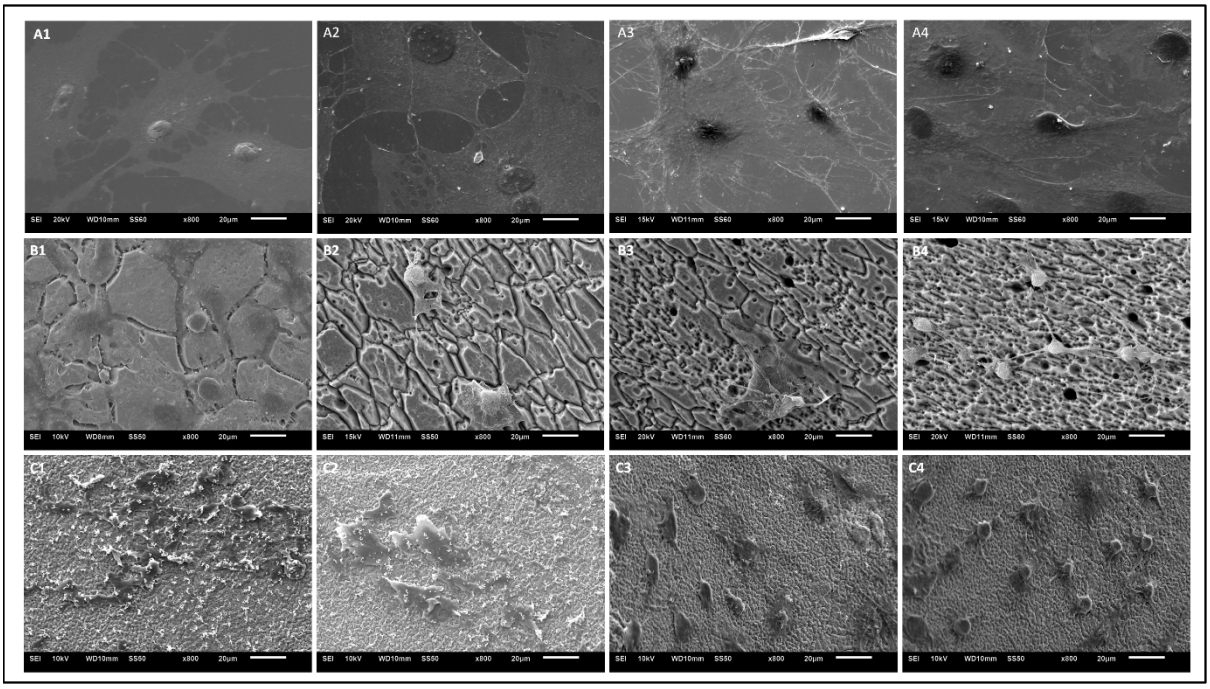

Figure 14: SEM images of MC3T3 cells after 48hrs culturing on A1) Control surface, A2) 40°chip, A3) 20°chip, A4) 0° chip, B1) Chemically treated control Surface B2) Chemically treated 40° chip, B3) Chemically treated 20° chip and B4) Chemically treated 0° chip, C1) Thermally treated control surface, C2) Thermally treated 40° chip, C3) Thermally treatd 20° chip and C4) Thermally treated 0° chip

3.4 DISCUSSION

Machining is a deformation process involving a wedge shaped tool which is advanced against a workpiece at a speed V. In this case, the is effective strain imposed on the material forming the chip is given by:

$$\varepsilon = \cos\alpha / (3\sin\phi \cos(\phi - \alpha) \quad \ldots\ldots\ldots\

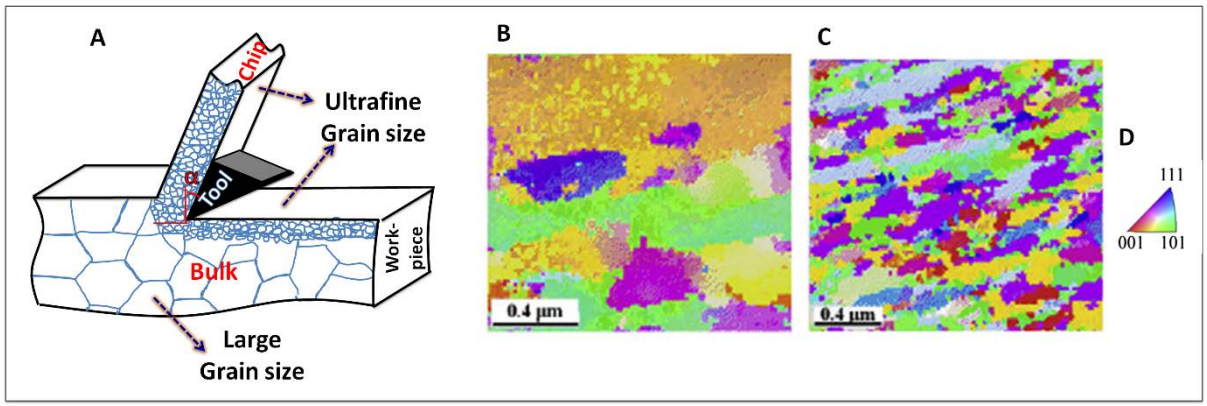

Figure 15: A) Schematic of plane strain machining with α° rake angle, B) OIM map of 20° chip, C) OIM map of 0° chip and D) OIM map legend [58]

Refining the grain size is a well-known technique for strengthening materials. The mechanism of this phenomenon has been explained by Hall-Petch effect. Grain boundaries prohibit dislocation movements storing strains and increasing the material hardness[62]. Wiezorek *et al.* has demonstrated that grain refinement and stored strain is the main reason behind hardness and strength increase in 316L stainless steel after linear plane-strain machining process[58].

In addition to the hardness increase under plane-strain machining SPD technique, the biological functionality of the surface might vary because of refining the grain size in nanometer scale and altering the microstructure. Upon contacting material surface with the biological environment, a layer of water covers the surface. Based on the chemistry and hydrophilicity of the surface, water molecules might be dissociated and form hydroxyl groups on the surface or weakly bind to the surface. Subsequently, ions and proteins presenting in the medium adsorb on the surface. Surface properties (*e.g.*, wettability, chemistry, and topology) determine types, level,

conformational arrangement and binding strength of these molecules on the surface. The focal attachments of cells to the adsorbed molecules induce specific signals transduced to the nucleus and determine the cell behavior [6, 63]. XPS spectra reveal no change in the chemical composition of the surface after SPD process of the plane-strain machining. In the iron XPS region (*i.e.,* 700-730eV), peaks at 707.5eV and 710.9eV are shown corresponding to the Fe element and Fe_2O_3 composition, respectively. In the chromium XPS region (*i.e.,* 560-600eV), the dominating peak at 576.7eV demonstrates the presence of Cr_2O_3 composition on the surface. The peaks at the nickel region including 852.8eV, 854eV and 856.9eV correspond to Ni, NiO and Ni_2O_3 compositions [64, 65]. The presence of these peaks show that an oxide layer forms on the surface. The thickness of this oxide layer should be in the nanometer scale because the elemental iron and chromium is detected in the XPS spectra. According to these observations, this surface oxide is the spontaneous nanometer oxide layer forming on the surface of stainless steel in the ambient air. Surface topography of nanograin chips and coarse-grain sample also revealed no significant difference. Besides, water contact angle did not show statistically significant difference between control sample and nanograin chips. Since surface chemistry and roughness of samples were identical, lack of change in water contact angle after refining the grain size is not unexpected. Results of MTT assay clearly suggest that 0° untreated chip demonstrates the highest MC3T3 cell viability during the short-term and long-term in vitro cell culture among all untreated and treated samples. Cells on untreated samples are in highly flattened form spreading their cytoplasmic extensions in multiple directions without showing any orientation; growth of cells on nanograin samples is higher than coarse-grained sample.

After both chemical and thermal treatment, the peaks corresponding to the elemental Fe and Cr disappear implying growing the oxide layer on the surface. Similar to untreated surfaces,

after thermal and chemical treatment, no difference in the chemical composition of nanograin chips and coarse-grained sample is observed showing that grain structure does not change the chemical composition of grown oxides. Decreasing the water contact angle of samples after surface treatment can be explained by the hydroxyl groups formed on the surface (26). While we did not observe any significant change in the wettability of untreated control sample and nanograin chips, after surface treatment, 0° chip shows the highest amount of decrease compared to control and 40° and 20° chips. While samples show identical surface chemistry, the different surface roughness and topography of nanograin chips after surface treatment cause different surface wettability in them. The drop amount of water contact angle was significantly higher after chemical treatment compared to thermal surface treatment. Different surface topography and chemistry between formed oxides after each treatment should evince this difference. Guillamet *et al.,* studied the surface structure of austenitic stainless steel after heat treatment in 900-1100°C temperatures for 5-15min duration. They demonstrated αFe_2O_3, Cr_2O_3 and the spinel oxide close to $MnCr_2O_4$ are the main compositions of thermally treated samples. In our study, XPS results of thermally treated samples also shown in addition to the presence of peaks corresponding to Fe_2O_3 and Cr_2O_3, a new peak appears in 638-648eV region corresponding to manganese enrichment on the surface [60]. In thermally treated surfaces, cell viability decreases compared to the native stainless steel oxide, this observation may be due to the difference in surface chemistry of these oxides and appearance of manganese oxide composition on the surface. Jang *et al.,* demonstrated that the incorporation of manganese composition into the surface titanium oxide layer diminishes osteoblast cell behavior [66].

After chemical treatment, the surface roughness remarkably increases and the island-like structure uniformly appears on the surface [67]; however, the size of islands significantly

decreases via reducing the grain size. Vorobiev *et al.*, suggested an explanation for this observation such that grain boundaries actively undergo anodic dissolution and cathodic reaction occurs in the grains and oxide film grows on the surface [68]. Therefore, refining the grain size provides more grain boundaries covering the surface with small islands resulting in an entirely rough surface for 0° nanograin surface.

It is expected that growing a stable surface oxide enhances the corrosion resistance and prevents toxic ion release [69, 70]. However, it is shown that the oxide film formed by chemical treatment results in an island-like structure with a non-uniform chemical composition and porosity within its depth (chromium-enriched surface). Therefore, chemically formed oxide on stainless steel reduces the corrosion resistance compared to the passive oxide naturally formed on the surface [67].

Cell morphology on the naturally passive oxide and chemically formed oxide is significantly different. While cells on untreated nanograins and the control sample entirely spread on the surface, in chemically treated samples, cells are in polygonal morphology and attached on the surface using long cytoplasmic projections. This different morphology of MC3T3 osteoblast cells might be because of the change in cellular phenotype [71]; therefore, more cell studies needed to explain this behavior.

3.5 SUMMARY AND CONCLUSION

Ultra-fine grain 316L stainless steel samples were prepared by severe plastic deformation (SPD) using linear plane-strain machining technique. Samples were prepared in three different average

grain sizes in nanoscale range by using three different rake angles (*i.e.*, 0°, +20° and +40°). Vickers microhardness was significantly increased after refining the average grain size. Oxide layers were grown on nanograin chips by chemical and thermal treatment. To systematically examine the naturally, chemically and thermally grown oxides on nanograin samples**,** surface roughness, topography, wettability and chemical composition of surfaces were characterized. Surface roughness and water contact angle (*i.e.*, index of wettability) of nanograin and coarse grain samples remained in similar ranges of 3-20nm and ~70°, respectively. XPS results showed a natural oxide formed on nanograin samples with similar composition of the oxide formed on the coarse grain sample. After chemical treatment, a chromium enriched oxide with island-like topography formed on the surface and the wettability of surface significantly increased (*i.e.*, contact angle ~ 10-30°). Refining the grain size creates oxides with smaller island-like structures showing rougher and more hydrophilic surfaces. After thermal treatment, micro-size oxide grains formed on the surface, the distribution of these grains became more uniform in nanograin samples with smaller average grain size. Manganese oxide compositions intensified in the composition of the thermally oxide layer formed on the surface. The viability and morphology of MC3T3 cells were studied on surfaces. The results of MC3T3 cell culture showed greatly improved cell adhesion and growth on the native passive oxide formed on 0° chip with the smallest grain size. Oxide formed on the surface of untreated samples demonstrated higher biocompatibility compared to both thermally and chemically treated surfaces.

4.0 TECHNIQUE 2: RAPID ELECTROSTATIC ENDOTHELIAL CELL SEEDING ON THIN FILM NITINOL

4.1 INTRODUCTION

Cardiovascular diseases (CVDs) are known the leading cause of death in the United States, a major part of this group of diseases are associated with morbidity in small-size blood vessels (*i.e.*, <6mm)[72, 73]. For instance, coronary artery disease (CAD) is recognized the most common type of CVDs that leads to 380’000 deaths in the US, annually[74]. CAD is accounted for 1 in 4 deaths in the US and about $108.9 billion cost was estimated regarding to it[75]. Figure 16 shows the schematic of coronary artery occlusion by plaque (*i.e.*, atherosclerosis) that inhibits transferring sufficient oxygen and nutrition to the cardiac muscle.

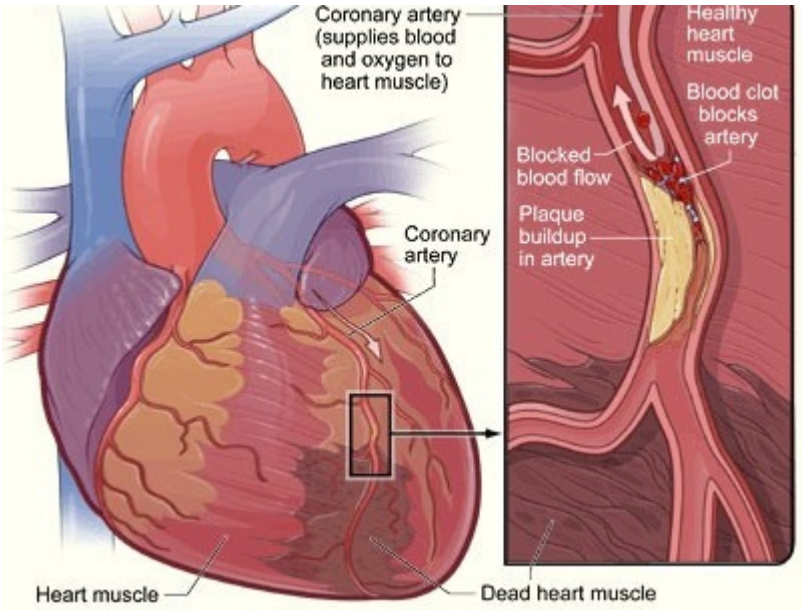

Figure 16: The heart damage in coronary artery disease resulted from blockage of a coronary artery[38]

Occlusion in small cerebral blood vessels and peripheral arteries are two other prevalent examples of small-size vascular diseases which result in disorder in providing the blood to the brain and lower extreme organs (*e.g.*, kidney, stomach and legs), respectively [76-79]. About 8 million Americans are affected by peripheral artery disease (PAD). It is claimed that the number of PAD around the world had a 23.5% rise from 2000 to 2010[80]. PAD occurrence increases with age and if it is left untreated, it might result to limb amputation; the risk of stroke and heart attack increases too. Bypass surgery is the typical treatment method to restore the blood flow in occluded vessels. In this surgery, a healthy blood conduit (*i.e.*, autologous vessel) is supplied from another part of the body and is placed around the blocked artery. Autologous vessels, including saphenous veins and mammary arteries, remained the gold standard for coronary grafting. The saphenous vein has been extensively utilized as a vascular graft because of its

length and diameter, which are similar to those of coronary and femoral or popliteal arteries [81-83]. Despite the high efficiency of autologous vascular grafts, there is limitations in providing needed amount of them such that patients might have not sufficient healthy veins for grafting owing to preexisting vascular disease or using healthy veins for previous surgeries[84]. Preparation of vascular graft from some other autogenous sources such as skin, pericardium or intestine have been examined but the results were not promising owning to early thrombosis, rupture or aneurysm occurrence[85, 86]. Arterial and venous allogenic grafts have been used as substitutes for small vascular grafts but the inflammatory reaction, calcification and limited availability are the major restricting factors for allografts. Xenograft has also been limited due to aneurysm formation, infection, thrombosis, calcification and risk of disease transmission and rejection [85, 86]. Therefore, to meet the high demands for vascular grafts, synthetic materials were also tested to develop vascular grafts. Among synthetic materials, expanded polytetrafluoroethylene (e-PTFE) and Polyethylene terephthalate (Dacron©) are two known polymers that are successfully used as vascular grafts. E-PTFE is an inert polymer with an electronegative charged luminal surface (similar to endothelium layer in the native blood vessel) that is antithrombotic and demonstrated patent results for lower limb bypass grafts (7–9 mm) and Dacron© demonstrated excellent result in large-diameter vascular grafts. However, both e-PTFE and Dacron© showed poor patency rates as small-caliber vascular grafts[86]. In a randomized trial to compare the PTFE with saphenous vein for femoropopliteral bypass, after 54 months, the patency rate for PTFE and saphenous vein is reported 37% and 70% respectively while after 6 weeks both were 92%[87]. Implanted e-PTFE and Dacron© graft do not develop an endothelialized lumen spontaneously, leading to adhesion of platelets and development of a luminal fibrin layer that can lead to thrombosis.

In addition to thrombosis, other causes of vessel narrowing, such as intimal hyperplasia expedite the occlusion. Occurrence of thrombosis and restenosis result in the failure of vascular grafts in short term such that approximately 600’000 percutaneous coronary procedures are performed annually in the United States and nearly 25-40% of initially successful of these procedures fail within one year[88].

Neointimal hyperplasia refers to proliferation and migration of vascular smooth muscle cells resulting in the thickening of arterial walls and decreased arterial lumen space (Figure 17). Damage to the arterial wall creates a series of biochemical events that lead to the recruitment of inflammatory cells, proliferation and migration of vascular smooth muscle cells, and collagen deposition and finally restenosis occurrence. The restenosis results in critical narrowing in 30% to 50% of patients after vascular grafts implantation[89].

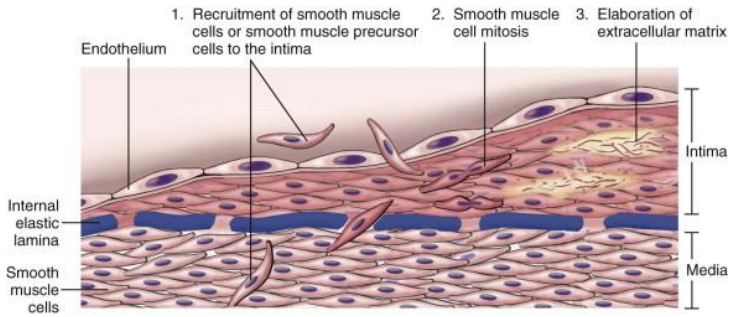

Figure 17: Schematic of vascular smooth muscle cells migration and neointimal hyperplasia occurrence[90]

Native blood vessels contain multiple cellular layers and this structure provides mechanical elasticity and a thrombo-resistant surface for blood vessels. Figure 18 shows the schematic structure of arteries including intima (squamous endothelial cells), media (vascular

smooth muscle) and adventitia (connective tissue). The endothelium in the intima layer plays an active role in preventing the thrombosis and platelet adhesion through providing a thrombo-resistant barrier between blood and arterial wall; furthermore, it releases chemicals to control thrombosis, platelet activation and smooth muscle cells migration and proliferation leading to maintaining hemostasis through chemical regulation for example normal endothelial cells release nitric oxide that has an active role in maintaining the vascular hemostasis and preventing neointimal hyperplasia[91]. Therefore, the lack of endothelialization in the surface of synthetic vascular grafts or the native endothelium injury that occurs in percutaneous procedures during endovascular deployment result in increasing the thrombosis potential and restenosis and finally failure of the treatment.

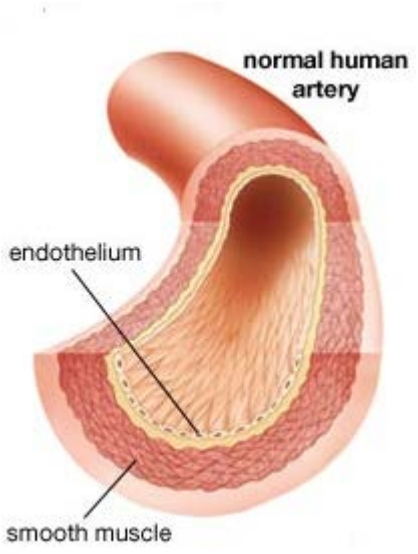

Figure 18: Schematic of artery structure[92]

Therefore, covering the surface of the vascular grafts with a layer of endothelial cells as exists in the intima layer of the native blood vessel is an strategy that is used to decrease the thrombosis[93-95]. Seeding the endothelial cells on the synthetic grafts first reported by Herring *et al.* for 6–mm Dacron© grafts[96]. The Endothelial seeding enhanced the patency rate after 4 weeks to more than 3 times (76% vs. 22%). However, multiple limitations exist in endothelial cell seeding such as poor retention of the cells on the surface of biomaterials under blood flow shear stress, low degree of adhesion of cells, limitation of available cells number and time duration for harvesting and incubating cells to grow. Using biological glues such as the modification and coating of the surface with RGD (Arginyl-Glycyl-Aspartic acid) peptides, matrix proteins (*e.g.,* fibronectin), growth factors or a combination of them is used to enhance the adhesion of endothelial cells but there are concerns about arising the thrombogenicity of the surface[97, 98].

Electrostatic cell seeding is an alternative technique to improve the efficiency of cell seeding in terms of number of attached cells and the amount of cell adhesion. In this method, a positive electrostatic charge is temporarily induced on the surface of the graft to promote endothelial cell adhesion. Biomaterials with an electrically charged surface have been studied and it is demonstrated that the adhesion of endothelial cells is enhanced on the electrically charged substrates[99]. Bowlin *et al.,* suggested using electrostatic force to seed the endothelial cells inside the small diameter e-PTFE tubes, they demonstrated the endothelial cell maturation accelerated and cell retention after implantation enhanced[100-102]. They developed a system for seeding the endothelial cells on the e-PTFE vascular graft via electrostatic force. The system is a capacitor-like structure which consists of an internal conductor within the graft. The ends of the graft are sealed around the internal conductor. The external conductor consists of a stainless

steel cylinder that was bored centrally and placed around the graft such that the internal electrode is placed at the center of it (Figure 19A). An electrical potential is applied across the internal and external conductors to induce a positive luminal surface electrostatic charge on the vascular graft as the dielectric material within the capacitor. Figure 19B shows the schematic of capacitor model of electrostatic endothelial cell seeding on the e-PTFE vascular graft. A temporary positive electrical charge was induced on the e-PTFE surface as the positive electrically charged electrode and endothelial cells which have negative electrical charge deposit on it. They found the optimal electrostatic transplantation conditions (+1V voltage and 16min duration) and exposure of cells to this system under optimal condition led to seeding efficiencies of up to 90% [101].

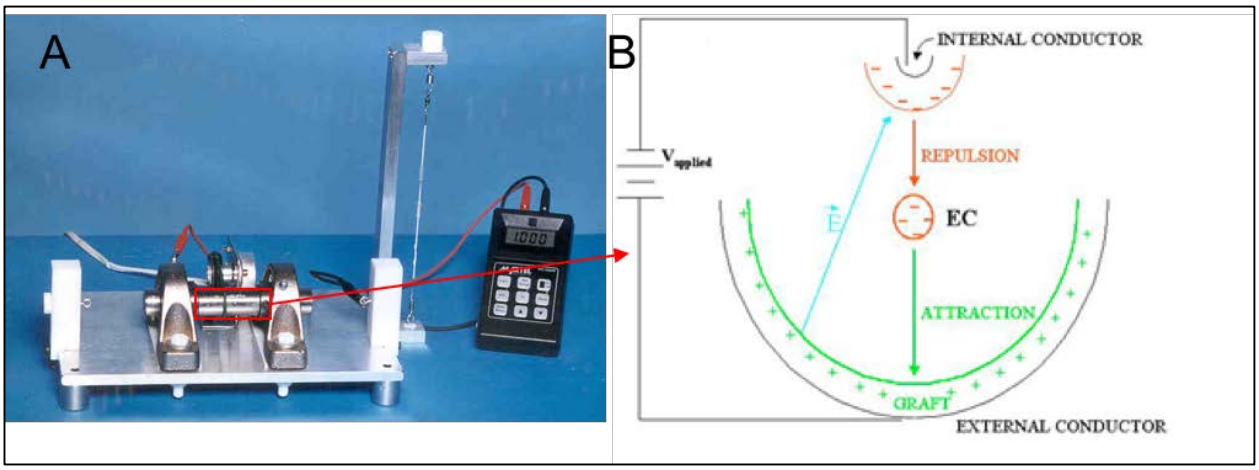

Figure 19: A) Electrostatic cell seeding set-up for e-PTFE graft, B) Capacitor model for electrostatic endothelial cell seeding[101]

In this study, the goal is to accelerate the endothelial cell seeding and improve the adhesion and growth of the seeded cells on the surface of thin film nitinol using electrostatic transplantation technique. This cell seeding procedure is aimed to perform on the thin film nitinol deployed inside the intravascular catheter right before the endovascular surgery. This study suggests a novel *in vitro* system for the rapid endothelialization of thin film nitinol. Advantages of thin film nitinol such as superelasticity, low profile and grown hemocompatible oxide on its surface along with the presence of a uniform endothelial layer on its surface candidate it as a promising endovascular graft for the treatment of small-diameter vascular diseases.

4.2 METHODS

4.2.1 Design, manufacture and test of electrostatic endothelial cell transplantation device

Thin film nitinol was deposited on silicon wafer using DC sputter deposition technique. The sputter chamber pressure and the argon pressure were kept 5×10^{-8} and 1.5×10^{-3}Torr, respectively. A 10nm thick native oxide layer forms the surface of thin film nitinol and by using a chemical surface treatment as explained in the introduction section (1.1.2), a 100nm titanium oxide grows on the surface[103]. Water contact angle significantly enhances after chemical treatment because of the grown oxide layer; therefore, a superhydrophilic surface is gained after the surface treatment. Untreated and superhydrophilic thin film nitinol were used as negative and positive electrodes, respectively.

The dimension of electrodes was 3mm×3mm and they were fixed parallel to each other with 2mm distance in a 24-well tissue culture plate (Figure 20A). The substrate with positive induced electric charge was placed at the bottom of the culture plate and connected to the power supply via copper wire (Figure 20A). The distance between two parallel electrodes was filled with the cell suspension solution.

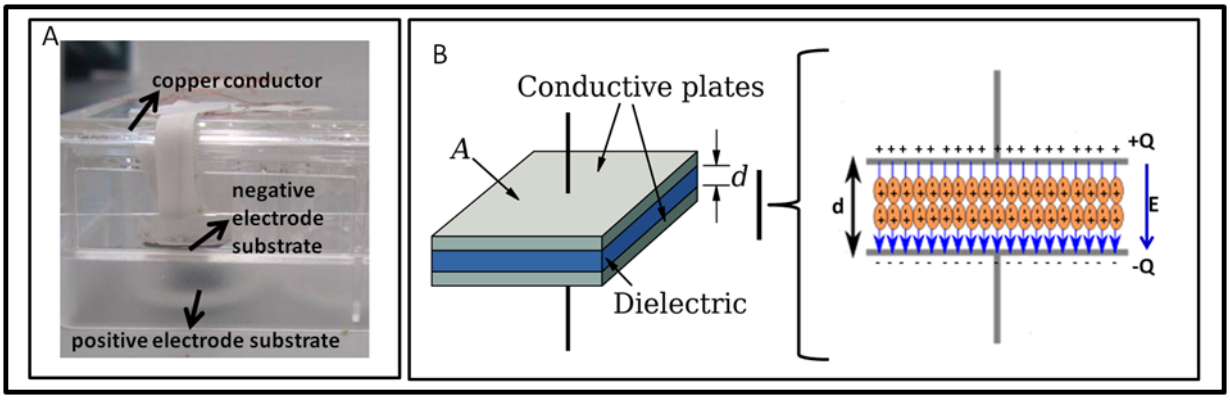

Figure 20: A) Parallel capacitor set-up, B) The schematic of induced electric charge and electrical field in a parallel capacitor

The induced electric charge (Q) on the electrode surface and the induced electric field (E) (Figure 20B) were estimated using the following equations:

$$Q=C\times V \qquad (2)$$

$$E=\frac{V}{d} \qquad (3)$$

Where V is the applied voltage, d is the distance between two electrodes and C is the total capacitance which is defined by:

$$C = \frac{k\varepsilon 0 A}{d} \quad (4)$$

where ε_0 is the permittivity constant (8.85×10^{-12}), A is the surface area of electrodes and k is the dielectric constant which is around 80 for the cells suspension medium. We can consider the cells suspension medium as the dielectric since no electric current was recorded during the experiment. We neglect the capacitance of the surface oxide layer due to the trivial thickness of native and grown oxide (*i.e.,* nanometer scale) against 2mm distance. Based on the above equations, the induced electric charge and electric field in each experiment are calculated.

In the second prototype, the thin film nitinol was deployed inside the 6Fr catheter and the catheter was placed in a microincubator providing a temperature of 37°C and 5% CO_2 pressure. The catheter was connected to a flow loop containing a small pulsatile pump creating a flow of endothelial cell suspension medium. The nitinol wire passed from the center of microcatheter while the thin film nitinol was rolled inside the catheter. Two sides of the catheter were perfectly sealed (Figure 21). One end of nitinol wire was connected to the negative terminal of voltage supply and one side of the thin film nitinol which faced the catheter wall contacted with copper conductor connecting to the positive terminal of the power supply ensuring no electrical connections existed between the components.

To evaluate the induced electric field (E) and electric charge (q) between the electrodes in the cylindrical capacitors, Gauss' law is used according to the following equations:

$$\int \mathrm{E}.\,\mathrm{dA} = \frac{\sum \mathrm{q}}{\varepsilon 0} \tag{5}$$

$$\mathrm{E} = \frac{\mathrm{q}}{2\pi \mathrm{r} \mathrm{L} \varepsilon 0} \tag{6}$$

$$\mathrm{V} = \int_{\mathrm{a}}^{\mathrm{b}} \mathrm{E}.\,\mathrm{dr} = \frac{\mathrm{q}}{2\pi\varepsilon 0} \left(\ln \frac{\mathrm{b}}{\mathrm{a}}\right) \tag{7}$$

$$\mathrm{C} = \frac{2\pi\varepsilon 0 \mathrm{L}}{(\ln \mathrm{b}/\mathrm{a})} \tag{8}$$

where A is the cylindrical surface with length L and diameter r, V is the electrical potential and C is the capacitance.

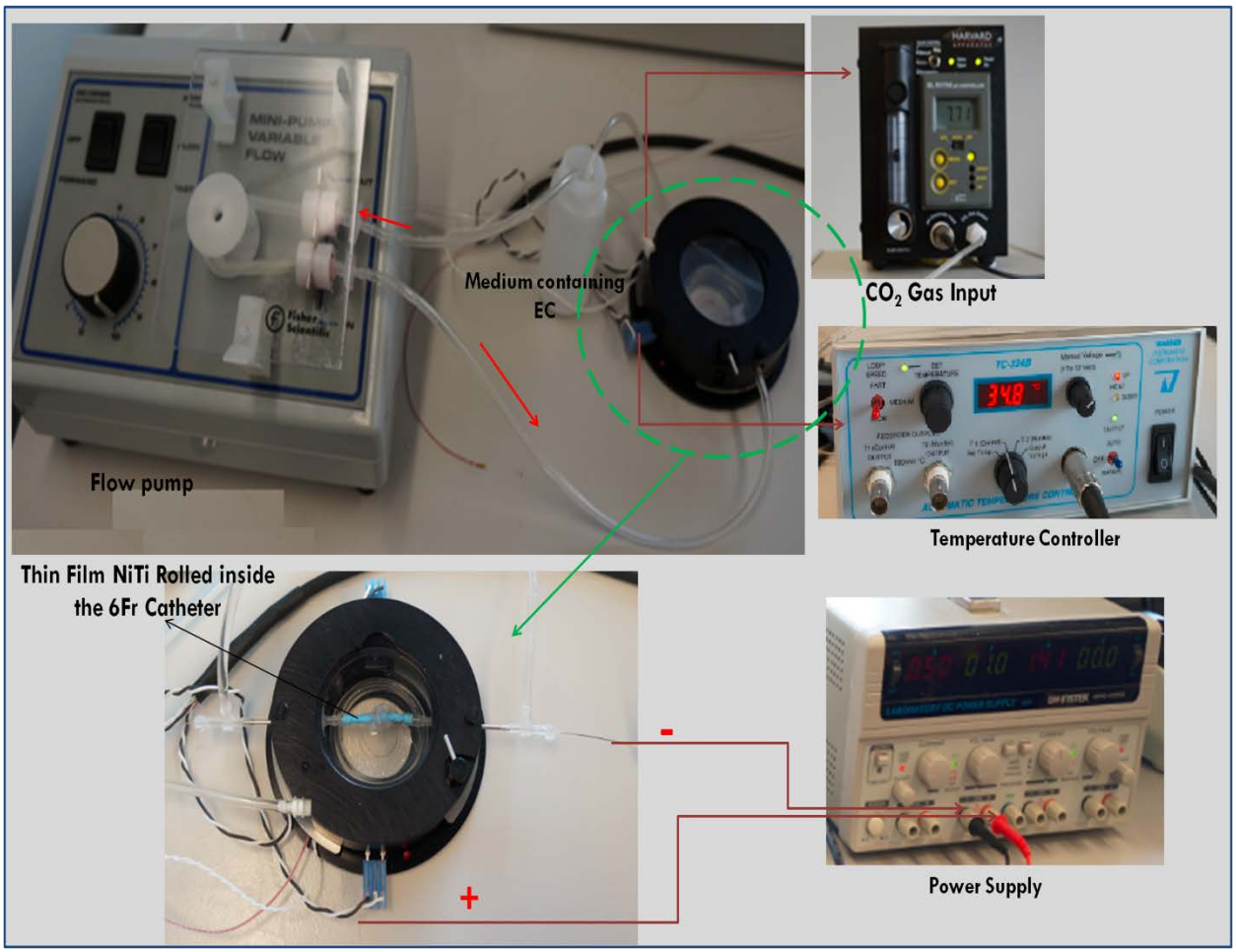

Figure 21. Components of electrostatic endothelial cell seeding on the thin film nitinol placed inside the 6Fr catheter

4.2.2 Experimental design

To simultaneously evaluate multiple factors which can affect the level of cell seeding and behavior of seeded cells, the Taguchi method is used to design the experiments. Taguchi method remarkably reduces the number of experiments that are required to model the response function compared with the full-factorial design of experiments. The parameters which can potentially

affect this electrostatic cell seeding process include: the cell suspension solution, the substrate chemistry, applied voltage and the incubation time. The voltage value determines both induced electric field and electrostatic charge. The range of values of these parameters is given in Table 1. For both voltage and time parameter, four levels will be taken and for each of suspension solution and substrate chemistry parameters, two levels will be considered.

Table 2: Electrostatic cell seeding parameters and their levels

Level	Time (hrs)	Voltage (V)	Suspension solution	Substrate
1	0	0.1	PBS	TFN
2	2	1	Cell medium solution	STFN
3	6	3	----	----
4	24	6	----	----

In addition to the above mentioned experiments which were performed in the parallel capacitor-like set-up, in cylindrical capacitor-like intravascular catheter set-up which have been explained above, experiments in 1V, 5V and15V were performed in cell medium suspension solution. These experiments were performed on superhydrophilic thin film nitinol substrate for 30min duration and the analysis was performed right after the experiment (*i.e.*, no incubation time).

Analysis of variance (ANOVA) technique will be performed to identify the significant factors that affect the number of attached cells.

4.2.3 Testing the morphology, attachment and the viability of seeded endothelial cells

BAEC (Bovine Aortic Endothelial Cells; Lonza, NJ, USA) were grown in the medium consisting of Endothelial Cell Basal Medium (EBM)-2 (Lonza, NJ, USA) and EGM-2 SingleQuot Kit Suppl. & Growth Factors including (Hydrocortisone 0.02%, FBS2%, VEGF0.05%, hFGF-B2%, IGF-1 0.05% and HEGF 0.05%, GA-1000 0.05%) (Lonza, NJ, USA). These cells at passage number 9 at a density of 2×10^5 cells/cm^2 were suspended in the medium solution or PBS solution. After electrostatic cell seeding, the samples were rinsed thoroughly with PBS and stained with Calcein AM (life technologies™, NY, USA). Three samples in each condition were used and in each sample five spots were randomly picked and the number of attached live cells were counted and used for the analysis (*i.e.*, totally 15 images).

Besides, LIVE/DEAD® cell viability assay (Life technologies, NY, USA) are performed to determine the live attached cells and dead cells using fluorescent microscopy (Olympus BX43, PA, USA). Both morphology and proliferation of adhered cells were evaluated using SEM after sputtering a thin layer of palladium (Pd). For SEM imaging, cells were fixed with 2.5% glutaraldehyde **(**Sigma-Aldrich**,** MO, USA), dehydrated in a series of ethanol/DI water mixtures including 30%, 50%, 75%, 90% and 100% ratios, then, subjected to drying with hexamethyldisilazane (HMDS) (Alfa Aesar, MA, USA)/ethanol in 3:1, 1:1 and 1:3 volume ratios. The samples were then dried in the chemical hood overnight at room temperature.

4.3 RESULTS

4.3.1 Electrostatic endothelial cell seeding in parallel capacitor-like set-up

Since we have two 4-level control factors (*i.e.,* Time and voltage) and two 2-level control factor (*i.e.,* cell suspension solution and substrate), Qualitek-4 software (software for automatic design and analysis of Taguchi experiments) has selected L-16 array without considering the interactions. The experiemental plan is shown in the Table 3, each row of this table shows an experiment with different combination of the parameters levels.

Table 3: Experimental plan using L-16 orthogonal array

Experiment number	Time (hrs)	Voltage (V)	Solution	Substrate
1	0	0.1	Cell medium	TFN
2	0	1	Cell medium	TFN
3	0	3	PBS	STFN
4	0	6	PBS	STFN
5	2	0.1	Cell medium	STFN

Table 3(continued)

6	2	1	Cell medium	STFN
7	2	3	PBS	TFN
8	2	6	PBS	TFN
9	6	0.1	PBS	TFN
10	6	1	PBS	TFN
11	6	3	Cell medium	STFN
12	6	6	Cell medium	STFN
13	24	0.1	PBS	STFN
14	24	1	PBS	STFN
15	24	3	Cell medium	TFN
16	24	6	Cell medium	TFN

The results of induced surface electrostatic charge in each of Taguchi designed experiments have been calculated based on the formula (1-3) and demonstrated in Table 4.

Table 4: Induced electrostatic charge and electrical field in the designed experiments

Experiment number	Electrostatic charge (μC)	Electrical field (V/m)
1	3.18×10^{-7}	50

Table 4 (Continued)

2	3.18×10^{-6}	500
3	9.54×10^{-6}	1500
4	1.9×10^{-5}	3000
5	3.18×10^{-7}	50
6	3.18×10^{-6}	500
7	9.54×10^{-6}	1500
8	1.9×10^{-5}	3000
9	3.18×10^{-7}	50
10	3.18×10^{-6}	500
11	9.54×10^{-6}	1500
12	1.9×10^{-5}	3000
13	3.18×10^{-7}	50
14	3.18×10^{-6}	500
15	9.54×10^{-6}	1500
16	1.9×10^{-5}	3000

The representative fluorescent imaging of attached Calcein AM stained endothelial cells under conditions determined in the designed experiments for parallel capacitors is shown in Figures 22, 23, 24 and 25. For each condition, a representative fluorescent image of the control sample (*i.e.*, the similar condition but without applying voltage) is shown as well.

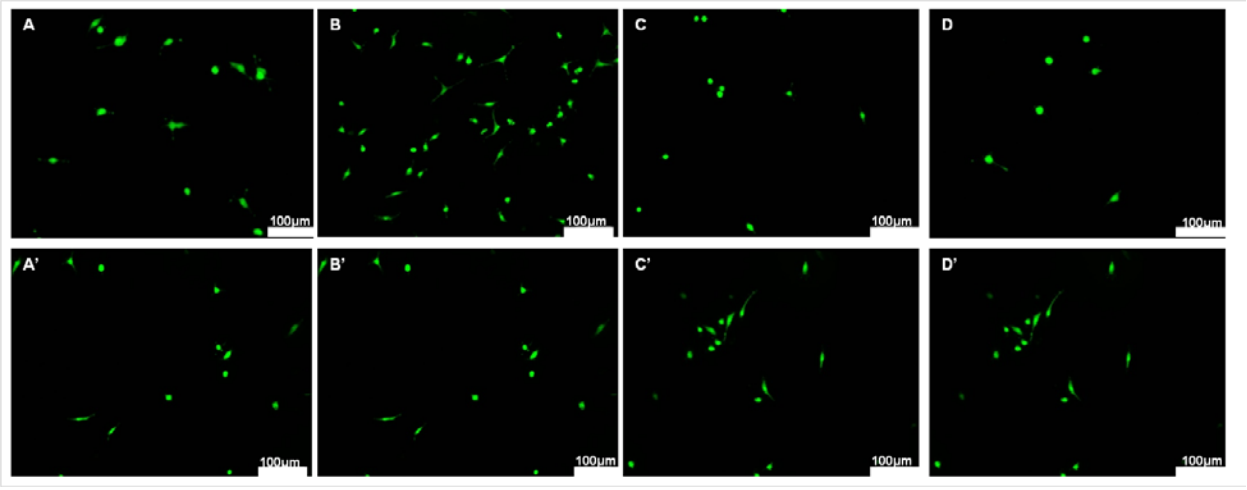

Figure 22: Representative fluorescent images of Calcein AM stained cells on STFN substrate in cell medium solution: A) 0.1V-2hrs, B) 1V-2hrs, C) 3V-6hrs, D) 6V-6hrs; A' and B') 0V-2hrs (control for A and B), C' and D') 0V-6hrs (Control for C and D)

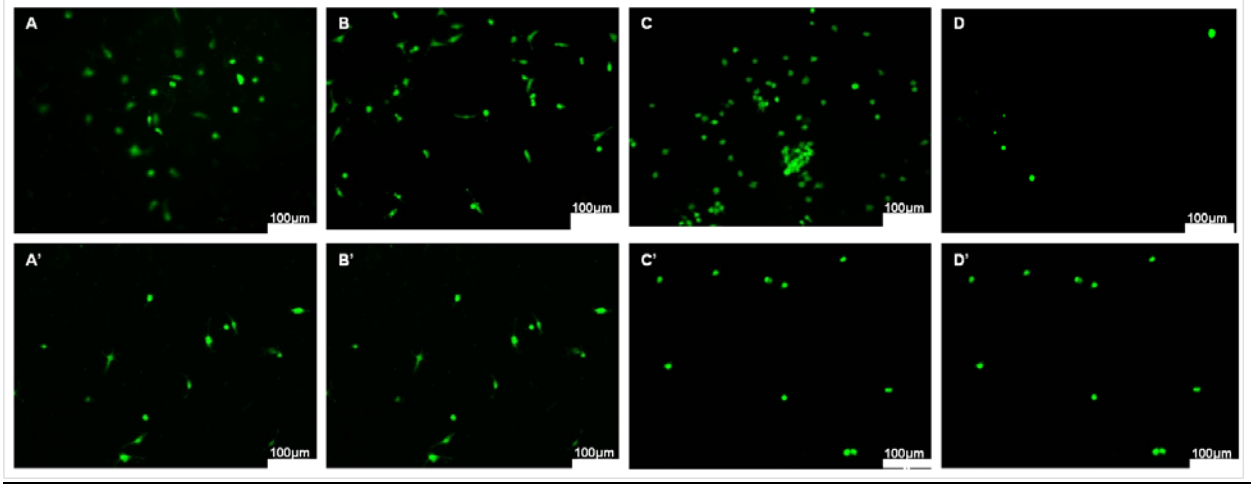

Figure 23: Representative fluorescent images of Calcein AM stained cells on STFN substrate in cell medium solution: A) 0.1V-2hrs, B) 1V-2hrs, C) 3V-6hrs, D) 6V-6hrs; A' and B') 0V-2hrs (control for A and B), C' and D') 0V-6hrs (Control for C and D)

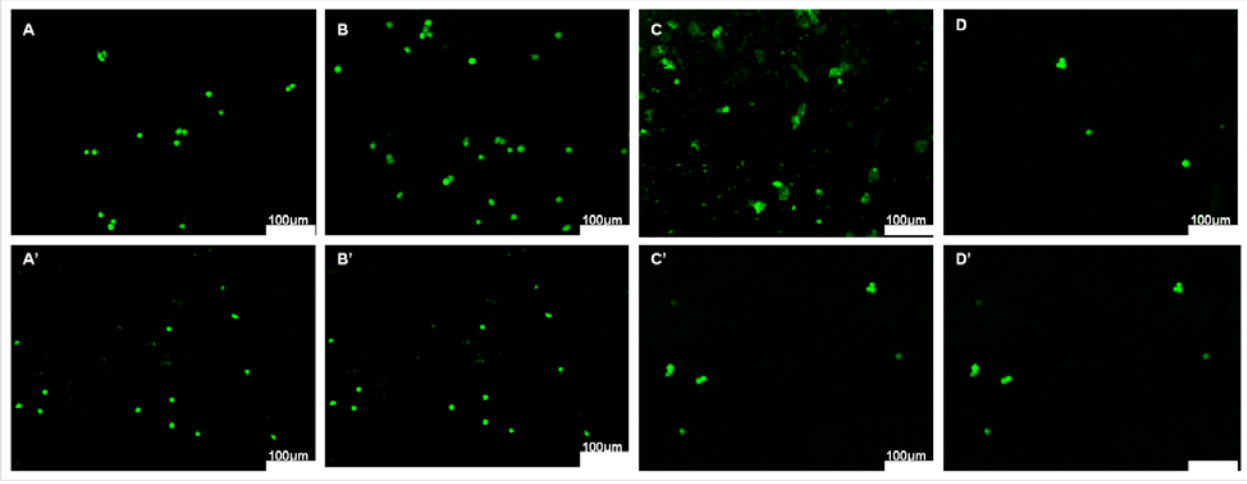

Figure 24: Representative fluorescent images of Calcein AM stained cells on TFN substrate in cell medium solution: A) 0.1V-0hr, B) 3V-24hrs, C) 6V-24hrs, D) 6V-6hrs; A' and B') 0V-0hr (control for A and B), C' and D') 0V-24hrs (Control for C and D)

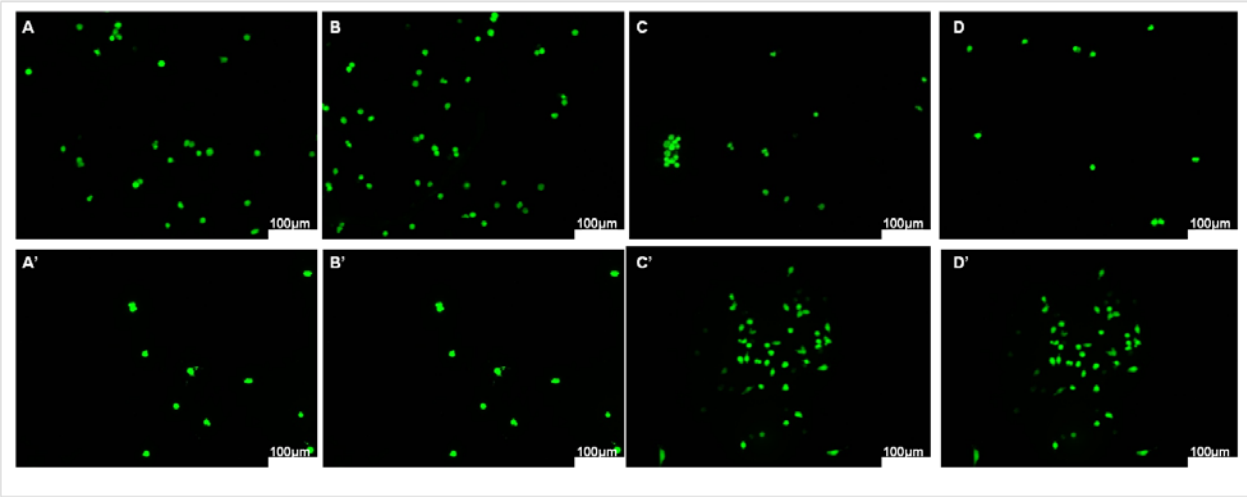

Figure 25: Representative fluorescent images of Calcein AM stained cells on TFN substrate in PBS solution: A) 0.1V-6hrs, B) 1V-6hrs, C) 3V-2hrs, D) 6V-2hrs; A' and B') 0V-6hrs (control for A and B), C' and D') 0V-6hrs (Control for C and D)

Qualitek-4 software uses the results of the fluorescent imaging in each experimental condition described in Table 3 and the effect of changing the electrostatic cell seeding independent parameters (*i.e.*, voltage, time, substrate chemistry and the suspension solution) on the average number of attached cells per mm^2 were analyzed based on standard statistical analysis. The results of the average number of attached cells per mm^2 are shown in Figure 26 while the levels of each parameter are changed. The average number of attached cells per mm^2 slightly increases on superhydrophilic thin film nitinol (~48) compared to untreated thin film nitinol (~41) (Figure 26A). The average number of attached cells per mm^2 increases through changing the voltage from 0.1V up to 1V and it reduces by decreasing the voltage from 1V to 6V; therefore, the average number of attached cells per mm^2 is the highest in 1V (Figure 26B). The result of the average effect of the cell suspension solution on the number of attached cells in Figure 26C shows that this value is slightly higher in cell medium solution (~49) compared to it in the PBS solution (~40). Ultimately, Figure 26D shows the effect of the time parameter. The diagram trend line shows that the average number of cells increases over time as expected.

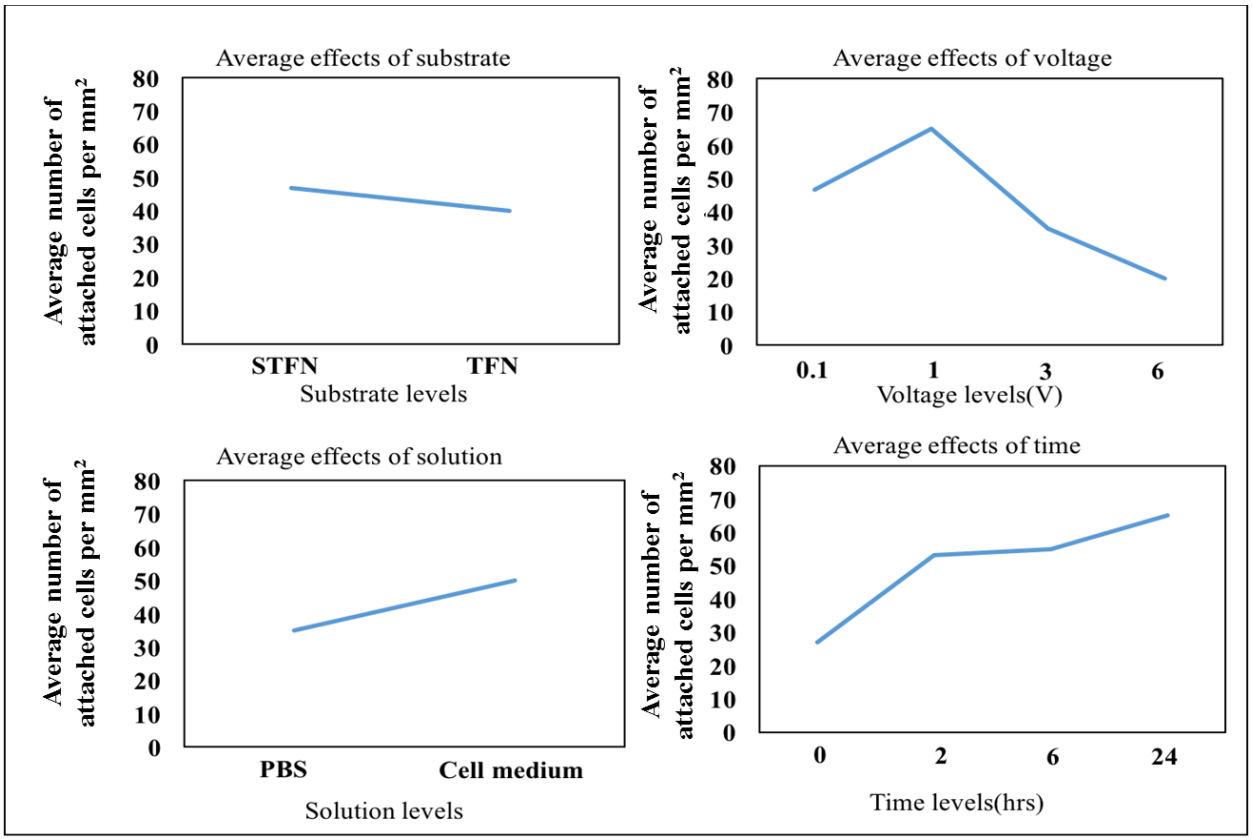

Figure 26: Diagram of average effect A) substrate, B) voltage, C) cell suspension solution and D) time duration on the number of attached cells per mm^2

Analysis of variance (ANOVA) technique was performed to identify the significant factors that affect the number of attached cells. Thus, voltage and time with contribution percentage 34.4% and 36.1% and F-ratio of 25.17 and 26.37 were respectively identified as the two dominant factors. While cell suspension solution shows 5.56% contribution with F-ratio of 12.6 and the substrate parameter shows 0.97% contribution with F-ratio of 3.03 (critical F-ratio ,$F^{*}_{2,3,0.05}$ =9.55). Sources of errors including the variability within the groups or unexplained random error contribute 22.3% of results.

SEM images in Figure 27A show endothelial cells attached on STFN substrate after 2hrs incubation in the cell medium show a few nanospikes emerging on the rounded-up cell bodies but upon applying 0.1V, the number and length of these nanospikes significantly increase (Figure 27B) while under 1V with the same condition, these cells become noticeably flat on the surface (Figure 27C).

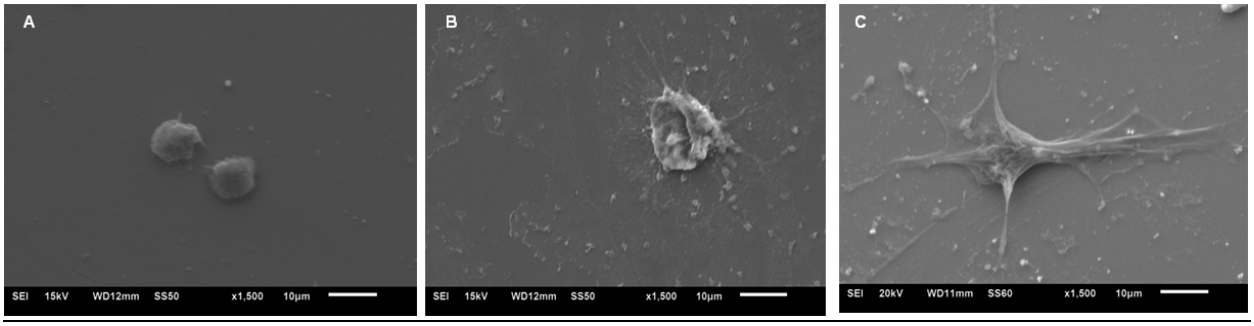

Figure 27: Representative SEM images of attached endothelial cells on STFN substrate in the cell medium solution after 2hrs under A) 0V (Control), B) 0.1V and C) 1V

By increasing the incubation time from 2hrs to 6hrs, the cell morphology presumably becomes more flat and the nanospikes emerging on the surface remarkably lengthens (Figure 28A). Applying 3V causes cells to become more flat but cell membrane pitting significantly occurs indicating the cell damaging (Figure 28B). By increasing the voltage up to 6V, the level of disintegration and pitting in cell membrane significantly increases (Figure 28C).

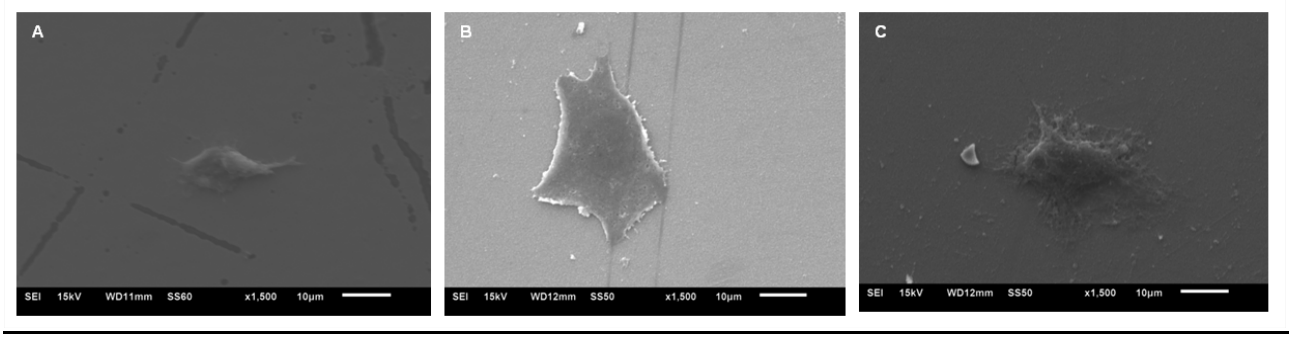

Figure 28: SEM images of attached endothelial cells on STFN substrate in the cell medium solution after 6hrs under A) 0V (Control), B) 3V and C) 6V

Similar to STFN substrate, the cell membrane damage (*i.e.*, cell membrane disintegration and pitting) under 6V, has been also observed in TFN substrate in both PBS and cell medium solutions (Figure 29B and Figure 30B) while no cell membrane damage was observed in TFN substrate under 3V (Figure 29A and 30A).

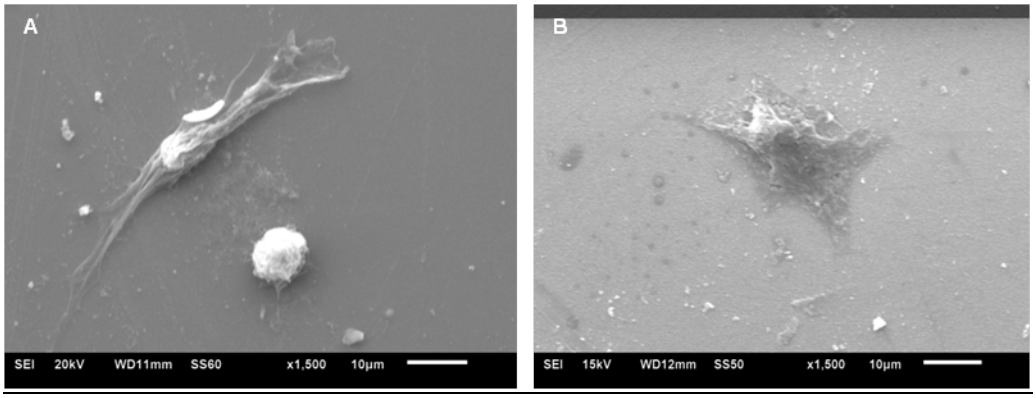

Figure 29: SEM images of attached endothelial cells on STFN substrate in the cell medium solution after 6hrs under A) 0V (Control), B) 3V and C) 6V

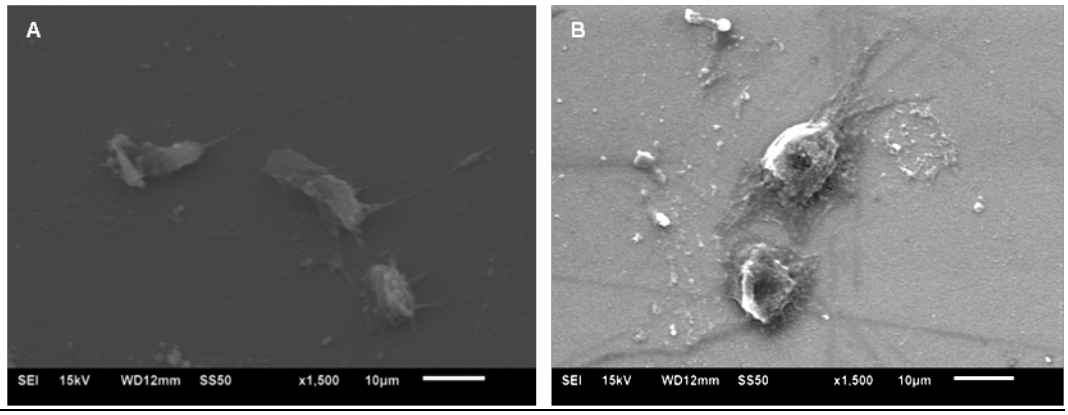

Figure 30: SEM images of attached endothelial cells on TFN substrate in PBS solution under: A) 3V-2hrs and B) 6V-2hrs

4.3.2 Electrostatic endothelial cell seeding in intravascular catheter

Table 5 shows the value of applied electrical voltage, induced electrical field and the induced electrostatic charge on the STFN substrate placed in the cylindrical capacitor set-up of the intravascular catheter. Induced electrostatic charge and electric field is noticeably higher in the parallel capacitor set-up compared to the cylindrical capacitor set-up of the intravascular catheter, for instance, under 1V voltage, the induced electric field in parallel capacitor set-up, and intravascular catheter set-up is 500V/m, 1.022 V/m, respectively.

Table 5: Electrostatic cell seeding experiments

Experiment number	Voltage(V)	Electrostatic charge (μC)	Electrical field (V/m)
1	1	0.136×10^{-6}	1.022
2	5	0.68×10^{-6}	5.11
3	15	2.04×10^{-6}	15.33

Figure 31 shows the Live/Dead assay results and the SEM images of attached cells on superhydrophilic thin film nitinol substrate placed in intravascular catheter set-up while 1, 5 and 15V is applied. Figure 32 demonstrates the fluorescent intensity of live attached cells under 1, 5 and 15V. Number of attached live EC increases under 1V and 5V while the number of live cells under 15V significantly decreased compared to control condition (0V). The highest number of attached cells is observed in 5V condition. The morphology of cells under the condition of applying electrical voltage is similar to the control sample but under 5V, multiple podia form on the surface of cell showing the advancement of cell maturation in this condition.

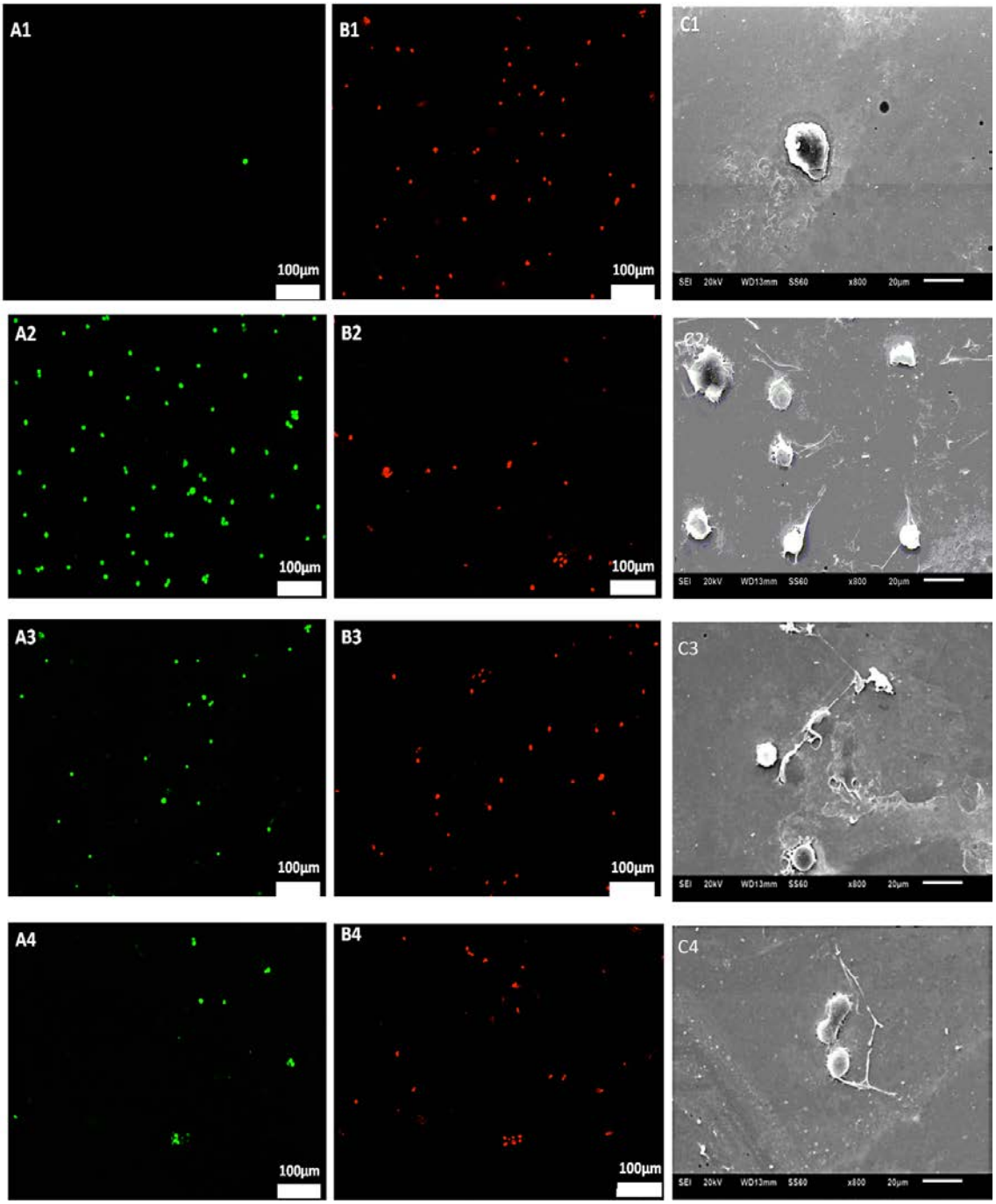

Figure 31: Live/Dead® cell viability assay of endothelial cells on the STFN substrate: under A1-B1) 15V, A2-B2) 5V, A3-B3) 1V and A4-B4) 0V (control) and SEM images of endothelial cells on the STFN substrate: C1) 15V, C2) 5V, C3) 0.5V and C4) 0V(control)

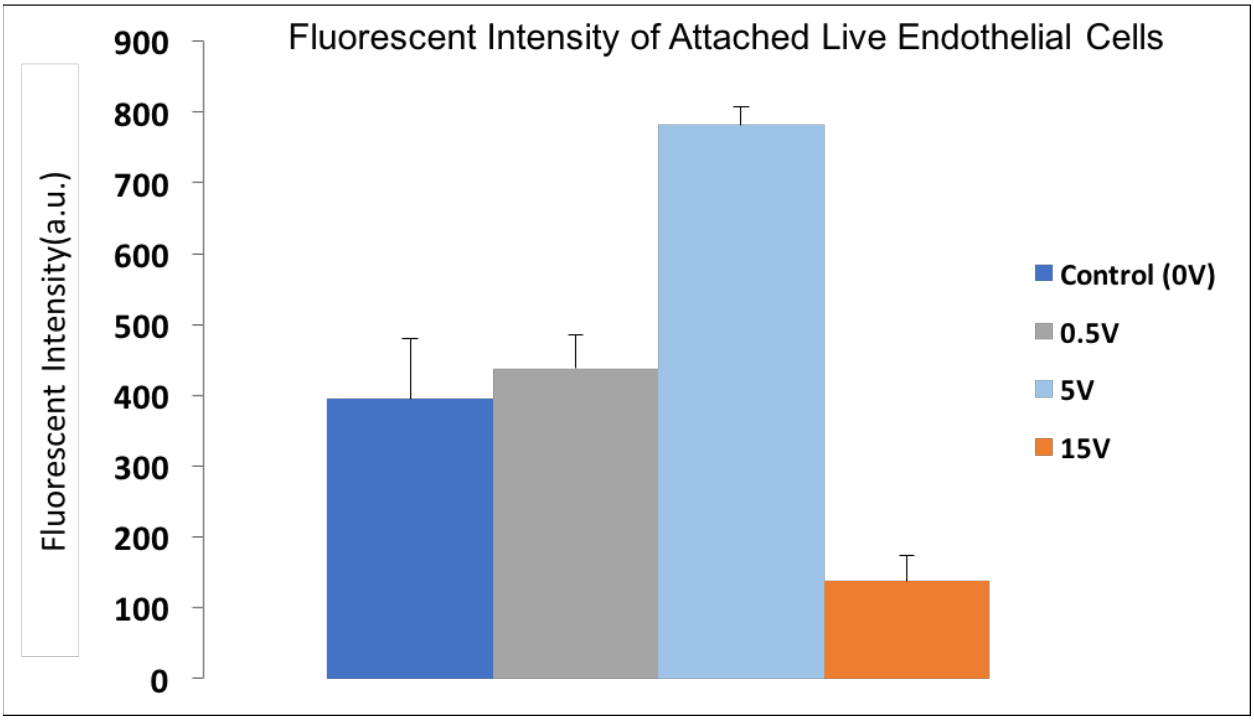

Figure 32: Fluorescent intensity of attached live Calcein AM stained endothelial cells under applying (0V, 0.5V, 5V and 15V conditions)

4.4 DISCUSSION

The cell is the basic structural unit of all living organisms, which contains a watery cytoplasmic solution and surrounded by a cell membrane. One of the important features of biological cells is having electrical nature due to the exchange of electrically charged ions across the cell membrane and showing the electrical potential of its interior relative to the exterior. Cell membranes consist of phospholipid bilayer structure and ion channels (*i.e.*, K and Cl ion channels) and proteins are embedded across this phospholipid bilayer (Figure 33).

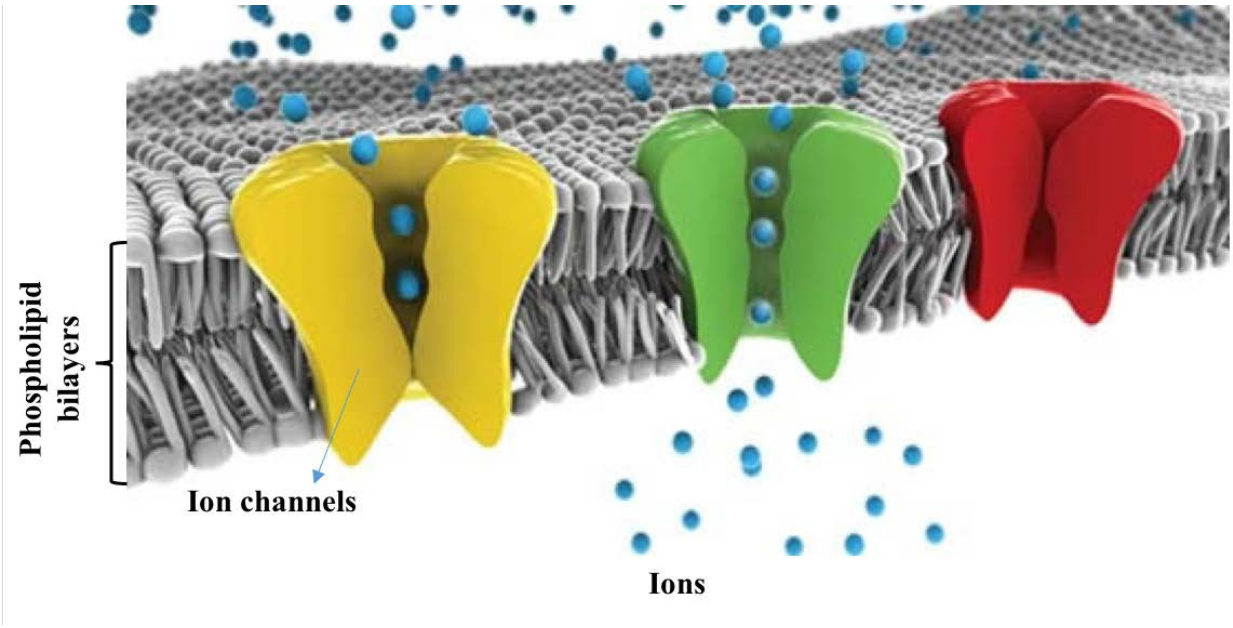

Figure 33: Schematic of cell membrane structure[104]

Phospholipid bilayer in the cell membrane is an insulator layer which acts as the dielectric which separate two electrically conductive regions of the cytoplasm and the extracellular fluid. Therefore, the cell can be modeled by a capacitor as shown in Figure 34.

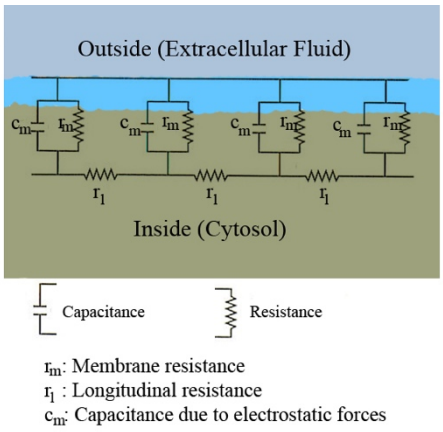

Figure 34: Schematic of the biological cells modeled as a capacitor[105]

Electric fields exist in many biological systems and influence cell signaling and many cellular behaviors and biological events. Therefore, electrophysiological features of cells vary with the surrounding physiological environment. At rest, most cells have typically a potential around -40 to -80mV indicating that they are dominated by K or Cl permeability. In a study by Jongsma *et al.,* the membrane potential of isolated human vascular endothelial cells, capacitance and input resistance were measured -16.3±12.7mV, 53.9±5.5 pF and 2.3±1.3GΩ[106].

Based on the electrophysiological features of cells, the cells can be seen as charged particles and electrostatic cell seeding can be modeled as electrophoretic deposition (EPD). EPD is a process that colloidal charged particles suspended in a solution and they migrate under the influence of an electric field generated between two electrodes, thus, they are deposited onto an electrode based on the electrostatic charge they have (Figure 35). In the electrostatic cell seeding set-up that we used in this study, the thin film nitinol plays as the positive electrode and the endothelial cells that are suspended in the PBS or cell medium solution play as the electrostatic negatively charged particles.

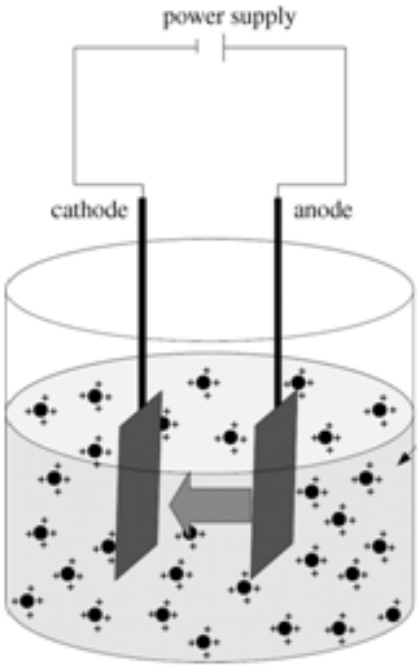

Figure 35: Schematic of electrophoretic deposition[107]

Avgustinik *et al.*, described the factors affecting the amount of deposited particles during EPD process in cylindrical, coaxial electrodes. These factors include the length(l) and radius(a) of the deposition electrode, the radius of the coaxial counter electrode (b > a), the particle mass concentration in the suspension (C), permittivity (ε), the zeta potential (ξ), the viscosity of the suspension (η), the electric field strength (E) and the deposition time (t). Therefore, the deposit yield (w) can be estimated through the following equation[108]:

$$w=\frac{l.E.\varepsilon.\xi.C.t}{3.\ln\left(\frac{a}{b}\right).\eta} \quad (9)$$

In this study, by using Taguchi DOE method, the effect of four factors (*i.e.*, voltage, substrate, cell suspension medium and incubation time) in the parallel electrostatic cell seeding set-up were studied. Since parallel capacitor set-up is a simpler set-up to perform the electrostatic cell seeding experiments compared to cylindrical capacitor intravascular set-up, it was used to study the effects of electrostatic cell seeding parameters (*i.e.,* incubation time, substrate, cell suspension solution and applied voltage) using Taguchi DOE methods. Design of experiment method allows evaluating multiple factors simultaneously and finding the optimal condition for accelerating and improving the endothelial cell seeding on the thin film nitinol substrate.

PBS and cell medium were tested as the cell medium suspension, in addition to the difference of their dielectric constant that is not significant; the main difference between them is the presence of proteins in the cell medium. Our results demonstrated that the average number of attached cells was higher when the cell medium solution was used. Proteins in biological serum effectively play role in the cell adhesion process such that proteins and biomolecules first adsorb on the surface of materials and then cells attach on these pre-adsorbed proteins. Proteins are large biomolecules and contain multiple functional groups with electrostatic charge; therefore, the electrostatic charge of the substrate can affect the type and the arrangement of the deposited proteins and subsequently impact their function, the ligand binding and cell signaling.

The estimation of average effect of voltage showed that increasing voltage up to an optimal range can enhance cell attachment but increasing it beyond this point decreased the number of attached cells. The applied voltage affects both the induced electric field and substrate

electrostatic charge. McCaig *et al.,* showed electric fields in the range of 75–100mV/mm^{-1} with voltage of 1.5–2.0mV enhanced the elongation and migration of endothelial cells[109]. If the applied voltage across the capacitor becomes too large, the dielectric breaks down and results in a short circuit. In addition, high voltage and high electric field can damage the cell membrane. For instance, in this study, in cylindrical capacitor intravascular set-up, under 15V applied voltage, the number of attached cells decreased compared to the control sample (0V applied voltage).

By increasing time incubation, the results demonstrated that the number of attached cells increased which showed that over time the seeded endothelial cells did not detach from the surface and they grow and their number increases.

The average number of attached cells was slightly higher on the STFN substrate compared to the TFN. The grown oxide layer on thin film nitinol acts as an insulating surface layer and enhance the wettability of the surface leading to improve the cell adhesion.

4.5 SUMMARY AND CONCLUSION

High incidence of restenosis in the current small-diameter vascular grafts caused by lack of endothelialization and thrombosis occurrence in them result in a pressing need to develop a novel vascular graft resistant to restenosis. Thin film nitinol shows unique favorable properties such as superelasticity, shape memory, biocompatibility and anti-thrombogenicity in a low profile (~10μm) which make it a candidate for small diameter vascular graft application. In this study,

electrostatic cell seeding was suggested in order to seed endothelial cells on the surface of thin film nitinol to enhance the resistance of the TFN surface against the restenosis. Endothelial cells possess electrostatic negative charge on their surfaces and under uniform electric field can be considered as electrically charged particles in electrophoresis process. Therefore, by inducing positive electrostatic charge on the surface of thin film nitinol, it is postulated to expedite the seeding of endothelial cells with negative charge on the surface. To assess and optimize the parameters in electrostatic cell seeding, a parallel capacitor set-up with TFN substrate as the positive electrode were used and using Taguchi design of experiment, the effects of applied voltage, substrate and cell suspension solution were evaluated. The results demonstrated that the number of attached endothelial cells increases by applying voltage and over time the detachment does not occur. Number of attached cells increase on the superhydrophilic TFN substrate and in medium solution (*i.e.,* with the presence of serum protein) increased compared to TFN substrate and PBS solution, respectively. 1V applied voltage with induced electrostatic charge of 3.18×10^{-6}μC and induced electric field of 500V/m showed the highest endothelial cell attachment in parallel capacitor set-up while the condition of 5V voltage with induced electrostatic charge of 0.68×10^{-6}μC and induced electric field of $5.11 V/mm^{-1}$ (*i.e.,* much lower amount compared to the parallel capacitor set-up) showed the highest endothelial cell attachment in cylindrical set-up intravascular set-up.

Electrostatic endothelial cell seeding for superhydrophilic thin film nitinol deployed in a 6Fr catheter demonstrated efficacy in accelerating endothelial cell attachment. In future studies, the phenotypic features of attached endothelial cells and the *in vivo* studies of implanted electrostatic endothelial cell seeded thin film nitinol will be evaluated.

5.0 TECHNIQUE 3: COATING ELECTROSPUN SILK ON THIN FILM NITINOL

5.1 INTRODUCTION

The high incidence and cost of small vascular diseases creates a pressing need to develop an effective treatment method and qualified replacement for these non-functional vessels [110-112]. Transcatheter endovascular therapy has made a significant progress in treating occlusive vascular diseases via presenting various minimally invasive devices. However, when these devices are used to treat small vascular diseases, *e.g.*, pediatric cardiovascular diseases, there still remains critical risks in terms of the device delivery, restenosis occurrence and hemocompatibility[113, 114]. As an example, coarctation of the aorta (CoA) is a narrowing occurrence in a short segment of aorta, where the main artery distributes the oxygenated blood from the left ventricle to all parts of body (Figure 36). It is a relatively common defect that accounts for 5-8% of all congenital heart defects[115]. If CoA is not diagnosed and treated in a timely manner, it is developed into the congestive heart failure (CHF) or hypertensions which both are among common pediatrics cardiovascular diseases.

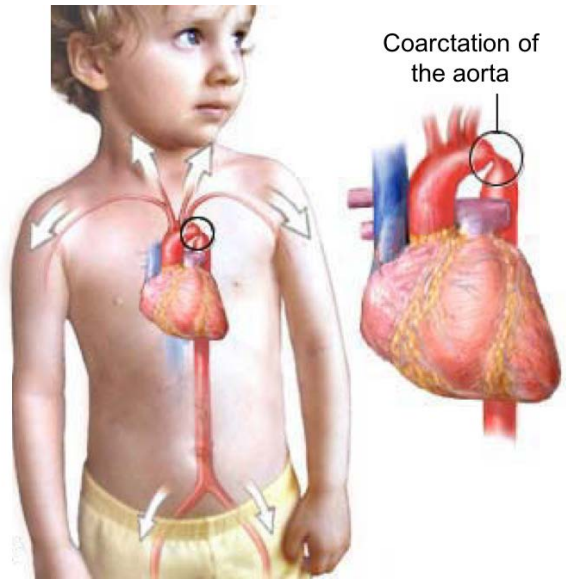

Figure 36: Schematic of coarctation of the aorta (CoA) disease[116]

Open surgery (*i.e.*, eliminating the narrowed section and connecting ends of the arteries along with using medication) is a common method to treat newborns diagnosed with CoA. Alternative treatment options specifically applied for older children are transcatheter-based therapies that include a dilation of the narrowed site using an angioplasty balloon or the placement of a vascular stent in the narrowed site[117-120]. While both surgical and transcatheter-based procedures are widely used for treating CoA, there are a few potential complications such as possible damages to the downstream organs such as kidney because of the blood flow interruption during surgery, CoA recurrence after balloon dilation due to the vessel damages, and restenosis occurrence at the narrowed site especially after stent deployment. In addition, systematic hypertension, aortic valve abnormalities, and aortic aneurysm formation could be other concerns that can occur after the conventional CoA treatments[115, 121, 122]. All

these complications are driving force to seek for a safer and more effective treatment method for CoA treatment. The ideal device for treatment of CoA could be a low-profile endovascular device, which can (1) be safely delivered with a micro delivery catheter (*e.g.*, < 3Fr), (2) be deployed in small blood vessels minimizing damages on the vessel wall, (3) reduce or prevent any potential thrombosis and neointimal hyperplasia with the device thickness of less than ~20μm, and (4) promote rapid endothelialization of the blood-contacting surface.

A high-quality thin film nitinol (TFN) can be fabricated by vacuum sputter deposition technique. Thin film nitinol exhibits superelasticity behavior (*i.e.*, reversible deformation to high strain around 5% at human body temperature) even with the substantially reduced thickness down to a few micrometers. TFN can be collapsed in remarkably smaller size catheters due to its low-profile dimension and easily be delivered through highly tortuous and narrow vascular system. In addition, the superelasticity of TFN enables the device to be deployed by itself without any additional actuation systems such as ballooning. This material has also demonstrated excellent biocompatibility and high corrosion resistance with its ultra-smooth surface as implantable vascular devices over decades, which are beneficial for treating small vascular diseases[69, 123, 124]. While TFN has shown superior superelastic behavior with thromboresistance characteristics, but its surface endothelialization is not so rapid and sufficient in order to be used as a small vascular graft application. Therefore, thin film of silk nano fibers can be used as a novel luminal coating layer for facilitating rapid and confluent endothelial cell growth. Silk is a fibrous protein that is mostly synthesized in epithelial cells that line in the glands of insects such as spiders (*e.g., Nephila clavipes)* and silkworms (*e.g., Bombyx mori).* Silkworm cocoon silk contains two structural proteins, the fibroin heavy and light chains which are glued together with sericin protein in forming the cocoon silk. Silk fibroins are purified from

sericins by boiling silk cocoons in an alkaline solution (*i.e.*, degumming). Silk has been established as a biomaterial for a wide variety of applications, for example, it has been used as sutures for centuries. Silk has beneficial properties such as excellent biocompatibility, biodegradability and sterilizability. Moreover and shows high processability such that silk solutions can be used to form films, gels, sponges and non-woven mats[125]. Figure 37 shows the general processing steps and the final possible forms of silk from silk cocoon source.

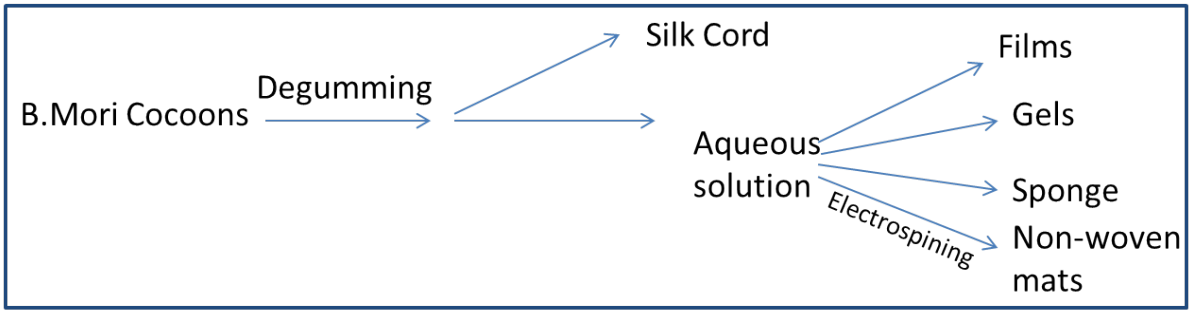

Figure 37: The degummed silk fibers can be processed into silk cords or formed into aqueous silk fibroin solution and it can be processed into non-woven silk fibers, sponges, gels and films

Silk fibroin can be successfully electrospun into nanofiber forms; electrospinning process is a known process to form fibers with nanosclae diameters from various polymers. A typical electrospinning setup consists of three components: a high voltage supplier, a capillary needle, and a collector (Figure 38). During electrospinning, the polymer solution is suspended from a needle and a high voltage is applied to it; therefore, the suspended polymer droplet becomes charged and electrostatic repulsive force counteracts the surface tension and the droplet is stretched; at a critical point a stream of liquid erupts from the surface. This point of eruption is

known as the Taylor cone. As a result, a fiber jet ejects from the apex of the cone and accelerates towards the collector.

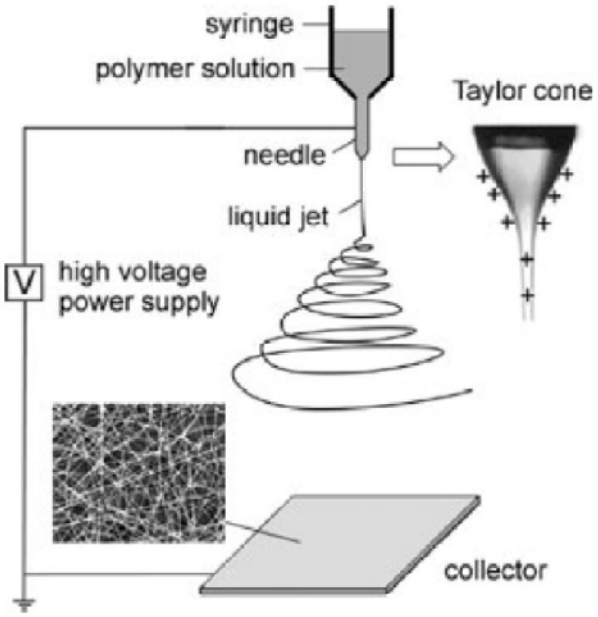

Figure 38: Schematic illustration of electrospinning setup[126]

In electrospinning, multiple factors have been found to control fiber formation in this process such as concentration, viscosity, surface tension, electrostatic conductivity of the polymer solution, applied electrical voltage, distance between tip and collector and the temperature. To generate uniform nanofibers, an optimal combination of these electrospinning parameters should be selected.

Electrospun silk demonstrated an excellent substrate for the cell growth mimicking the function of native extracellular matrix [127]. In native tissue, the extracellular matrix is mainly composed of fibrous proteins, including collagens, elastin, fibronectin, and laminin (Figure 39). The diameter of these structural ECM proteins (50 to 500nm) is about 1–2 orders of magnitude smaller than the cells. Nanofibers to more adequately simulate ECM geometry can be produced by electrospinning.

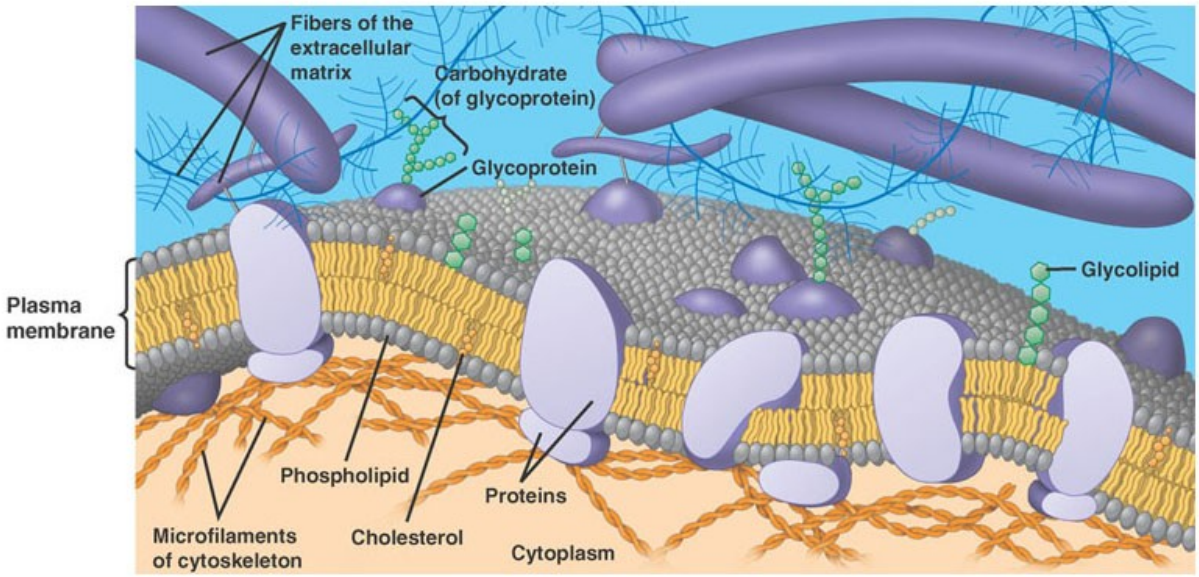

Figure 39: Fibers of extracellular matrix(ECM)[128]

This study aims to fabricate a low-profile composite endograft using thin layers of nitinol and silk. The silk nanofibers have been deposited on the TFN substrates using electrospinning technique and the feasibility of using thin film silk as a novel coating for facilitating rapid and

confluent endothelial cell growth has been explored. Therefore, the functionality, thrombogenicity as well as endothelial cell (EC) and smooth muscle cell (SMC) responses were evaluated.

5.2 METHODS

5.2.1 Preparation and characterization of thin film nitinol

The thin film nitinol (TFN) was prepared by a direct current (DC) sputter deposition technique as previously described[129]. Briefly, 6μm thick films were deposited on 4" silicon wafer as the substrate having 5000Å thick silicon oxide layer. The sputter chamber pressure and the argon pressure were 5×10^{-8} and 1.5×10^{-3}Torr, respectively. In order to prepare TFN specimen with dimensions of 1cm×0.6cm for fabricating TFN-S endograft, a chemical etching process along with a conventional photolithography method was used to create patterns on the sputtered TFN (Figure 40A). AZ-4620 positive photoresist with around 5μm thickness was used to define patterns and completely protect the TFN layer before the chemical etching. The etchant solution with a mixture of hydrofluoric acid (HF), nitric acid (HNO_3) and DI water with volume ratios of 1:1:20 was used and the chemical etching process approximately lasted 6min to etch through the TFN with 6μm thickness[130]. The resultant etched film was crystallized at 500°C for 120min in a vacuum less than 10^{-7}Torr and mechanically removed from the silicone substrate. The phase transformation behavior and crystallinity of TFN material was studied using differential scanning calorimeter (DSC) and X-ray diffractometer (XRD), respectively.

5.2.2 Preparation of electrospun silk

Bombyx mori cocoon (provided from Uljin-Nongwon, Republic of Korea) was degummed to remove sericin and other impurities. It was boiled at 95°C with sodium carbonate (0.2% w/w), (Daejung Chemical & Metals Co, Republic of Korea, 7541-4405) and sodium oleate (0.3% w/w), (Kanto Chemical Co, Japan, 37225-01) for 2hrs, and then it was rinsed thoroughly with deionized (DI) water to remove the impurities. Then, it was dissolved in 9.3 M LiBr (Samchun Chemical, Republic of Korea, L1106) solution. This solution was dialyzed against DI water for 3 days to eliminate LiBr using dialysis tubing cellulose membrane (Sigma-Aldrich, US, D9402-100FT). After dialyzing, the solution was freeze-dried (Eyela, Japan, FDU 2100) and then dissolved in 98% formic acid (JUNSEI Chemical Co, Japan, 25010-0350) at 10% (w/v) concentration for electrospinning.

5.2.3 Fabrication of integrated TFN/silk endograft

Using a direct electrospining of thin silk layer onto the TFN, 6μm-thick sputter-deposited superelastic TFN and 10μm thick electrospun samples were integrated. Figure 40B shows process details on the direct electrospinning of silk onto the TFN. An electrospining set-up was comprised of high voltage power supply, syringe pump, metal nozzle and a metal drum collector (NanoNC, Republic of Korea, ESR200RD). A SF/formic acid solution in 12mL syringe was continuously fed to the tip of the charged metal nozzle. The TFN was cut into a small piece and attached on the surface of the drum. An electric field was applied between the nozzle tip and the

drum collector. The applied voltage was fixed at 20kV and the distance of 15cm was maintained while the pumping flow rate was maintained at 1mL/hr.

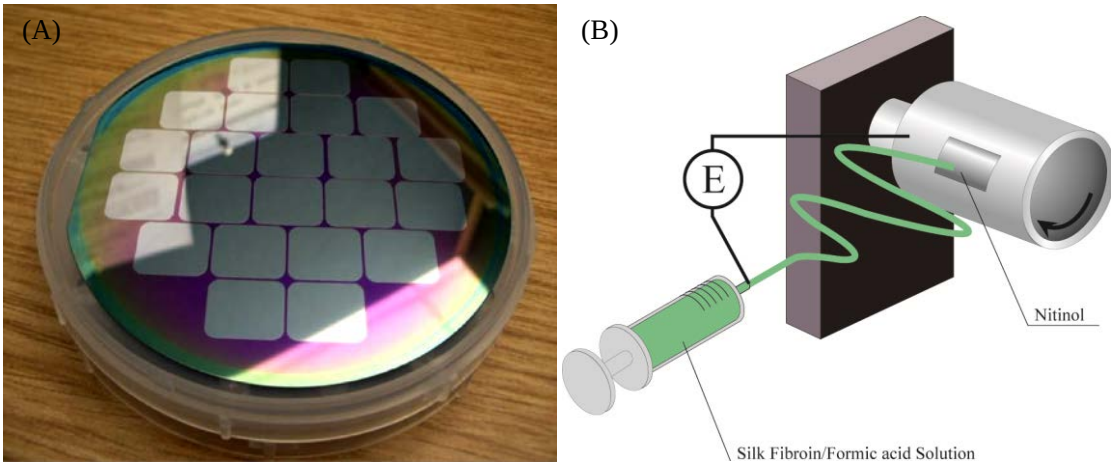

Figure 40: (A) Patterned TFN for the endograft fabrication and (B) Schematic diagram of electrospining of silk fibroin (SF) on the surface TFN

The morphology of the electrospun silk deposited on TFN was analyzed by scanning electron microscopy (SEM, JEOL JSM-6610LV, Japan).

After sputter deposition and subsequent thermal annealing process, the stand alone TFN was achieved by splitting silicon substrate followed by mechanical delamination process.

5.2.4 Radial force measurement

The radial force exerted from TFN-S endograft was measured with a custom-built test set-up on a vibration isolation table. A brass tube with 2mm internal diameter was used to simulate the

small-caliber vascular geometry. It was cut in half along its longitudinal axis and placed over a force measurement system that was equipped with an accurate load cell (FSB200, FUTEK, Advanced Sensor Technology, Inc., CA, USA). The TFN-S device (15mm long with 3.14mm diameter) was deployed into the half-cut brass tube to measure the device's radial force (F_{radial}). The device was tested five times to evaluate its radial force accurately.

The radial force exerted from the TFN-S device was also estimated by calculating the bending moment produced by the integrated TFN-S device. The radial force was estimated using the approximation presented by Chun *et al*. [131]:

$$F_{radial} = \left(\frac{E}{1-\nu 2}.\ \frac{1}{24}.\ h^3\right).\frac{1}{r}.\ \frac{w}{l} \qquad (10)$$

where *r* is the tube radius (1mm), *l* is the axial length of the rolled film (15mm), *w* is the film width (3.14mm), *E* is Young's modulus of the austenite phase of nitinol (83GPa), *v* is Poisson's ratio (0.33), and *h* is the film thickness (6μm).

5.2.5 *In vitro* cell culture and cell adhesion study

Specimen of e-PTFE, Dacron® and integrated TFN-S were prepared in 1cm×0.6cm dimensions. All the samples were sterilized by immersion in 70% ethanol for 30min, then, they were transferred to a 12-well tissue culture plates (Becton Dickinson and company, NJ, USA) and washed with sterile PBS (Gibco®, NY, USA). BAEC (Bovine Aortic Endothelial Cells; Lonza,

NJ, USA) at passage number 7 were seeded at a density of 4×10^5 cells/cm^2 on the samples. Cells were grown in the medium consisting of Endothelial Cell Basal Medium (EBM)-2 (Lonza, NJ, USA) and EGM-2 SingleQuot Kit Suppl. & Growth Factors including (Hydrocortisone 0.02%, FBS2%, VEGF0.05%, hFGF-B2%, IGF-1 0.05% and HEGF 0.05%, GA-1000 0.05%) (Lonza, NJ, USA). BASMC Cells (Bovine Aortic Smooth Muscle Cells; Lonza, NJ, USA) at passage number 5 were grown in MCDB131 (1×) medium (Cellgro®, VA, USA) including L-glutamine (1%), 10% FBS, Antibiotic-Antimycotic solution (1%) and 50 mg/ml ascorbic acid-2-phosphate. In each well of tissue culture plate, 2mL of media was added at the beginning of the experiment. The plates were placed in a humidified incubator at 37°C and 5% CO_2 for 48 hrs. The samples were rinsed thoroughly with PBS and stained with Calcein AM (life technologies™, NY, USA) and the fluorescence intensities were measured by fluorescent microscopy (Olympus BX43, PA, USA) as an index of live cells. Both morphology and proliferation of adhered cells were evaluated using SEM after sputtering a thin layer of palladium (Pd). For SEM imaging, cells were fixed with 2.5% glutaraldehyde **(**Sigma-Aldrich**,** MO, USA), dehydrated in a series of ethanol/DI water mixtures including 30%, 50%, 75%, 90% and 100% ratios, then, subjected to drying with hexamethyldisilazane (HMDS) (Alfa Aesar, MA, USA)/ethanol in 3:1, 1:1 and 1:3 volume ratios. The samples were then dried in the chemical hood overnight at room temperature.

5.2.6 Dynamic whole blood test

The TFN-S endograft was rolled, collapsed in a 5Fr catheter (The INFINITI, Cordis, CA) and deployed in a silicone tube with 1.5mm internal diameter (Platinum-Cured Silicone Tubing, Cole-Parmer, IL). The silicone tube was connected to the pulsatile pump (Harvard apparatus,

MA) and all circulatory environments were treated with heparin before the application of blood. 100mL of fresh whole human blood was circulating in the tube for 30min while the flow velocity was 0.3m/s and the tube containing the device was placed in the water bath at 37°C temperature (Figure 41). The samples were dried at air and coated with a thin layer of palladium (Pd) for SEM imaging. The SEM images were used to check the clot formation on the samples.

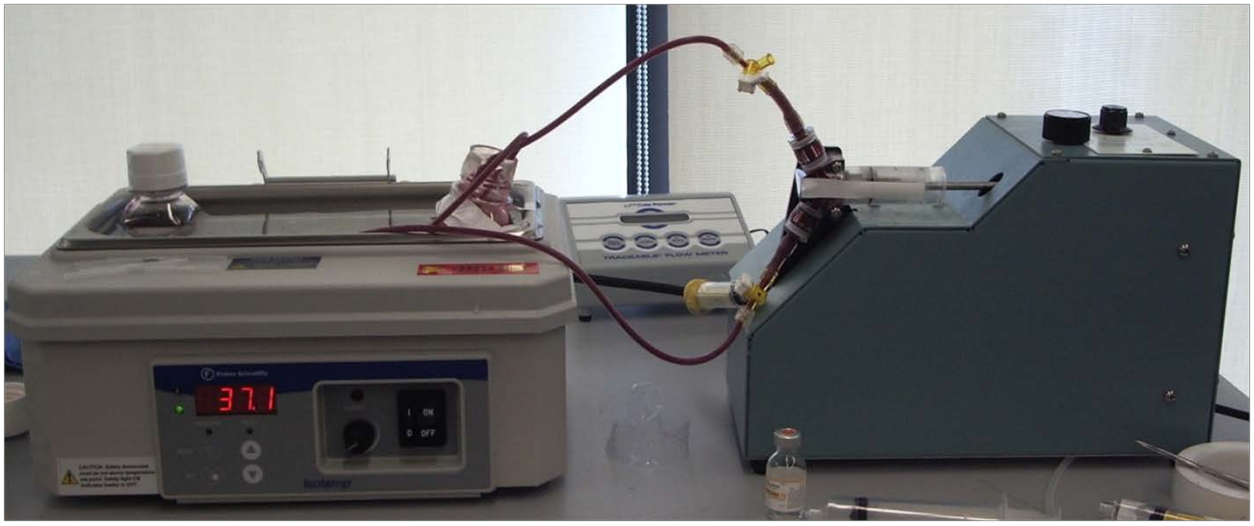

Figure 41: Dynamic whole blood test set-up equipped with a pulsatile flow pump, water bath, and the heparinized silicone tubing

5.2.7 Statistical analysis

Values of fluorescent intensity regarding to attached endothelial and smooth muscle cells were expressed as the mean value ± standard deviation (SD). Statistical analysis was performed for the experiment using one-way analysis of variance (ANOVA) test and Tukey's HSD test by

Minitab® 16.1.0 (©2010 Minitab Inc. PA, USA) and P-value<0.01 was considered statistically significant.

5.3 RESULTS

5.3.1 Material properties of TFN

The XRD result of TFN measured at room temperature showed a predominant single peak at 2θ = 42.5° corresponding to (1 0 0) peak of the B2 austenite phase. It indicates the structure of annealed thin film is crystallized with the austenite phase structure at room temperature. DSC thermogram of TFN shown during cooling and heating operations demonstrated that two peaks are detected, one is observed during heating from -20°C to 80°C which is assigned to the transformation from martensitic phase to the austenitic phase. Austenite start temperature (A_s) equals to 10.09°C and the austenite finish temperature (A_f) is 23.66°C. One other peak is appeared during cooling the specimen corresponding to the transformation from austenitic phase to the martensitic phase (*i.e.*, martensite start temperature (M_s) = 20.06°C and martensite finish temperature (M_f) = 4.66°C).

5.3.2 Prototype fabrication

After sputter deposition and subsequent thermal annealing process, the stand alone TFN was achieved by splitting silicon substrate followed by mechanical delamination process. Figure 42A shows the SEM image of the cross section in TFN-S prototype created by a direct deposition of

silk onto TFN using electrospinning technique. Electrospun silk can be attached without any delamination. The SEM image in Figure 42B shows well-distributed electrospun silk layer with the thickness of fibers ranging approximately from 0.36 to 0.67μm (*i.e.,* 3D scaffold for rapid endothelialization). Figure 42C shows the cylindrical shape of TFN that was manufactured using stress induced permanent deformation process. Once the electrodeposited silk layer has been coated on TFN, the whole device was collapsed into a 3Fr micro delivery catheter as shown in Figure 42D. No noticeable film damages or mechanical deformation were observed during both collapsing and deployment.

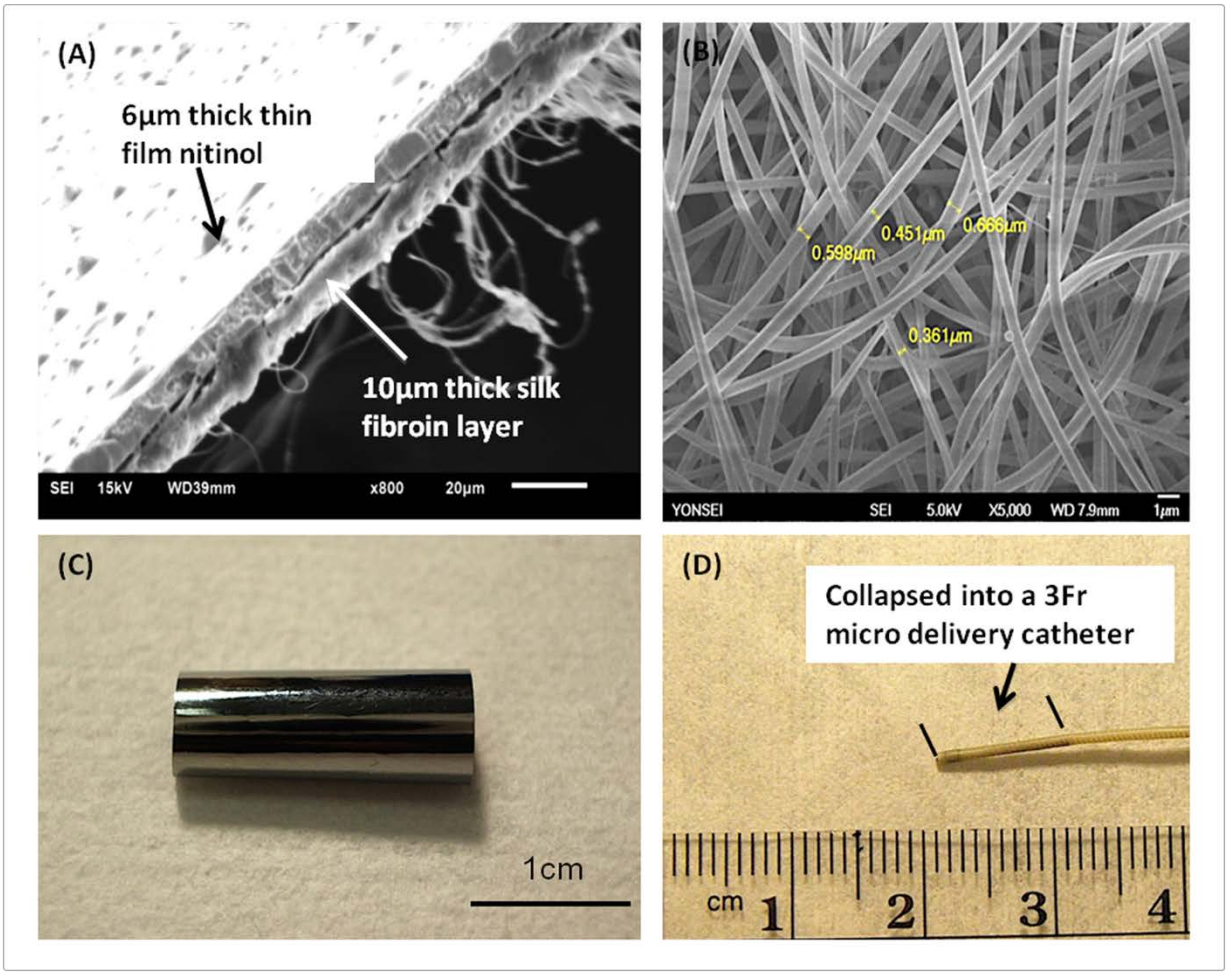

Figure 42: Device prototype images; A) SEM micrograph of integrated TFN/electrospun silk, B) The magnified structure of the electrospun silk, C) Integrated TFN/silk prototype, D) The collapsed integrated TFN/silk device into a 3Fr micro delivery catheter

5.3.3 Radial force evaluation

The theoretical prediction of the radial force of the TFN-S endograft (4µN) agrees well with the experimental data (3.8µN). This assessment result implies that there will be no migration of the

device under the typical blood flow conditions observed in a small vasculature[131]. Results of radial force measurement demonstrated that there was no significant difference between radial forces of thin film nitinol and the TFN-S within the range of the load cell (*i.e.*, ± 0.0001N); adding the thin layer of electrospun silk did not increase the radial force. The TFN-S device demonstrated no migration under the flow velocity of 0.3m/s in 2mm diameter tube (n=3).

5.3.4 Cell adhesion and viability studies

5.3.4.1 SEM image analysis

Figure 43A, 43B and 38C qualitatively compare both the number and morphology of the endothelial cells (ECs) attached on Dacron®, e-PTFE and TFN-S samples after 48hrs, respectively. Figure 43 shows each of these substrates presents a different topography for cells, the e-PTFE is formed from nodes around 10µm width connected with fibrils while Dacron® is composed of ~ 20µm woven fibers and electrospun silk represents a porous 3D mesh composed of slender fibers spread in random directions. ECs attached on both Dacron® and e-PTFE samples were mostly observed in spherical shape and fixed on the surface by short and thin cytoplasmic digitations or filopodia. However, attached cells on the electrospun silk surface had spread out in fusiform morphologies showing major podia around the cells. Figure 43D, 43E, and 38F show how smooth muscle cells (SMCs) attached on Dacron®, e-PTFE and TFN-S samples after 48hrs, respectively. SMCs were well spread out on all three surfaces and manifested their cytoplasmic extensions in multiple directions.

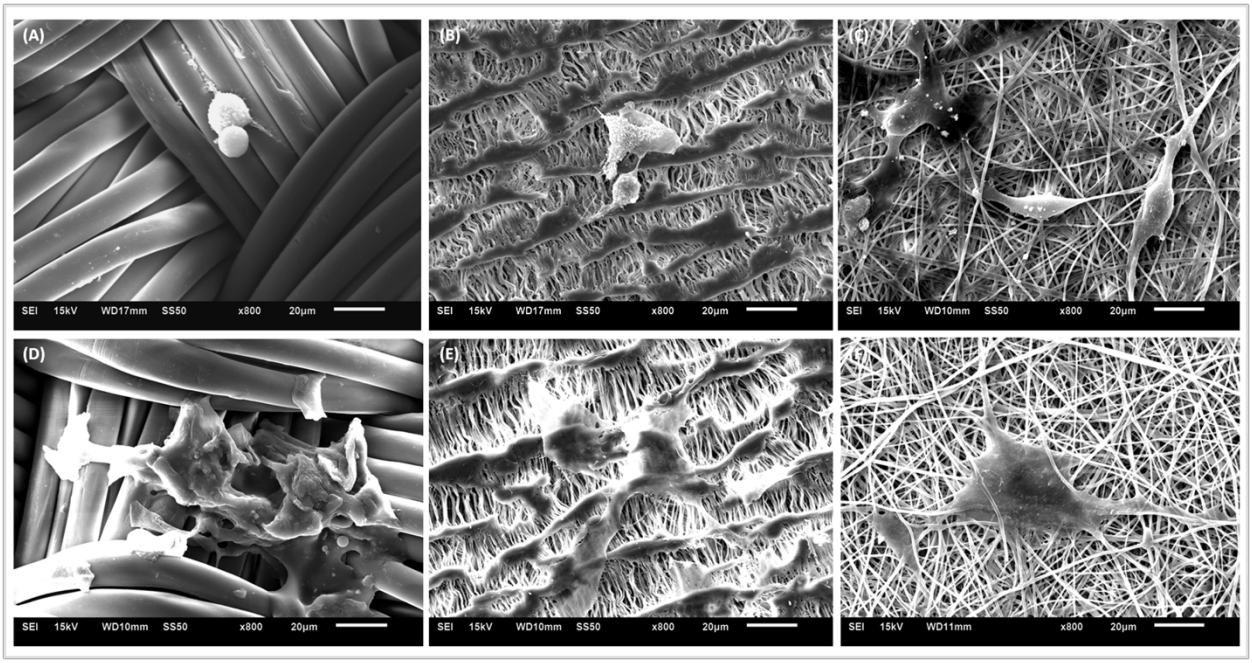

Figure 43: SEM images of the attached endothelial cells (ECs) on A) Dacron®, B) e-PTFE and C) TFN-S and the attached smooth muscle cells (SMCs) on D) Dacron®, E) e-PTFE and F) TFN-S

5.3.4.2 Fluorescent microscopy image analysis

Figure 44 shows representative fluorescent microscopy images of Calcein AM stained endothelial cells (44A-C) and smooth muscle cells (44D-F) on Dacron®, e-PTFE and silk surfaces, respectively. The number of viable endothelial cells significantly increased on silk surfaces (Figure 44C) compared to Dacron® (Figure 44A) and e-PTFE (Figure 44B). Similarly, the number of smooth muscle cells was higher on electrospun silk (Figure 44D-F).

Figure 45 shows average fluorescent intensity of live Calcein AM stained ECs and SMCs attached on three different materials. TFN-S demonstrated greatly increased levels of fluorescence intensities as compared to either e-PTFE or Dacron® samples. As shown in Figure

44A and B, the TFN-S material showed significantly higher fluorescent intensities for both ECs and SMCs compared with either e-PTFE or Dacron® samples (P-value<0.001). Average fluorescent intensity for TFN-S was 1342±1025 a.u/mm^2 for ECs and 1252.74±990 for SMCs, which are more than twice of the total intensities observed in either e-PTFE or Dacron®.

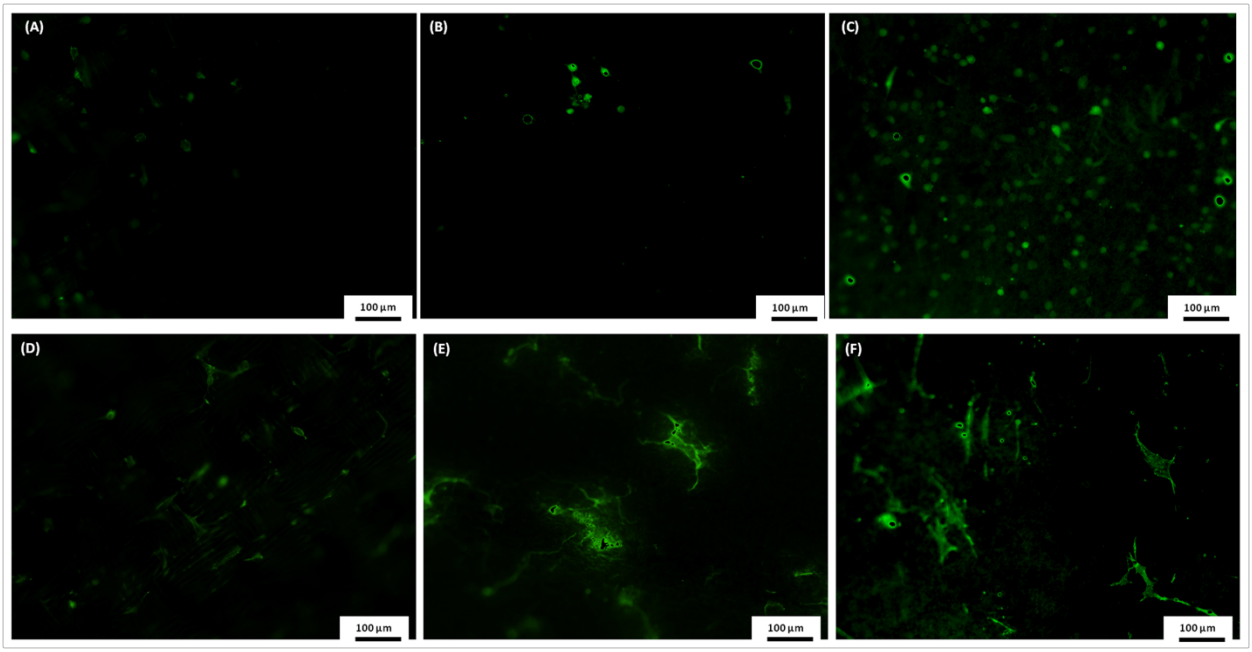

Figure 44: SEM images of the attached endothelial cells (ECs) on A) Dacron®, B) e-PTFE and C) TFN-S and the attached smooth muscle cells (SMCs) on D) Dacron®, E) e-PTFE and F) TFN-S

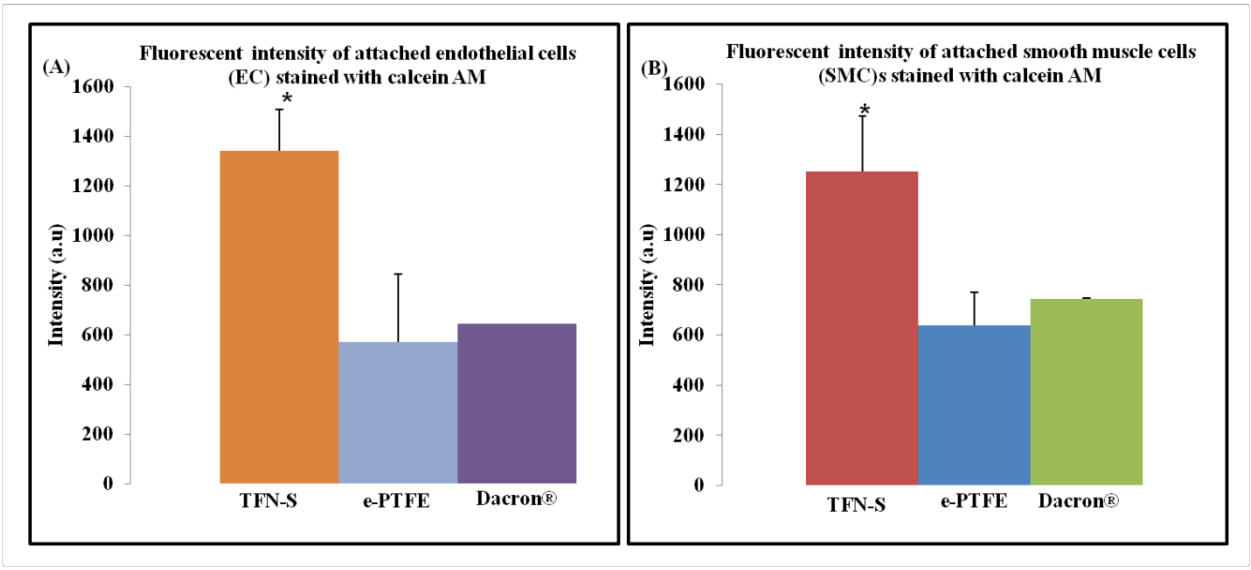

Figure 45: Average fluorescence intensity measurement of Calcein AM stained A) endothelial cells (ECs) and B) smooth muscle cells (SMCs) attached on TFN-S, e-PTFE, and Dacron® samples

5.3.5.6 Dynamic whole blood test

Figure 46 shows the representative SEM images of Dacron®, e-PTFE and TFN-S surfaces after 30min under dynamic whole blood flow, shown in different magnifications. Qualitative analysis of scanning electron microscopy data demonstrated substantially reduced thrombosis on TFN-S as compared to either Dacron® or e-PTFE. SEM images for Dacron® (Figure 46A, D, and G) and e-PTFE (Figure 46B, E, and H) showed that almost fully covered blood clots on the surface and the deposited blood products were dense. The thicknesses of the deposited blood clots roughly range from a few micrometers to a few hundred micrometers. These deposited layers were composed of both fibrin and platelet micro-particle (PMP) formation (*i.e.*, highly activated platelets aggregation)[132] with occasional red and white blood cells visible as well. Although

blood clot was also observed on the TFN-S surface, the total deposition was substantially lower than either e-PTFE or Dacron®.

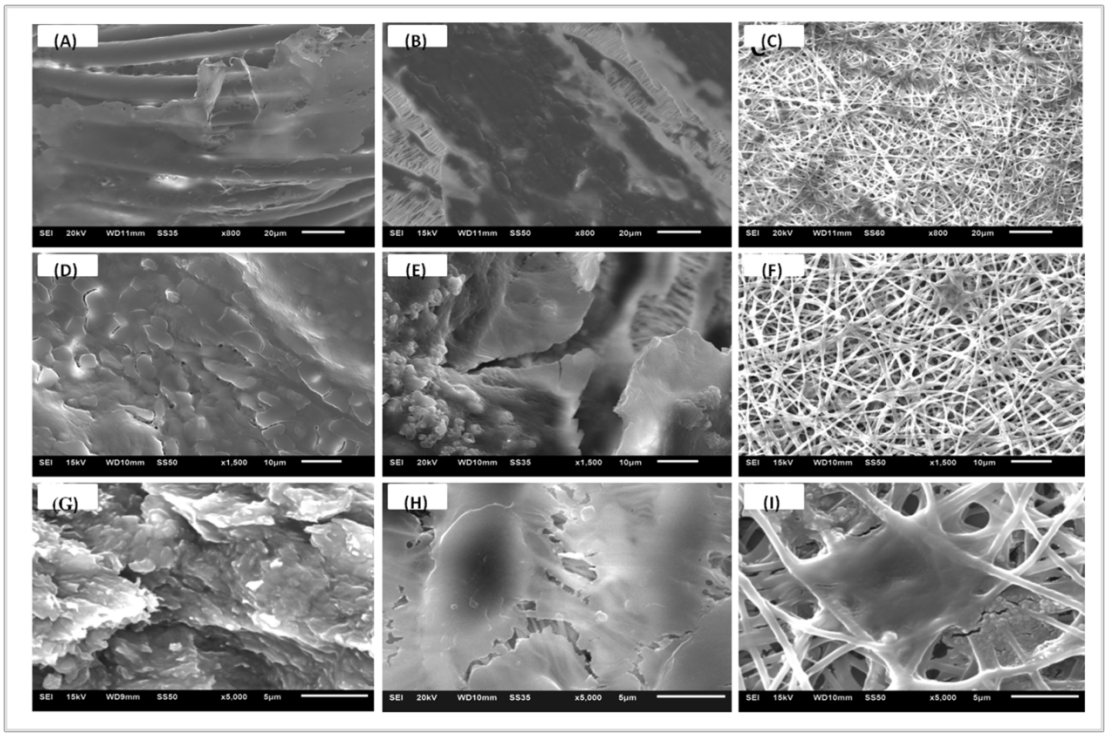

Figure 46: Representative SEM images of hemocompatibility results after 30 min whole blood circulation, three different magnifications (×800, ×1500 and ×5000): Dacron® (A, D, G), e-PTFE (B, E, H) and TFN-S (C, F, I)

5.4 DISCUSSION

A novel low-profile endovascular graft is fabricated and tested that contains thin film nitinol and thin electrospun silk layer, specifically targeted for treating small vascular diseases. *In vitro* cell

culture was performed to evaluate cellular behavior of both endothelial and smooth muscle cells, as well as built up an *in vitro* circulation model using a pulsatile pump, silicone tubing, and whole blood in order to compare a short-term (early) thrombotic response of various endograft materials including TFN and silk (TFN-S). A short-term *in vivo* swine test was also performed to assess biological interaction between thin film nitinol and vascular wall.

The patency rate of commercially available synthetic vascular stent grafts (*e.g.,* e-PTFE and Dacron covered devices) was significantly reduced in small vascular applications less than 6 mm in diameter. While these synthetic vascular stent grafts have demonstrated successful outcomes for treating large-diameter blood vessels, they show undesirable results if used in diseased small-diameter blood vessels. However, the majority of vascular diseases occur in small-diameter blood vessels; therefore, suitable vascular stent graft specifically for small-diameter blood vessels is urgently needed. The primary reasons behind this failure are mostly associated with the surface interaction with blood and blood vessel wall, which includes thrombogenicity and insufficient (or late) endothelialization, as well as the occurrence of excessive neointimal hyperplasia resulting in stent restenosis[133, 134]. Although the exact reasons of both thrombosis and intimal hyperplasia with a small-diameter vascular stent graft are poorly understood, recent studies reveal that a rapid endothelialization of the graft surface minimizing its thrombogenicity have been considered as a successful strategy to enhance the patency rate of vascular grafts[135, 136]. Therefore, most important criteria for the success of a vascular stent graft specifically used in small-diameter blood vessels include: (1) the capability of the rapid endothelialization, (2) slow or minimized smooth muscle cell growth (*i.e.,* reduced neointimal layer formation), and (3) anti-thrombogenicity of the device's surface exposed to the

blood stream. Our new device could synergistically enhance both mechanical and biological functions of the endograft by integrating thin layers of nitinol and silk.

The size of endograft was markedly reduced only using two thin layers of nitinol and electrospun silk without any additional backbone structure (*e.g.,* stent or reinforcement). This unique feature is specifically important for small vessel endograft applications, because the backbones typically increase the bulkiness of the device. The increased dimension of endovascular device in small blood vessels is known to cause local blood flow disturbances, which may increase the probability of potential thrombosis or blood vessel occlusion. All hemodynamic parameters (*e.g.,* flow velocity, wall shear stress, and flow patterns) involve in modulating expressions of endothelial cell genes and proteins which determine the formation of the intimal hyperplasia[137]. Since the thickness of endografts specifically used in small-diameter blood vessels can noticeably change hemodynamic parameters, low-profile endografts are favorable in the aspect of keeping the blood flow and forces similar to that in the native blood vessels. The total thickness of the TFN-S is only 16μm, which is roughly 6.25-12.5 times thinner than either e-PTFE or Dacron® graft materials (*i.e.,* typically 100-200μm thick). In addition, the TFN-S device does not require a backbone that is typically 80-150μm thick.

While the reduced dimension of the device is favorable, it is not always free from the device migration because the radial forces are reduced with the lack of backbone structure. Although a backbone structure helps prevent endograft migration, both empirical and experimental radial force data showed that the TFN-S endograft has sufficient radial force without any backbone or additional reinforcement to overcome the device migration caused by typical blood flow shear stress in small vasculature [138]. This is possible due to thin film nitinol

unique superelastic property even in low dimensions. In addition, the low-profile attribute of the TFN-S device could significantly reduce the size of the delivery catheter (*i.e.,* ID=0.67mm), which is critical for treating small vascular diseases. Therefore, the TFN-S endograft could be delivered via a 3Fr catheter and deployed in the vascular system up to 3mm in diameter.

In addition to the advantageous physical characteristics of TFN-S, the electrospun silk covered the luminal surface of the endograft showed better anti-thrombogenic behavior compared to both Dacron® and e-PTFE. Furthermore, *in vitro* cell culture studies on the TFN-S endograft materials demonstrated that both the number of attached endothelial cells and their spread morphologies on the electrospun silk were superior to both Dacron® and e-PTFE.

The number of viable SMCs attached on its surface also showed higher numbers on TFN-S than those on either e-PTFE or Dacron®. A pristine surface was acquired without damages on the vessel wall after the TFN-S device deployment *in vivo*. This result showed that there would be no (or minimized) stent-induced injury and wound healing process. Even though the gravitationally seeded SMCs have more cells attached on the surface, there would be no triggers of the wound healing process. While the SMC affinity is one of the important factors to be considered as SMC growth and further neointima growth, there are more complex mechanisms in neointima growth and restenosis. For example, there are several complex mechanisms from the migrated and proliferated cells from the wall, originated SMCs from the adventitial fibroblasts, bone marrow or circulating cells. The neointima growth by SMCs is controversial and more research is needed to define the detail mechanisms of SMC attachment on the graft materials[139, 140]. Our *in vitro* cell culture study results provide the proof-of-concept data about the reaction of electrospun silk compared to e-PTFE and Dacron® samples to the ECs and

SMCs which are the two main biological cells involving in restenosis formation[141, 142]; however, to discern the restenosis progress in these grafts, more *in vivo* data will be needed.

5.5 SUMMARY AND CONCLUSION

A novel composite endograft was manufactured via integrating thin layers of nitinol and electrospun silk (TFN-S) aiming small-diameter vascular graft applications.

TFN-S demonstrated a remarkably low-profile endograft (*i.e.,* ~16μm) with radial force of 3.8μN resulted from thin film nitinol superelasticity. This radial force suffices to prevent migration under blood flow of small-diameter blood vessels without need to use vascular stent backbones. *In vitro* experiments showed electrospun silk (*i.e.,* luminal surface covering) significantly decreased thrombus and improved endothelialization compared to two conventional vascular grafts (*i.e.,* Dacron® and e-PTFE). The proof-of-concept *in vitro* testing results suggest that TFN-S could be promising candidate materials for small-diameter vascular grafts.

6.0 TECHNIQUE 4: MICROPATTERNED THIN FILM NITINOL COVERED CAROTID ARTERY EMBOLIC PROTECTION STENT

6.1 INTRODUCTION

Carotid artery disease is a major cause of stroke in the United States. Atherosclerosis occurrence and stenosis in the carotid artery inhibit proper blood flow to the brain leading to a serious brain damage, in addition, the risk of dislodgment and embolization from the atherosclerosis plaque and the occlusion of cerebral micro vessels exist and can lead to an ischemic stroke (Figure 47). Stroke is the leading cause of mortality and morbidity in the United States such that approximately 795,000 people suffer from a stroke annually and 15%-20% of these strokes is associated to carotid artery stenosis[143, 144]

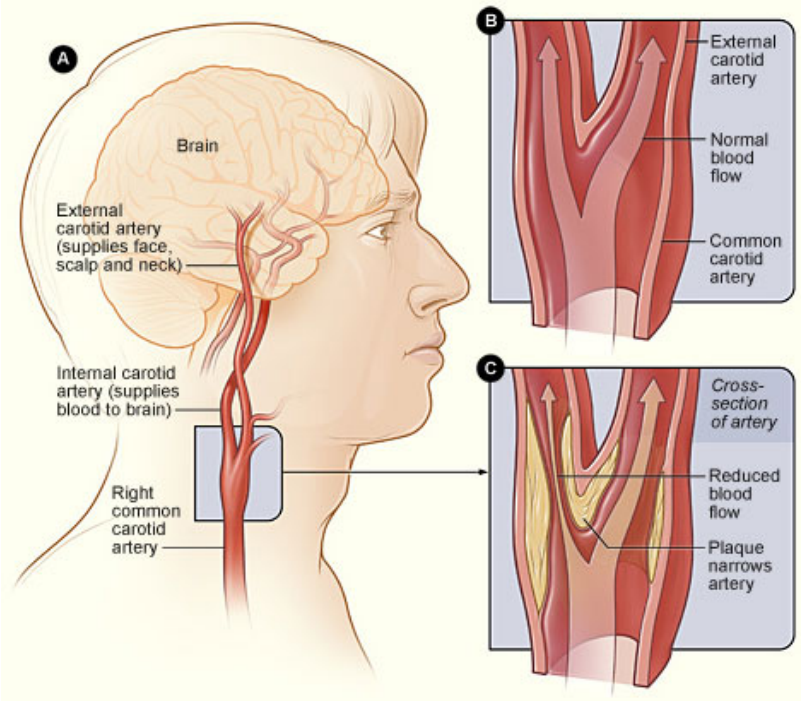

Figure 47: A) carotid artery, B) normal carotid artery and C) Carotid artery stenosis[145]

Carotid endarterectomy (CEA) is the standard treatment for carotid artery stenosis and around 100’000 CEA procedures are performed annually in the US alone[146]. The CEA procedure begins with a longitudinal arteriotomy of carotid artery and removing the plaque and finally closing the cut (Figure 48). However, after the surgery, there is the risk of re-narrowing of artery either immediately or over time and also there is the risk of embolization and thrombosis occurrence during the procedure.

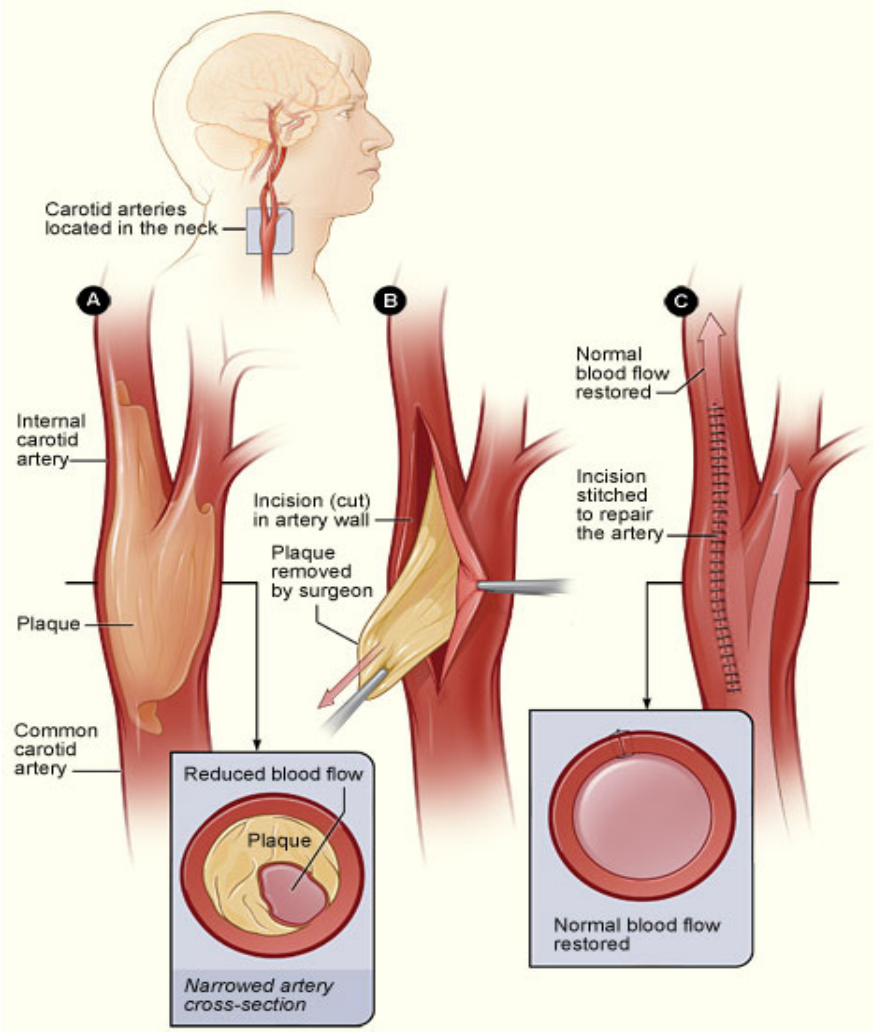

Figure 48: The process of carotid endarterectomy[147]

Carotid angioplasty and stenting is an alternative to the open surgery particularly for patients at high risk for the open surgery. It includes a dilation of the narrowed site using an angioplasty balloon or the placement of a vascular stent in the narrowed site. Vascular stent restores the blood flow through the blocked or narrow arteries but although these treatments have had relative success, they suffer from several drawbacks such as the cost, the risk of recurrence and the possibility of intimal vessel wall damage. In-stent restenosis is typically seen 3 to 6

months after the stent implantation and results in the failure of the procedure. During in-stent restenosis, the thickening of scar tissue underneath the lining of the artery and the migration of smooth muscle cells lead to the blockage of the blood flow.

In addition, the risk of distal embolization of atheromatous material still remains and this risk increases upon stent implantation and balloon dilation. Therefore, various types of embolic protection devices (EPDs) have been designed to use in order to reduce the risk of stroke in the carotid artery stenting procedure. Figure 49 shows multiple examples of embolic protection devices for capturing and removing the debris of atheromatous material. However, no randomized studies prove the effectiveness of the EPDs, for example, the efficacy of GaurdWire distal protection device (Figure 49) in a trial of randomized 500 patients showed no improvement[148].

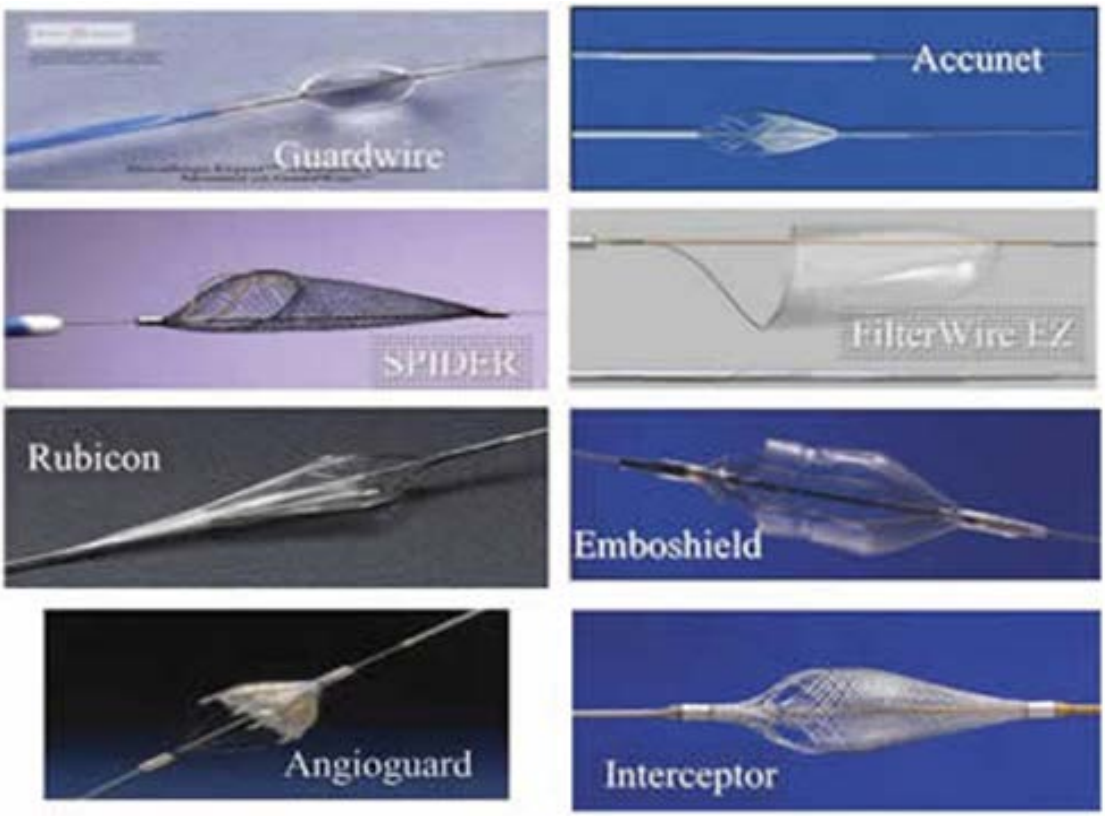

Figure 49**:** Examples of filter-type embolic protection devices (EPDs)[149]

While the FDA has approved several bare metallic, self-expanding stents to treat carotid stenosis, it has not approved any covered stents for carotid artery applications. The pore size in conventional stents is larger compared to the size of embolic material, thus, the presence of a cover can trap the embolic material at source and reduce their propagation. A porous cover does not block the side branches and keeps the normal perfusion into branch vessels. A CE-marked covered stent is the CGuard™ system that consists of metallic stent covered with an ultra-thin polyethylene terephthalate (PET) mesh. A 30 days clinical trial in patients undergoing carotid artery stenting with CGaurd™ system demonstrated the safety and efficacy of this device [150].

In this study, micropatterned thin film nitinol is proposed to be used as the covering membrane in stent for treating carotid artery stenosis. Thin film nitinol shows low profile, superelasticity and controllable micropatterned surface. *In vitro* studies are performed to evaluate the feasibility of micropatterned TFN as carotid artery covered stent in terms of capturing the embolic particles and interacting with endothelial cells.

6.2 METHODS

6.2.1 Preparation and characterization of micropatterned thin films of nitinol

To create micropatterned thin film nitinol, the sputter deposition technique along with a lift-off process introduced by Chun *et al.*, has been used[130]. Briefly, positive photoresist (PR) AZ 5214 was deposited on a silicon wafer via spin coating technique and by using a chromium mask and UV exposure; six different patterns (*e.g.*, diamond shape) were developed on it (Figure 50-1). Then, a reactive ion etching was used to create trenches around the photoresist (50μm depth) (Figure 50-2). Next, photoresist was removed (Figure 50-3) and two layers of copper and SiO_2 were subsequently deposited on the surface (Figure 50-4). The thin film of nitinol was deposited on the top of silicone layer using hot-target sputter deposition technique with the thickness of 6μm (Figure 50-5). The copper sacrificial layer was removed and the deposited thin film of nitinol was subsequently removed from the top of the silicon layer (Figure 50-6). Finally, the film was crystallized at 500°C for 120min in a vacuum of less than 1×10^{-7}Torr. The resultant thin film nitinol showed an austenite finish temperature (A_f) of almost 34°C. Scanning electron

microscopy (SEM) (Jeol-JSM 6610 LV, Japan) was used to observe the morphology of the micropatterned thin film nitinol. Besides, porosity percentage of each sample were calculated using SEM images and MATLAB R2015a (MathWorks, MA, USA) image analysis.

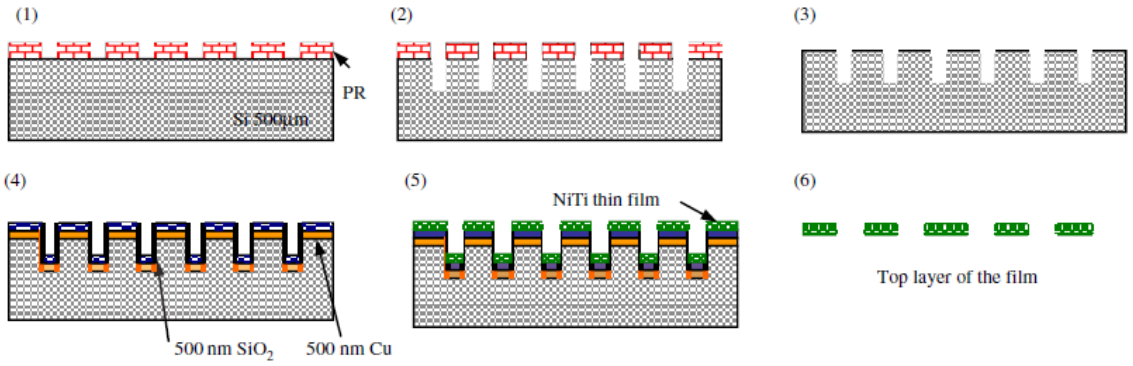

Figure 50: Micropatterned thin film nitinol fabrication process : 1) Positive photoresist (PR) deposition and photolithography to create patterns, 2) Reactive ion etching to create trenches around the photoresist, 3) PR is removed, 4) deposition of copper layer and silicon layer, 5) Sputter deposition of thin film nitinol and, 6) copper and silicon layers are removed

6.2.2 *In vitro* testing of the efficiency of micropatterned thin film nitinol samples to capture embolic particles

A bench-top flow loop was used for the *in vitro* testing of the efficiency of micropatterned thin film nitinol samples to capture embolic particles which is illustrated in Figure 51. It consists of silicone tubing (Platinum-Cured Silicone Tubing, Cole-Parmer, IL, USA) with inner diameter of 6.5mm which is close to the average human carotid artery dimensions[151]. To model the carotid

artery stenosis, microspheres (Cospheric, CA, USA) in diameter of 53-63μm in two different weight loads (*i.e.,* 10mg and 30mg) were homogenously dispersed in 500mg water-soluble poly (vinyl alcohol) (PVA) glue (Lineco®, MA, USA) and the homogenous suspension was uniformly deposited with the length of 14mm on the surface of the internal wall of the silicone tube. Micropatterned thin film nitinol was rolled and placed inside the commercially available nitinol vascular stent (Zilver Vascular Self Expanding Stent, Cook Medical, Bloomington, IN). The thin film nitinol covered stent was deployed in the silicone tube right on top of the suspension containing fluorescent microspheres. The silicone tube was connected to the pulsatile pump (Harvard apparatus, MA) and deionized water was circulating at 402 and 510mL/min and 65 and 85 beats per minute (bpm) in the tube for 30min[152]. The tube containing the device was placed in the water bath at temperature 37°C. Flowmeter (OMEGA®, FLR1000 series, CN, USA) and pressure meter (PressureMAT™, PendoTECH, NJ, USA) are placed adjacent to the carotid artery model to monitor the flow condition. At the ends of of flow circuit, a filter (Component Supply Co Inc., Fl, USA) with 105μm porosity dimension and 32% open area is placed which captures the released particles. The microspheres captured by the filter were imaged by fluorescent microscopy (Olympus BX43, Japan).

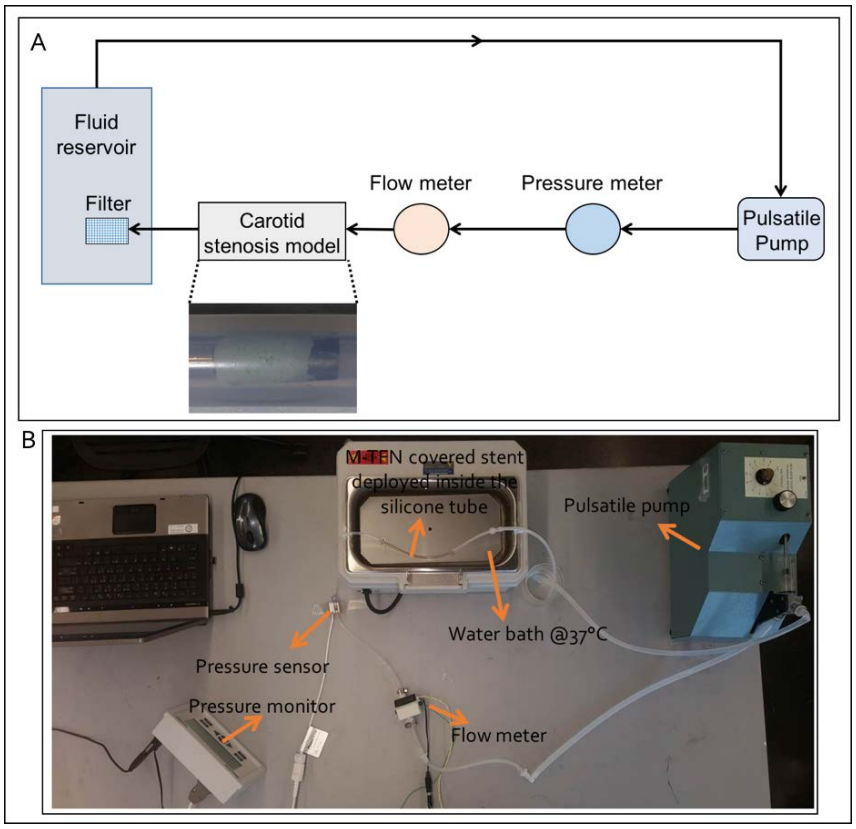

Figure 51: A) Schematic of flow loop in vitro set-up for carotid artery model, B) Flow loop in vitro set-up for carotid artery model

6.2.3 *In vitro* cell culture

Specimens of micropatterned thin film nitinol and solid thin film nitinol (*i.e.*, control sample) were prepared in 1cm×1cm dimensions. All the samples were sterilized by immersion in 70% ethanol for 30min, then, they were transferred to a 12-well tissue culture plates (Becton Dickinson and company, NJ, USA) and washed with sterile PBS (Gibco®, NY, USA). BAEC (Bovine Aortic Endothelial Cells; Lonza, NJ, USA) at passage number 5 were seeded at a

density of 2×10^5 cells/cm^2 on the samples. Cells were grown in the medium consisting of Endothelial Cell Basal Medium (EBM)-2 (Lonza, NJ, USA) and EGM-2 SingleQuot Kit Suppl. & Growth Factors including (Hydrocortisone 0.02%, FBS2%, VEGF0.05%, hFGF-B2%, IGF-1 0.05% and HEGF 0.05%, GA-1000 0.05%) (Lonza, NJ, USA). 2ml of media was added in each well of the tissue culture plate and the plates were kept in a humidified incubator under 5% CO_2 at 37°C.

6.2.3.1 Actin staining and fluorescent imaging

For the staining of F-actin, Alexa Fluor® 488 Phalloidin (ThermoFisher scientific, PA, USA) was used. After 48hrs cell culture, the samples were washed with PBS, fixed in 3.7% formaldehyde solution in PBS for 10min at room temperature and then each sample was extracted using acetone at –20°C for 3 to 5min. Subsequently, the samples were loaded with the fluorescent phalloidin washed with PBS and fluorescent images were taken using fluorescent microscopy (Olympus BX43, Japan).

6.2.3.2 Quantification of endothelial cell elongation and alignment

To quantitatively evaluate cell elongation and orientation, each phalloidin stained cell was visualized as an elliptical shape and the ratio of the major elliptic axis of individual the stained cells with respect to the horizontal axis was measured using MATLAB R2015a (MathWorks, MA, USA) image analysis. Moreover, the angle between the major axis of each individual cell with respect to the long axis of the micropattern was measured as the alignment angle using MATLAB R2015a (MathWorks, MA, USA) image analysis. Five samples of the micropatterned thin film nitinol and control samples were used and in each sample four spots were randomly picked and used for the analysis (*i.e.,* totally 20 images).

6.2.3.3 MTT endothelial cell viability and proliferation assay

Cell proliferation was assessed by a colorimetric assay using 3-(4, 5-dimethylthiazol-2-yl)-2, 5-diphenyl tetrazolium bromide (MTT, CT02 MTT Cell Growth Assay Kit, EMD Millipore, Darmstadt, Germany). Cells were cultured for 1hr, 4hrs, 24hrs and 5 days at an initial seeding density of 2×10^5 cells/ml on micropatterned thin film nitinol and the control sample with three replicates of each sample. After the determined incubation time, 0.01ml pre-warmed MTT solution was added to each culture well containing 0.1ml fresh cell medium and the cell culture plate containing MTT solution continued incubation for 4hrs under the same conditions. MTT solution has a pale yellow color which live cells cleave it to yield a dark blue formazan product. This transformation is catalyzed just by active cell mitochondria. Thus, the measurement of produced formazan can be an index of number of live cells. After 4hrs incubation of cells with MTT, 0.1ml isopropanol with 0.04 N HCl was added to each well. The HCl converts the phenol red in tissue culture medium to a yellow color that does not interfere with MTT formazan measurement. The isopropanol dissolves the formazan to give a homogeneous blue solution suitable for absorbance measurement. The absorbance was measured at a wavelength of 570nm using microplate reader (BioTek® Synergy 2, VT, USA).

6.2.3.4 Morphology and coverage percentage of endothelial cells

The morphology of endothelial cells adhered on substrates was probed by SEM after a thin layer of palladium (Pd) deposition by sputtering. For the SEM, cells were fixed with 2.5% glutaraldehyde (Sigma-Aldrich, MO, USA), dehydrated in a series of ethanol/DI water mixtures including 30%, 50%, 75%, 90% and 100% ratios, then, subjected to drying with hexamethyldisilazane (HMDS) (Alfa Aesar, MA, USA)/ethanol in 3:1, 1:1 and 1:3 volume ratios. The samples were dried in the hood overnight at room temperature. Coverage percentage

of endothelial cells on the micropatterned thin film nitinol and the control sample were analyzed using SEM images and MATLAB R2015a (MathWorks, MA, USA) image analysis. Five samples of the micropatterned thin film nitinol and control samples were used and in each sample four spots were randomly picked and used for the analysis (*i.e.*, totally 20 images).

6.2.4 Statistical analysis

Values regarding to embolic microspheres capture efficiency of micropatterned thin film nitinol, optical density regarding to the MTT assay, aspect ratio of attached endothelial cells and endothelial cell coverage percentage were expressed as the mean value ± standard deviation (SD). Statistical analysis was performed for the experiment using one-way analysis of variance (ANOVA) test and Tukey's HSD test by Minitab® 16.1.0 (©2010 Minitab Inc. PA, USA) and P-value<0.01 was considered statistically significant.

6.3 RESULTS

6.3.1 Morphology and porosity percentage of micropatterned TFN samples

Figure 52 shows the SEM images of micropatterned thin film nitinol samples. Multiple micropatterning morphologies (*e.g.*, ellipse, diamond or circle) and dimensions with a uniform distribution and smooth edge patterns and a wide range of porosity percentage (*i.e.*, 44%, 37%, 32%, 17% and 15%) have been obtained.

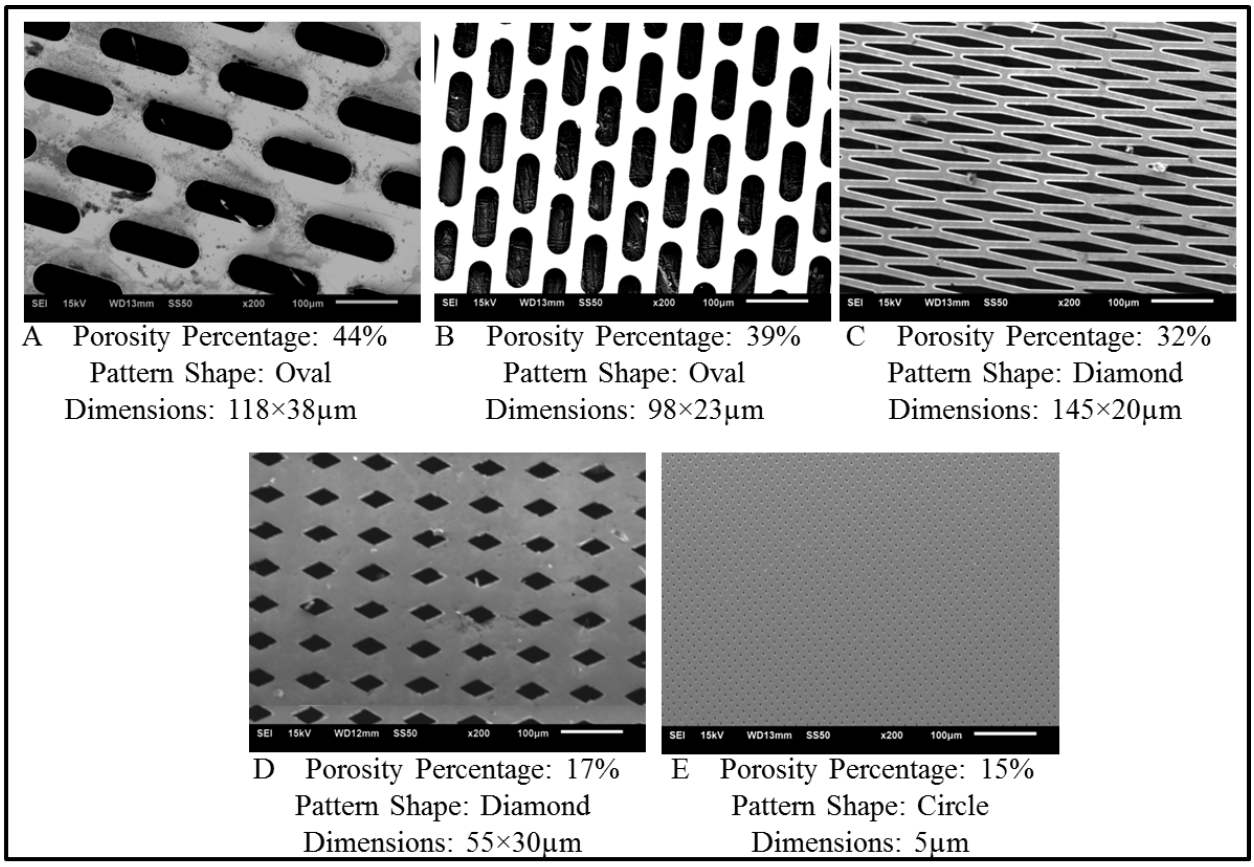

Figure 52: SEM images of micropatterned TFN samples with porosity percentage and dimensions of micropatterns (dimensions: major axis×minor axis)

6.3.2 The efficiency of micropatterned thin film nitinol samples to collect embolic particles

Figure 53 shows the capture efficiency (*i.e.*, ratio of the particle numbers kept by the thin film compared to the total particles) of micropatterned thin film nitinol samples. The lowest capture efficiency is 76.9±1.7 % which is observed in sample regarding to Figure 53A with 44% porosity

(*i.e.*, the highest porosity) while the highest capture efficiency is 96.1±0.81 % in the micropatterned film with 15% porosity (*i.e.*, the lowest porosity). It indicates that the porous TFNs effectively improve the embolism migration. By decreasing the flow rate and volume flow rate (VFR), the capture efficiency increases. In other words, in 65bpm flow rate, the level of embolism migration decreases in all the micropatterned stent grafts. By decreasing the particles mass, the capture efficiency slightly increases. It indicates that in lower accumulated deposition of plaques and fatty materials, the efficiency of these porous stent grafts increases. The capture efficiency of these micropatterned TFNs is pretty high for larger pieces of embolisms (*e.g.*, >180µm).

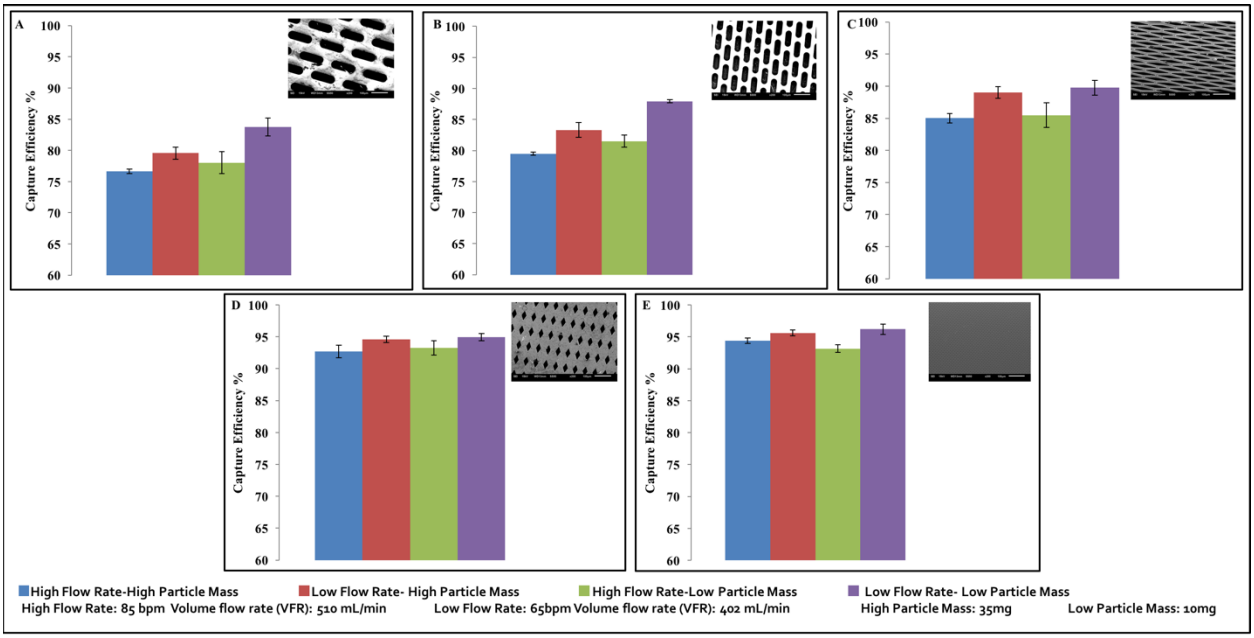

Figure 53: Capture efficiency percentage of micropatterned thin film nitinol samples

6.3.3 MTT cell viability and proliferation assay

Figure 54 shows the mean value of endothelial cells viability on thin film nitinol and micropatterned thin film nitinol samples that were evaluated using the MTT assay over five different time periods (1hr, 2hrs, 4hrs, 1day and 5 days). After 1hr, 2hrs, 4hrs and 1 day, no significant difference is observed between the TFN and micropatterned TFN samples but after 5 days, the optical density increases on the micropatterned TFN sample indicating the higher endothelial cell proliferation after micropatterning of the surface (P-value<0.01).

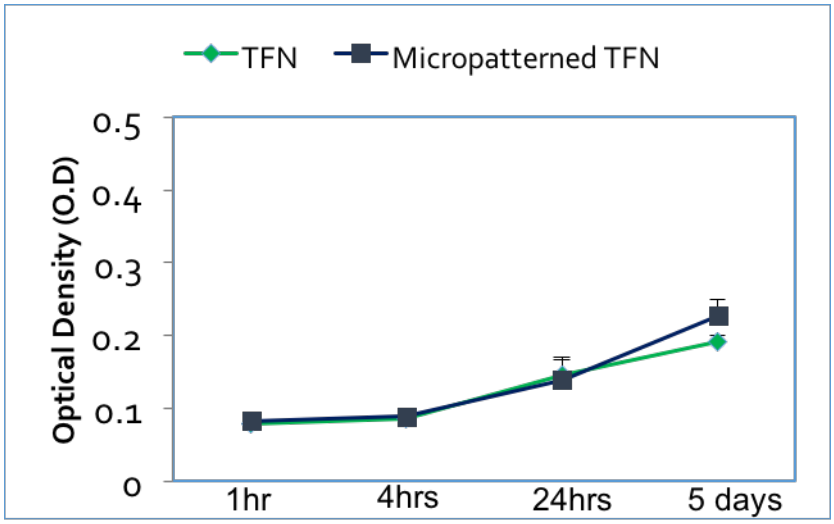

Figure 54: MTT assay for endothelial cell viability cultured on the TFN and micropatterned TFN substrates after 1hr, 2hrs, 4hrs, 24hrs and 5days

6.3.4 Quantification of endothelial cell elongation and alignment

Figure 55 shows the representative fluorescent images of stained endothelial cells cultured on thin film nitinol and micropatterned thin film nitinol.

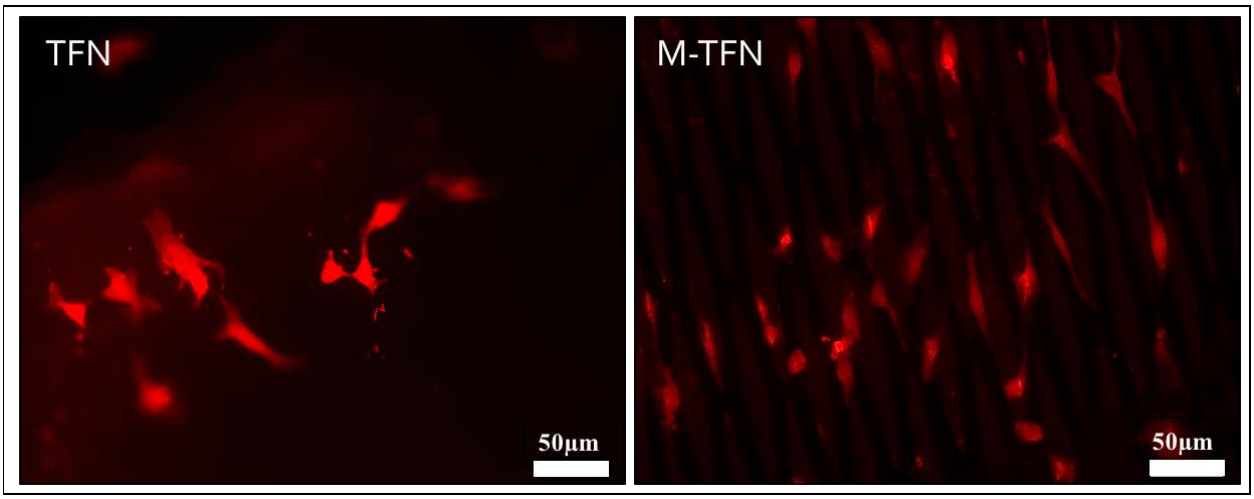

Figure 55: Representative fluorescent images of F-actin stained endothelial cell cultured on A) Thin film nitinol, B) Micropatterned thin film nitinol after 48hrs

The results of measuring the aspect ratio (*i.e.*, ratio of the minor axis to the major axis) of endothelial cells cultured on the micropatterned TFN and TFN are shown in Figure 56. The aspect ratio indicated the level of elongation of cells such that lower amount of it indicates that cells are more elongated. The value of aspect ratio demonstrated that the elongation of cells is two times higher on the micropatterned surface of thin film nitinol.

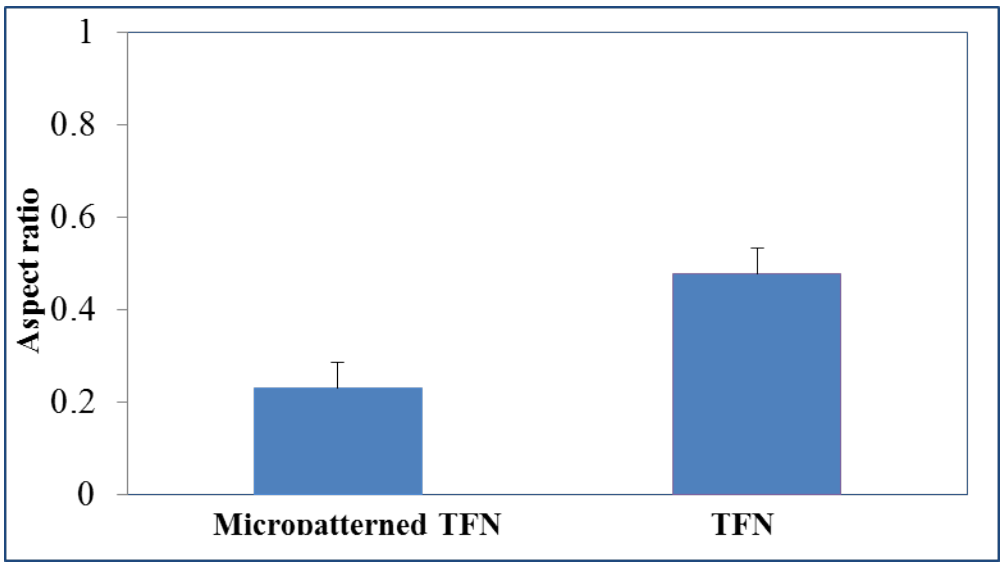

Figure 56: Aspect ratio of endothelial cells cultured on micropatterned TFN and TFN after 48hrs

Figure 57 shows the distribution of alignment angles of endothelial cells along the major axis of micropatterns of thin film nitinol. Quantitative analysis of actin alignment of endothelial cells on the micropatterns of TFN shows that around 35% of cells elongates along the major axis of the micropatterns with the angle of 40-50° and nearly 17% of cells elongate with 20-30° and 17% with 50-60° and the rest of cells elongate with alignment angles of 0-20°, 30-40° and 60-90° with approximately equal ratios. These results suggest that micropatterning impact the elongation and alignment of cells.

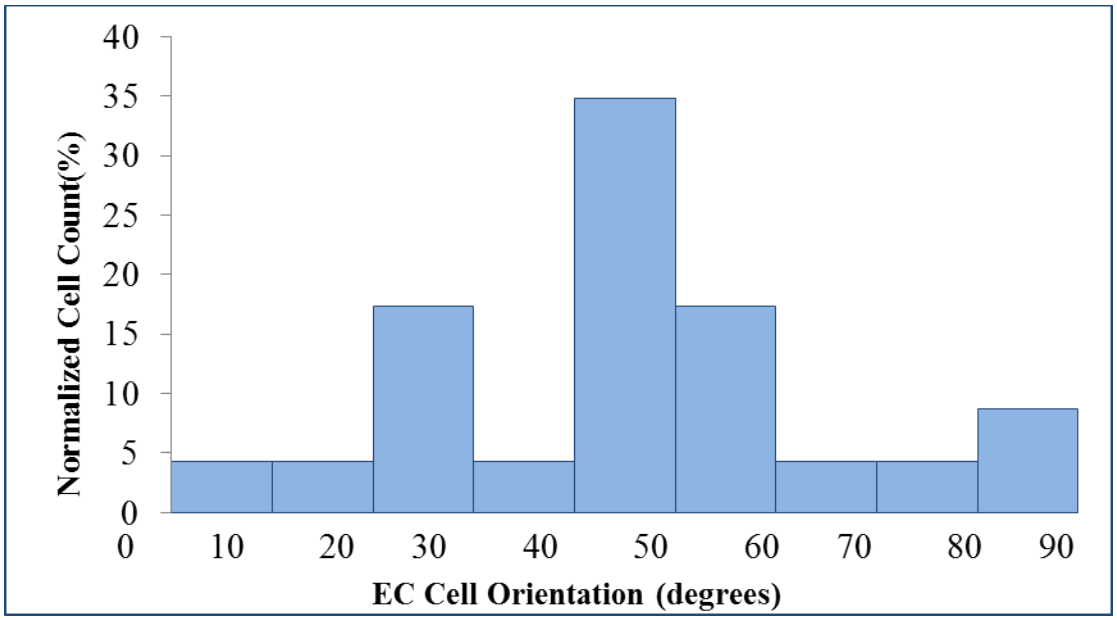

Figure 57: Alignment angles of endothelial cells along the major axis of micropatterns after 48hrs culture

6.3.5 Morphology and coverage percentage of endothelial cells

Figure 58 shows the representative SEM images of endothelial cells cultured on TFN and micropatterned TFN. Endothelial cells have spread out on the TFN substrate and major podia have emerged on the surface of cells (Figure 58A and C). Endothelial cells have spread out on the surface of micropatterned TFN and also grow on the porosities covering the total surface (Figure 58B, D and E). The endothelial cells integrate with each other on the micropatterned surface and show an integrated coverage on the surface.

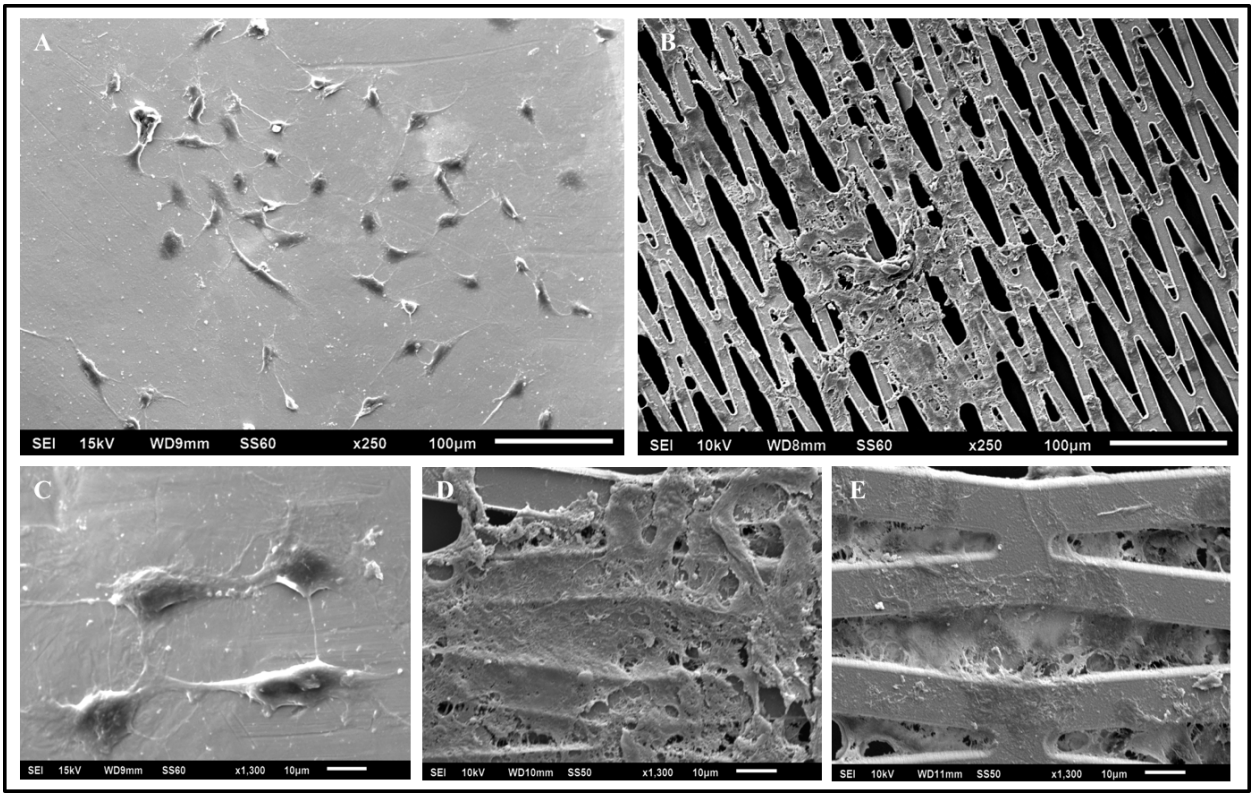

Figure 58: Representative SEM images of endothelial cells cultured on A) TFN and B) micropatterned TFN, C) TFN in high magnification, D) Front face of micropatterned TFN in high magnification and E) Back face of micropatterned TFN in high magnification

Quantitative analysis of SEM imaging shows that the coverage of endothelial cells are more than two times higher on the micropatterned TFN surface compared to the TFN surface (Figure 59). The coverage of endothelial cells on the front and back of micropatterned thin film nitinol is nearly the same level indicating the covering of the porosities and migration of endothelial cells.

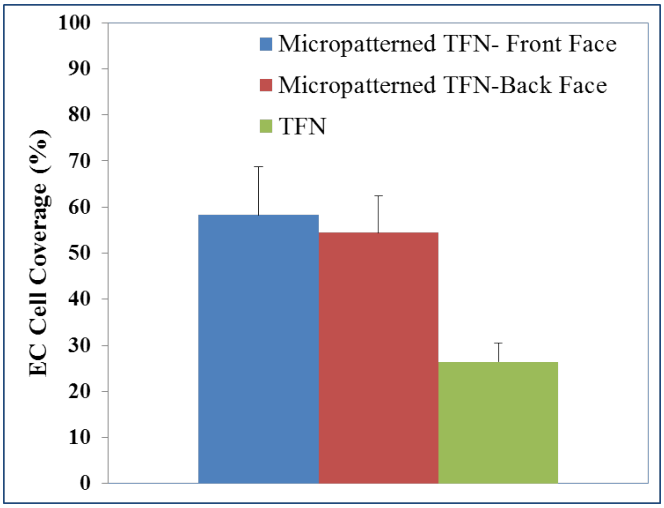

Figure 59: Percentage of endothelial cell coverage on front and back faces of micropatterned TFN and TFN

6.4 DISCUSSION

In the native tissues, cells are surrounded with a 3D microenvironment consisting of extracellular matrix and neighboring cells which impose geometrical and topographical constraints. These conditions influence ECM ligands binding with the cell surface receptors affecting intracellular signaling pathways and impacting the cytoskeleton architecture *e.g.*, actin network, cell polarity, migration, differentiation and growth. However, in the smooth surface of a biomaterial substrate (*e.g.*, TFN), cells encounter a homogenous substrate which does not have many important features of the native tissue microenvironment; therefore, the micropatterning of biomaterials surface is an efficient method to create a microenvironment for cells that is closer to the *in vivo* condition and control the cellular responses in the microscale level to guide cells constructing a

tissue with properties similar to the native tissue. The morphology and alignment of cells in 3D cellular organization in a tissue impact the function of tissue for instance the alignment of muscle cells in the heart tissue is the crucial requirement for generating strong contractile force of the heart.

Micropatterning of the surface allows manipulating the shape, porosity and dimension of microscale patterns and creating microenvironment to regulate multiple cellular responses. Several methods of patterning have been explored, including the creation of microgrooves and micropores[153, 154]. Micropatterning of medical stents has demonstrated the ability to regulate cell adhesion, proliferation, and differentiation along their surfaces by increasing the surface area of the stent exposed to the cells[155]. In order to reduce the risk of in-stent restenosis and thrombosis, it is crucial to prevent the proliferation and migration of smooth muscles cells while promoting rapid endothelialization[154]. Previous research has shown that micropatterning nitinol stents increases endothelialization along its surface[154].

In this study, the endothelial cell growth and elongation enhances upon micropatterning the surface of thin film of nitinol. Micropatterned TFN with 32% percentage porosity allows the blood perfusion to side microvessels and also demonstrates almost 90% efficacy to prevent the migration of embolic materials. During the deployment of stent, the superelastic thin film nitinol expands over the stent and the embolic materials place between the blood vessel wall and the thin film nitinol.

6.5 SUMMARY AND CONCLUSION

Stroke and carotid artery atherosclerotic disease represents a significant disease burden in the United States, showing the third most common cause of mortality. Recently, endovascular treatment became more popular due to its less invasive and more cost-effective nature compared with the open surgery. The endovascular approach uses balloon angioplasty and placement of stents with the separate embolic protection filter devices, where the filter is not so effective in reducing periprocedural complications. Therefore, we introduced a new device that does not require embolic protection filter devices, as well as it is low-profile, thromboresistant, and versatile to fabricate various fenestrations. The micropatterned thin film nitinol in multiple geometries (*i.e.*, diamond, oval and circle), various dimensions and porosities (*i.e.*, 15-47%) was produced by sputter deposition and a subsequent lift-off method, and then covered on the backbone. The efficacy of various micropatterned thin film nitinol to capture the embolic particles was evaluated in various atherosclerotic carotid artery stenosis conditions through *in vitro* tests. The results demonstrated that the micropatterned thin film nitinol covered stent can prevent the emboli dislodgement up to 70-96% during 30min duration tests, suggesting a high potential for the carotid artery occlusive disease treatment. Besides, results of *in vitro* cell culture show that endothelial cell adhesion, growth and elongation significantly enhance on the diamond-shape micropatterned thin film nitinol (*i.e.*, dimensions of 145μm×20μm and porosity percentage of 32%). Micropatterned thin film nitinol covered stent represents a high-potential low-profile device for treating carotid artery stenosis. *In vivo* studies must be carried on to demonstrate whether these preliminary results might translate into relevant clinical benefits as compared to the current available technologies.

7.0 CONCLUSION

Population aging, obesity and inactive lifestyle lead to increasing demands for artificial medical devices (*e.g.*, orthopedic and cardiovascular devices). In addition to increasing the demands, due to increasing the average life expectancy, the development of novel implantable devices with higher durability and functionality are urgently required. One of the keys to achieve this goal is to manage the interface between the implant and the host tissue via modifying the surface characteristics to increase the surface bio-functionality. Since 70–80% of implants are made of metallic biomaterials, developing surface modification techniques specific to metallic materials to enhance their biocompatibility is a pressing need in biomaterials field. In this study, four different novel surface treatment strategies are introduced for thin film nitinol and 316L stainless steel substrates for cardiovascular and orthopedic applications. For each strategy a target disease has been considered and the strategy and its efficacy in treating the disease has been explained:

1. Grain size refinement of 316L stainless steel obtained by two-dimensional linear plane-strain machining: 316L austenitic stainless steel samples with nanoscale grains were prepared under severe plastic deformation using linear plane-strain machining technique for three different rake angles (*i.e.*, 0°, 20° and 40°). The average grain size of 316L stainless steel is about 22µm while after plane-strain machining, it reduces to nanometer scale (*e.g.*, 42nm in 0° rake angle). Refining the grain size along with growing the oxide layer create surfaces with a

wide variety of surface topography, roughness and chemistry. The results of MC3T3 cell culture showed greatly improved cell adhesion and growth in nanoscale grain sample obtained by 0° rake angle. The oxide layer that is naturally formed on the surface demonstrated higher biocompatibility compared to both thermally and chemically formed oxides.

2. Rapid electrostatic seeding of endothelial cells for thin film nitinol based endovascular grafts: Surface oxide layer (*i.e.,* insulating layer) was grown on a 6μm thick thin film nitinol. Surface-treated thin film nitinol was used as the substrate for the electrostatic endothelial cell seeding. The induced electrostatic charge on the substrate was controlled through changing the applied voltages and it was calculated using Gauess' law assuming the cylindrical capacitor model. This novel technique enables the thin film nitinol graft to endothelialize rapidly within the intravascular catheter such that the condition of 5V voltage with induced electrostatic charge of 0.68×10^{-6}μC and induced electric field of $5.11 V/mm^{-1}$ demonstrated to enhance the endothelial cell attachment on the thin film nitinol deployed inside the catheter. This study demonstrated that a novel metallic scaffold, thin film nitinol, could rapidly increase the number of cells attached on the surface via electrostatic cell seeding.

3. Coating the thin film nitinol surface with electrospun silk: A thin layer of nanofiber silk was directly deposited onto the sputter-deposited thin film nitinol using electrospinning technique. While TFN is ultra-low profile (*i.e.,* a few micrometers thick), relatively thromboresistant, and superelastic, its surface endothelialization is not rapid and sufficient. The electrospun silk layer showed significantly decreased thrombus and improved endothelialization compared to two conventional vascular grafts (*i.e.,* Dacron® and e-PTFE). Therefore, integrated thin film nitinol/silk endograft represents a high-potential low-profile endovascular device, exploiting advantages from both thin film nitinol and thin electrospun silk layer.

4. Micropatterned thin film nitinol covered carotid artery embolic protection stent: Micropatterning process in multiple geometries (*i.e.*, diamond, oval and circle), various dimensions and porosities (*i.e.*, 15-47%) was performed on thin film nitinol substrate using sputter deposition and a subsequent lift-off method. The effectiveness of micropatterned TFNs covered stents in preventing the dislodgment and migration of plaque materials in atherosclerosis disease were tested using an *in vitro* set-up consisting of fluorescent microparticles as embolic particles. The results demonstrated that the micropatterned TFNs showed efficacy up to 70-96% in capturing the embolic particles during 30min duration tests. In addition, surface endothelialization drastically enhanced on the micropatterned TFN (*i.e.*, diamond shape patterns with 145µm×20µm dimensions). Micropatterned TFN covered stent represents a high potential novel candidate device for carotid artery embolic protection device

BIBLIOGRAPHY

[1] http://www.nemfi.com/orthopedic-implant-and-medical-device-finishing.html

[2] Domb AJ, Khan W. Focal controlled drug delivery: Springer; 2014.

[3] Novaes Jr AB, Souza SLSd, Barros RRMd, Pereira KKY, Iezzi G, Piattelli A. Influence of implant surfaces on osseointegration. Brazilian Dental Journal. 2010;21:471-81.

[4] Montes CC, Pereira FA, Thome G, Alves EDM, Acedo RV, de Souza JR, et al. Failing factors associated with osseointegrated dental implant loss. Implant dentistry. 2007;16:404-12.

[5] Stevens MM, George JH. Exploring and engineering the cell surface interface. Science. 2005;310:1135-8.

[6] Boyan BD, Hummert TW, Dean DD, Schwartz Z. Role of material surfaces in regulating bone and cartilage cell response. Biomaterials. 1996;17:137-46.

[7] Wilson CJ, Clegg RE, Leavesley DI, Pearcy MJ. Mediation of biomaterial-cell interactions by adsorbed proteins: a review. Tissue Eng. 2005;11:1-18.

[8] Williams R, Williams D. Albumin adsorption on metal surfaces. Biomaterials. 1988;9:206-12.

[9] Gronthos S, Simmons P, Graves S, Robey PG. Integrin-mediated interactions between human bone marrow stromal precursor cells and the extracellular matrix. Bone. 2001;28:174-81.

[10] MacDonald D, Rapuano B, Deo N, Stranick M, Somasundaran P, Boskey A. Thermal and chemical modification of titanium–aluminum–vanadium implant materials: effects on surface properties, glycoprotein adsorption, and MG63 cell attachment. Biomaterials. 2004;25:3135-46.

[11] Postiglione L, Di Domenico G, Ramaglia L, Montagnani S, Salzano S, Di Meglio F, et al. Behavior of SaOS-2 cells cultured on different titanium surfaces. J Dent Res. 2003;82:692-6.

[12] Meirelles L, Melin L, Peltola T, Kjellin P, Kangasniemi I, Currie F, et al. Effect of hydroxyapatite and titania nanostructures on early in vivo bone response. Clin Implant Dent Relat Res. 2008;10:245-54.

[13] Dalby MJ, Gadegaard N, Tare R, Andar A, Riehle MO, Herzyk P, et al. The control of human mesenchymal cell differentiation using nanoscale symmetry and disorder. Nature materials. 2007;6:997-1003.

[14] Siebers M, Ter Brugge P, Walboomers X, Jansen J. Integrins as linker proteins between osteoblasts and bone replacing materials. A critical review. Biomaterials. 2005;26:137-46.

[15] Chow T. Wetting of rough surfaces. Journal of Physics: Condensed Matter. 1998;10:L445.

[16] Bächle M, Kohal RJ. A systematic review of the influence of different titanium surfaces on proliferation, differentiation and protein synthesis of osteoblast-like MG63 cells. Clin Oral Implants Res. 2004;15:683-92.

[17] Kim S, English AE, Kihm KD. Surface elasticity and charge concentration-dependent endothelial cell attachment to copolymer polyelectrolyte hydrogel. Acta biomaterialia. 2009;5:144-51.

[18] Bet M, Goissis G, Vargas S, Selistre-de-Araujo H. Cell adhesion and cytotoxicity studies over polyanionic collagen surfaces with variable negative charge and wettability. Biomaterials. 2003;24:131-7.

[19] Schneider GB, English A, Abraham M, Zaharias R, Stanford C, Keller J. The effect of hydrogel charge density on cell attachment. Biomaterials. 2004;25:3023-8.

[20] Ducheyne P, Radin S, Heughebaert M, Heughebaert J. Calcium phosphate ceramic coatings on porous titanium: effect of structure and composition on electrophoretic deposition, vacuum sintering and in vitro dissolution. Biomaterials. 1990;11:244-54.

[21] Thull R, Grant D. Physical and chemical vapor deposition and plasma-assisted techniques for coating titanium. Titanium in medicine: Springer; 2001; 12:283-341.

[22] Jansen J, Wolke J, Swann S, Van Der Waerden J, De Groof K. Application of magnetron sputtering for producing ceramic coatings on implant materials. Clin Oral Implants Res. 1993;4:28-34.

[23] Fernandez-Pradas J, Cleries L, Serra P, Sardin G, Morenza J. Evolution of the deposition rate during pulsed laser deposition of hydroxyapatite coatings and its relation with target morphology. Applied Physics A. 2001;72:613-8.

[24] Herø H, Wie H, Jørgensen RB, Ruyter I. Hydroxyapatite coatings on Ti produced by hot isostatic pressing. J Biomed Mater Res. 1994;28:343-8.

[25] Sun L, Berndt CC, Gross KA, Kucuk A. Material fundamentals and clinical performance of plasma-sprayed hydroxyapatite coatings: a review. J Biomed Mater Res. 2001;58:570-92.

[26] Kim HM, Miyaji F, Kokubo T, Nakamura T. Preparation of bioactive Ti and its alloys via simple chemical surface treatment. J Biomed Mater Res. 1996;32:409-17.

[27] Ohtsuki C, Iida H, Hayakawa S, Osaka A. Bioactivity of titanium treated with hydrogen peroxide solutions containing metal chlorides. J Biomed Mater Res. 1997;35:39-47.

[28] Li P, De Groot K. Calcium phosphate formation within sol-gel prepared titania in vitro and in vivo. J Biomed Mater Res. 1993;27:1495-500.

[29] Webster TJ, Ejiofor JU. Increased osteoblast adhesion on nanophase metals: Ti, Ti6Al4V, and CoCrMo. Biomaterials. 2004;25:4731-9.

[30] Roy M, Bandyopadhyay A, Bose S. Induction plasma sprayed nano hydroxyapatite coatings on titanium for orthopaedic and dental implants. Surface and Coatings Technology. 2011;205:2785-92.

[31] de Oliveira PT, Nanci A. Nanotexturing of titanium-based surfaces upregulates expression of bone sialoprotein and osteopontin by cultured osteogenic cells. Biomaterials. 2004;25:403-13.

[32] Bagherifard S, Ghelichi R, Khademhosseini A, Guagliano M. Cell response to nanocrystallized metallic substrates obtained through severe plastic deformation. ACS applied materials & interfaces. 2014;6:7963-85.

[33] Kauffman GB, Mayo I. The story of nitinol: the serendipitous discovery of the memory metal and its applications. The chemical educator. 1997;2:1-21.

[34] Busch J, Johnson A, Lee C, Stevenson D. Shape-memory properties in Ni-Ti sputter-deposited film. Journal of applied physics. 1990;68:6224-8.

[35] Ho KK, Carman GP. Sputter deposition of NiTi thin film shape memory alloy using a heated target. Thin Solid Films. 2000;370:18-29.

[36] Chun Y, Levi DS, Mohanchandra K, Carman GP. Superhydrophilic surface treatment for thin film NiTi vascular applications. Materials Science and Engineering: C. 2009;29:2436-41.

[37] Kurtz S, Ong K, Lau E, Mowat F, Halpern M. Projections of primary and revision hip and knee arthroplasty in the United States from 2005 to 2030. The Journal of Bone & Joint Surgery. 2007;89:780-5.

[38] http://www.nursingceu.com/courses/492/index_nceu.html.

[39] MaTsushiTa T. Orthopaedic applications of metallic biomaterials. Metals for Biomedical Devices. 2010:329.

[40] Fosco M, Ayad R, Fantasia R. Orthopaedic implant materials and design. Wear of Orthopaedic Implants and Artificial Joints. 2012:133.

[41] Navarro M, Michiardi A, Castano O, Planell J. Biomaterials in orthopaedics. Journal of the Royal Society Interface. 2008;5:1137-58.

[42] Shayan M, Jung Y, Huang P-S, Moradi M, Plakseychuk AY, Lee J-K, et al. Improved osteoblast response to UV-irradiated PMMA/TiO2 nanocomposites with controllable wettability. Journal of Materials Science: Materials in Medicine. 2014:1-10.

[43] Anselme K. Osteoblast adhesion on biomaterials. Biomaterials. 2000;21:667-81.

[44] Valiev RZ, Estrin Y, Horita Z, Langdon TG, Zechetbauer MJ, Zhu YT. Producing bulk ultrafine-grained materials by severe plastic deformation. Jom. 2006;58:33-9.

[45] Langdon TG. Processing by severe plastic deformation: Historical developments and current impact. Materials Science Forum: Trans Tech Publ; 2010.;2:9-14.

[46] Estrin Y, Vinogradov A. Extreme grain refinement by severe plastic deformation: a wealth of challenging science. Acta materialia. 2013;61:782-817.

[47] Valiev R. Nanostructuring of metals by severe plastic deformation for advanced properties. Nature materials. 2004;3:511-6.

[48] Huot J, Balema V. Mechanochemical Effect of Severe Plastic Deformations: Metal Alloys, Hydrides and Molecular Solids. ChemInform. 2012;43:no.

[49] Saldaña L, Méndez-Vilas A, Jiang L, Multigner M, González-Carrasco JL, Pérez-Prado MT, et al. In vitro biocompatibility of an ultrafine grained zirconium. Biomaterials. 2007;28:4343-54.

[50] Xu X, Nie F, Wang Y, Zhang J, Zheng W, Li L, et al. Effective inhibition of the early copper ion burst release with ultra-fine grained copper and single crystal copper for intrauterine device application. Acta biomaterialia. 2012;8:886-96.

[51] Kim TN, Balakrishnan A, Lee B, Kim W, Smetana K, Park J, et al. In vitro biocompatibility of equal channel angular processed (ECAP) titanium. Biomedical Materials. 2007;2:117.

[52] Estrin Y, Kasper C, Diederichs S, Lapovok R. Accelerated growth of preosteoblastic cells on ultrafine grained titanium. Journal of Biomedical Materials Research Part A. 2009;90:1239-42.

[53] Estrin Y, Ivanova EP, Michalska A, Truong VK, Lapovok R, Boyd R. Accelerated stem cell attachment to ultrafine grained titanium. Acta biomaterialia. 2011;7:900-6.

[54] Zhao C, Cao P, Ji W, Han P, Zhang J, Zhang F, et al. Hierarchical titanium surface textures affect osteoblastic functions. Journal of Biomedical Materials Research Part A. 2011;99:666-75.

[55] Zheng C, Nie F, Zheng Y, Cheng Y, Wei S, Valiev R. Enhanced in vitro biocompatibility of ultrafine-grained biomedical NiTi alloy with microporous surface. Applied Surface Science. 2011;257:9086-93.

[56] Sunil BR, Kumar AA, Kumar TS, Chakkingal U. Role of biomineralization on the degradation of fine grained AZ31 magnesium alloy processed by groove pressing. Materials Science and Engineering: C. 2013;33:1607-15.

[57] Ye X, Liu T, Ye Y, Wang H, Tang G, Song G. Enhanced grain refinement and microhardness of Ti–Al–V alloy by electropulsing ultrasonic shock. Journal of Alloys and Compounds. 2014; 621:66–70

[58] Idell Y, Facco G, Kulovits A, Shankar M, Wiezorek J. Strengthening of austenitic stainless steel by formation of nanocrystalline γ-phase through severe plastic deformation during two- dimensional linear plane-strain machining. Scripta Materialia. 2013;68:667-70.

[59] Evans T, Hart A, James H, Smith V. New process for colouring stainless steel. Trans Inst Metal Finishing. 1972;50:77-9.

[60] Guillamet R, Lopitaux J, Hannoyer B, Lenglet M. Oxidation of stainless-steels(AISA-304 and AISI-316) at high-temperature influence on the metallic substratum. Journal de physique IV.1993;3:349-56.

[61] Shekhar S, Cai J, Basu S, Abolghasem S, Shankar MR. Effect of strain rate in severe plastic deformation on microstructure refinement and stored energies. Journal of Materials Research. 2011;26:395-406.

[62] Azushima A, Kopp R, Korhonen A, Yang D, Micari F, Lahoti G, et al. Severe plastic deformation (SPD) processes for metals. CIRP Annals-Manufacturing Technology. 2008;57:716- 35.

[63] Hayes J, Czekanska E, Richards R. The cell–surface interaction. Tissue Engineering III: Cell-Surface Interactions for Tissue Culture: Springer; 2012;2:1-31.

[64] Hryniewicz T, Rokosz K, Rokicki R. Electrochemical and XPS studies of AISI 316L stainless steel after electropolishing in a magnetic field. Corrosion Science. 2008;50:2676-81.

[65] Hanawa T, Hiromoto S, Yamamoto A, Kuroda D, Asami K. XPS Characterization of the Surface Oxide Film of 316L Stainless Steel Samples that were Located in Quasi-Biological Environments. Materials Transactions. 2002;43:3088-92.

[66] Park J-W, Kim Y-J, Jang J-H. Surface characteristics and in vitro biocompatibility of a manganese-containing titanium oxide surface. Applied Surface Science. 2011;258:977-85.

[67] Stoychev D, Stefanov P, Nicolova D, Valov I, Marinova T. Chemical composition and corrosion resistance of passive chromate films formed on stainless steels 316 L and 1.4301. Mater Chem Phys. 2002;73:252-8.

[68] Vázquez-Santoyo L, Pérez-Bueno J, Manzano-Ramírez A, Gonzalez-Hernández J, Pérez-Robles J, Vorobiev YV. Origin of interference colors on austenitic stainless steel. Inorganic materials. 2005;41:955-60.

[69] Shahryari A, Omanovic S, Szpunar JA. Enhancement of biocompatibility of 316LVM stainless steel by cyclic potentiodynamic passivation. Journal of Biomedical Materials Research Part A. 2009;89:1049-62.

[70] Hryniewicz T, Rokosz K, Filippi M. Biomaterial studies on AISI 316L stainless steel after magnetoelectropolishing. Materials. 2009;2:129-45.

[71] Sader MS, Balduino A, de Almeida Soares G, Borojevic R. Effect of three distinct treatments of titanium surface on osteoblast attachment, proliferation, and differentiation. Clin Oral Implants Res. 2005;16:667-75.

[72] http://www.nhlbi.nih.gov/resources/docs/2012_ChartBook_508.pdf

[73] http://en.wikipedia.org/wiki/List_of_causes_of_death_by_rate

[74] http://www.cdc.gov/heartdisease/facts.html

[75] http://www.cdc.gov/dhdsp/data_statistics/fact_sheets/docs/fs_heart_disease.pdf

[76] Behrouz R, Malek AR, Torbey MT. Small vessel cerebrovascular disease: the past, present, and future. Stroke research and treatment. 2012;2012.

[77] Fisher C. Lacunar strokes and infarcts A review. Neurology. 1982;32:871.

[78] Fisher C. Lacunar infarcts-a review. Cerebrovascular diseases. 1991;1:311 20.

[79] Criqui MH, Langer RD, Fronek A, Feigelson HS, Klauber MR, McCann TJ, et al. Mortality over a period of 10 years in patients with peripheral arterial disease. New England Journal of Medicine. 1992;326:381-6.

[80] Thom T, Haase N, Rosamond W, Howard VJ, Rumsfeld J, Manolio T, et al. Heart disease and stroke statistics—2006 update a report from the American Heart Association Statistics Committee and Stroke Statistics Subcommittee. Circulation. 2006;113:85-151.

[81] Lytle B, Loop F, Cosgrove D, Ratliff N, Easley K, Taylor P. Long-term (5 to 12 years) serial studies of internal mammary artery and saphenous vein coronary bypass grafts. The Journal of Thoracic and Cardiovascular Surgery. 1985;89:248.

[82] Cutler B, Thompson J, Kleinsasser L, Hempel G. Autologus saphenous vein femoropopliteal bypass: analysis of 298 cases. Surgery. 1976;79:325-31.

[83] Sabik JF. Understanding saphenous vein graft patency. Circulation. 2011;124:273-5.

[84] Veith FJ, Moss CM, Sprayregen S, Montefusco C. Preoperative saphenous venography in arterial reconstructive surgery of the lower extremity. Surgery. 1979;85:253-6.

[85] Teebken OE, Haverich A. Tissue engineering of small diameter vascular grafts. European journal of vascular and endovascular surgery. 2002;23:475-85.

[86] Bergan JJ, Veith FJ, Bernhard VM, Yao J, Flinn WR, Gupta SK, et al. Randomization of autogenous vein and polytetrafluoroethylene grafts in femoral-distal reconstruction. Surgery. 1982;92:921-30.

[87] Tilanus HW, Obertop H, Van Urk H. Saphenous vein or PTFE for femoropopliteal bypass. A prospective randomized trial. Annals of surgery. 1985;202:780.

[88] Strauss CE, Porten BR, Chavez IJ, Garberich RF, Chambers JW, Baran KW, et al. Real-time decision support to guide percutaneous coronary intervention bleeding avoidance strategies effectively changes practice patterns. Circulation: Cardiovascular Quality and Outcomes. 2014;7:960-7.

[89] Loscalzo J. Vascular Matrix and Vein Graft Failure Is the Message in the Medium? Circulation. 2000;101:221-3.

[90] https://www.studyblue.com/notes/note/n/robbins-vessels-test-2/deck/11910067

[91] Garg UC, Hassid A. Nitric oxide-generating vasodilators and 8-bromo-cyclic guanosine monophosphate inhibit mitogenesis and proliferation of cultured rat vascular smooth muscle cells. Journal of Clinical Investigation. 1989;83:1774.

[92] http://anatomyandphysiologyi.com/cardiovascular-system-blood-vessels/

[93] Stanley JC, Graham LM, Burkel WE. Endothelial cell seeded synthetic vascular grafts. Vascular Graft Update: Safety and Performance Philadelphia: ASTM. 1986:33-43.

[94] Belden T, Schmidt S, Falkow L, Sharp W. Endothelial cell seeding of small-diameter vascular grafts. ASAIO Journal. 1982;28:173-7.

[95] Stanley JC, Burkel WE, Ford JW, Vinter DW, Kahn RH, Whitehouse Jr WM, et al. Enhanced patency of small-diameter, externally supported Dacron iliofemoral grafts seeded with endothelial cells. Surgery. 1982;92:994-1005.

[96] Herring MB, Dilley R, Jersild Jr RA, Boxer L, Gardner A, Glover J. Seeding arterial prostheses with vascular endothelium. The nature of the lining. Annals of surgery. 1979;190:84.

[97] Seeger JM, Klingman N. Improved in vivo endothelialization of prosthetic grafts by surface modification with fibronectin. Journal of vascular surgery. 1988;8:476-82.

[98] Zheng W, Wang Z, Song L, Zhao Q, Zhang J, Li D, et al. Endothelialization and patency of RGD-functionalized vascular grafts in a rabbit carotid artery model. Biomaterials. 2012;33:2880- 91.

[99] Ogwu A, Okpalugo T, Ali N, Maguire P, McLaughlin J. Endothelial cell growth on silicon modified hydrogenated amorphous carbon thin films. Journal of Biomedical Materials Research Part B: Applied Biomaterials. 2008;85:105-13.

[100] Bowlin GL, Rittgers SE. Electrostatic endothelial cell seeding technique for small diameter (< 6 mm) vascular prostheses: feasibility testing. Cell transplantation. 1997;6:623-9.

[101] Bowlin GL, Rittgers SE, Milsted A, Schmidt SP. In vitro evaluation of electrostatic endothelial cell transplantation onto 4 mm interior diameter expanded polytetrafluoroethylene grafts. Journal of vascular surgery. 1998;27:504-11.

[102] Bowlin GL. Apparatus and method for endothelial cell seeding/transfection of intravascular stents. Google Patents; 2000.

[103] Mohanchandra KP, Chun Y, Prikhodko SV, Carman GP. TEM characterization of super-hydrophilic Ni–Ti thin film. Materials Letters. 2011;65:1184-7.

[104] http://www.mc.vanderbilt.edu/lens/images/uploaded/0816081804405art.jpg

[105] https://en.wikipedia.org/wiki/Cable_theory.

[106] Van Rijen H, Van Kempen M, Analbers L, Rook M, Van Ginneken A, Gros D, et al. Gap junctions in human umbilical cord endothelial cells contain multiple connexins. American Journal of Physiology-Cell Physiology. 1997;272:117-30.

[107] Boccaccini A, Keim S, Ma R, Li Y, Zhitomirsky I. Electrophoretic deposition of biomaterials. Journal of The Royal Society Interface. 2010;7:581-613.

[108] Besra L, Liu M. A review on fundamentals and applications of electrophoretic deposition (EPD). Progress in materials science. 2007;52:1-61.

[109] Zhao M, Bai H, Wang E, Forrester JV, McCaig CD. Electrical stimulation directly induces pre-angiogenic responses in vascular endothelial cells by signaling through VEGF receptors. Journal of cell science. 2004;117:397-405.

[110] Perler BA. Cost-efficacy issues in the treatment of peripheral vascular disease: primary amputation or revascularization for limb-threatening ischemia. Journal of Vascular and Interventional Radiology. 1995;6:111-5.

[111] Russell MAPE MW, Huse MA DM, Drowns MA S, Hamel AB EC, Hartz ScD SC. Direct medical costs of coronary artery disease in the United States. The American journal of cardiology. 1998;81:1110-5.

[112] Kakisis JD, Liapis CD, Breuer C, Sumpio BE. Artificial blood vessel: the Holy Grail of peripheral vascular surgery. Journal of vascular surgery. 2005;41:349-54.

[113] Amodeo A, Galletti L, Marianeschi S, Picardo S, Giannico S, Di Renzi P, et al. Extracardiac Fontan operation for complex cardiac anomalies: seven years' experience. The Journal of Thoracic and Cardiovascular Surgery. 1997;114:1020-31.

[114] Conte MS. The ideal small arterial substitute: a search for the Holy Grail? The FASEB journal. 1998;12:43-5.

[115] Turner D, Gaines P. Endovascular management of coarctation of the aorta. Seminars in interventional radiology:Thieme Medical Publishers. 2007; 24:153.

[116] http://mykentuckyheart.com/information/CoarctationoftheAorta.html

[117] Rao PS. Stents in the Management of Aortic Coarctation in Young Children. JACC: Cardiovascular Interventions. 2009;2:884-6.

[118] Rao P. Balloon angioplasty of aortic coarctation: a review. Clinical cardiology. 1989;12:618-28.

[119] Rodés-Cabau J, Miró J, Dancea A, Ibrahim R, Piette E, Lapierre C, et al. Comparison of surgical and transcatheter treatment for native coarctation of the aorta in patients≥ 1 year old. The Quebec Native Coarctation of the Aorta Study. Am Heart J. 2007;154:186-92.

[120] Egan M, Holzer RJ. Comparing balloon angioplasty, stenting and surgery in the treatment of aortic coarctation. 2009;7(11):1401-12.

[121] Toro-Salazar OH, Steinberger J, Thomas W, Rocchini AP, Carpenter B, Moller JH. Long- term follow-up of patients after coarctation of the aorta repair. The American journal of cardiology. 2002;89:541-7.

[122] Webb G. Treatment of coarctation and late complications in the adult. Semin Thorac Cardiovasc Surg: Elsevier; 2005;2:139-42.

[123] Stepan L, Levi D, Gans E, Mohanchandra K, Ujihara M, Carman G. Biocorrosion investigation of two shape memory nickel based alloys: Ni-Mn-Ga and thin film NiTi. Journal of Biomedical Materials Research Part A. 2007;82:768-76.

[124] Shayan M, Chun Y. An overview of thin film nitinol endovascular devices. Acta biomaterialia. 2015;21:20-34

[125] Altman GH, Diaz F, Jakuba C, Calabro T, Horan RL, Chen J, et al. Silk-based biomaterials. Biomaterials. 2003;24:401-16.

[126] http://www.intechopen.com/books/concepts-compounds-and-the-alternatives-of-antibacterials/chitosan-as-a-biomaterial-structure-properties-and-electrospun-nanofibers

[127] Zhang X, Reagan MR, Kaplan DL. Electrospun silk biomaterial scaffolds for regenerative medicine. Advanced drug delivery reviews. 2009;61:988-1006.

[128] http://biology.stackexchange.com/questions/36177/why-dont-our-cells-merge-when-their- phospholipid-membranes-touch-each-other

[129] Ho KK, Mohanchandra K, Carman GP. Examination of the sputtering profile of NiTi under target heating conditions. Thin Solid Films. 2002;413:1-7.

[130] Chun Y, Levi D, Mohanchandra K, Fishbein M, Carman G. Novel micro-patterning processes for thin film NiTi vascular devices. Smart Materials and Structures. 2010;19:105021.

[131] Chun Y, Levi DS, Mohanchandra K, Vinuela F, Carman GP. Thin film nitinol microstent for aneurysm occlusion. J Biomech Eng. 2009;131:051014.

[132] Motta A, Maniglio D, Migliaresi C, Kim H-J, Wan X, Hu X, et al. Silk fibroin processing and thrombogenic responses. Journal of Biomaterials Science, Polymer Edition. 2009;20:1875- 97.

[133] Burkel W. The challenge of small diameter vascular grafts. Med Prog Technol. 1987;14:165-75.

[134] Wang X, Lin P, Yao Q, Chen C. Development of small-diameter vascular grafts. World J Surg. 2007;31:682-9.

[135] Hashi CK, Derugin N, Janairo RRR, Lee R, Schultz D, Lotz J, et al. Antithrombogenic modification of small-diameter microfibrous vascular grafts. Arterioscler Thromb Vasc Biol. 2010;30:1621-7.

[136] Fuster V, Kim RJ. New Drugs and Technologies. Circulation. 2005;112:135-44.

[137] Chiu J-J, Chien S. Effects of disturbed flow on vascular endothelium: pathophysiological basis and clinical perspectives. Physiol Rev. 2011;91:327-87.

[138] Potters WV, Marquering HA, VanBavel E, Nederveen AJ. Measuring Wall Shear Stress Using Velocity-Encoded MRI. Current Cardiovascular Imaging Reports. 2014;7:1-12.

[139] Hoofnagle MH, Thomas JA, Wamhoff BR, Owens GK. Origin of Neointimal Smooth Muscle We've Come Full Circle. Arterioscler Thromb Vasc Biol. 2006;26:2579-81.

[140] Marx SO, Totary-Jain H, Marks AR. Vascular smooth muscle cell proliferation in restenosis. Circ Cardiovasc Interv. 2011;4:104-11.

[141] Kipshidze N, Dangas G, Tsapenko M, Moses J, Leon MB, Kutryk M, et al. Role of the endothelium in modulating neointimal formation: vasculoprotective approaches to attenuate restenosis after percutaneous coronary interventions. J Am Coll Cardiol. 2004;44:733-9.

[142] Lee Y-U, Luo J, Sprague E, Han H-C. Comparison of artery organ culture and co-culture models for studying endothelial cell migration and its effect on smooth muscle cell proliferation and migration. Ann Biomed Eng. 2010;38:801-12.

[143] Foulkes MA, Wolf PA, Price TR, Mohr J, Hier DB. The Stroke Data Bank: design, methods, and baseline characteristics. Stroke. 1988;19:547-54.

[144] http://www.strokecenter.org/patients/about-stroke/stroke-statistics/

[145] https://www.nhlbi.nih.gov/health/health-topics/topics/catd

[146] Rosamond W, Flegal K, Furie K, Go A, Greenlund K, Haase N, et al. American heart association statistics committee and stroke statistics subcommittee. Heart disease and stroke statistics—2008 update: a report from the American Heart Association Statistics Committee and Stroke Statistics Subcommittee Circulation. 2008;117:25-146.

[147] https://www.nhlbi.nih.gov/health/health-topics/topics/catd/treatment

[148] Stone GW, Webb J, Cox DA, Brodie BR, Qureshi M, Kalynych A, et al. Distal microcirculatory protection during percutaneous coronary intervention in acute ST-segment elevation myocardial infarction: a randomized controlled trial. Jama. 2005;293:1063-72.

[149] http://www.marmur.com/carotid-artery-stenting.html

[150] http://www.inspiremd.com/en/clinical-trials/carenet/

[151] Krejza J, Arkuszewski M, Kasner SE, Weigele J, Ustymowicz A, Hurst RW, et al. Carotid artery diameter in men and women and the relation to body and neck size. Stroke. 2006;37:1103- 5.

[152] Oktar S, Yücel C, Karaosmanoglu D, Akkan K, Ozdemir H, Tokgoz N, et al. Blood-flow volume quantification in internal carotid and vertebral arteries: comparison of 3 different ultrasound techniques with phase-contrast MR imaging. American journal of neuroradiology. 2006;27:363-9.

[153] Aubin H, Nichol JW, Hutson CB, Bae H, Sieminski AL, Cropek DM, et al. Directed 3D cell alignment and elongation in microengineered hydrogels. Biomaterials. 2010;31:6941-51.

[154] Shen Y, Wang G, Chen L, Li H, Yu P, Bai M, et al. Investigation of surface endothelialization on biomedical nitinol (NiTi) alloy: Effects of surface micropatterning combined with plasma nanocoatings. Acta biomaterialia. 2009;5:3593-604.

[155] Belkaid W, Thostrup P, Yam PT, Juzwik CA, Ruthazer ES, Dhaunchak AS, et al. Cellular response to micropatterned growth promoting and inhibitory substrates. BMC biotechnology. 2013;13:86.